Ph.D. Thesis in Physics

of

Daniela Bassignana

2012

New technologies of silicon position-sensitive detectors for future tracker systems

Universidad Autónoma de Barcelona
Facultad de Ciéncies, departamento de Física

Instituto de Microelectrónica de Barcelona
IMB-CNM (CSIC)

Thesis Directors: Dr. Giulio Pellegrini and Dr. Manuel Lozano Fantoba
Thesis Tutor: Prof. Enrique Fernández Sánchez

Ph.D. Thesis in Physics

of

Daniela Bassignana

2012

New technologies of silicon position-sensitive detectors for future tracker systems

Universidad Autónoma de Barcelona

Facultad de Ciéncies, departamento de Física

Instituto de Microelectrónica de Barcelona

IMB-CNM (CSIC)

Thesis Directors: Dr. Giulio Pellegrini and Dr. Manuel Lozano Fantoba

Thesis Tutor: Prof. Enrique Fernández Sánchez

Abstract

In view of the new generation of high luminosity colliders, HL-LHC and ILC, a farther investigation of silicon radiation detectors design and technology is demanded, in order to satisfy the stringent requirements of the experiments at such sophisticated machines. In this thesis, innovative technologies of silicon radiation detectors for future tracking system are proposed. Three different devices have been studied and designed with the help of different tools for computer simulations. They have been manufactured in the IMB-CNM clean room facilities in Barcelona and characterized with proper experimental setups in order to test both the detectors capabilities and the quality and suitability of the technologies used for their fabrication process.

The first technology deals with the upgrade of dedicated sensors for laser alignment systems in future tracker detectors. The design and technology of common single-sided silicon microstrip detectors have been slightly modified in order to improve IR light transmittance of the devices. The layout of the sensors has been decided following the hints of optical simulations and the fabrication process has been properly monitored, obtaining a final transmittance of 50% with a baseline pitch of 50μm. The second device is a novel 2D position sensitive detector based on the standard technology of single-sided AC coupled, silicon microstrip detectors in which resistive coupling electrodes made of polysilicon have been integrated. The resistive charge division method, applied reading out the resistive electrodes at both ends, was used to obtain spatial information on the coordinate of an ionizing event along the strip length. The prototypes fabricated, characterized with a laser set-up, showed a longitudinal spatial resolution of about 1.1% of the total strip length (20 mm) for a 6 MIPs signal. A Spice-like model of the detector has been developed and crosscheck with the experimental results, providing a good tool for future prototypes optimization.

Finally, the last proposal deals with the new design, fabrication and first characterization of double columns stripixel detectors. The device consists of double-columns electrodes (both n^+ and p^+ electrodes) arranged in a diamond configuration on one side of the n-type silicon bulk and connected by two separated metal layers organized in two sets of perpendicular strips that allow a X-Y projective readout of the sensor. The design has been optimized with the use of TCAD Sentaurus simulations and 2D position sensitivity has been demonstrated reconstructing a laser beam position within two consecutive p^+-type strips crossing two consecutive n^+-type strips, with a spatial resolution of 23μm.

The preliminary studies, the fabrication and characterization methods along with the experimental results are presented and discussed in the dedicated chapters of this thesis.

Publications

First author

2012 *Design, fabrication and characterization of the first full 3D stripixel detectors* D.Bassignana, Z.Li, M.Lozano, G.Pellegrini, D.Quirion, T.Tuuva, submitted to JINST.

2012 *Development of a novel 2D position-sensitive semiconductor detector concept* D.Bassignana, M.Fernandez, R.Jaramillo, M.Lozano, F.J.Munoz, G.Pellegrini, D.Quirion, I.Vila, 2012 JINST 7 C04008.

2012 *First investigation of a novel 2D position-sensitive semiconductor detector concept* D.Bassignana, M.Fernandez, R.Jaramillo, M.Lozano, F.J.Munoz, G.Pellegrini, D.Quirion, I.Vila, 2012 JINST 7 P02005.

2011 *Silicon microstrip detectors for future tracker alignment systems* D. Bassignana, G. Pellegrini, M. Lozano, M. Fernndez, I. Vila, A. Virto, R. Jaramillo, F.J. Munoz, Nucl. Instr. and Meth. A 628, 276-281.

Co-author

2012 *3D Double Sided Detector Fabrication at IMB-CNM* G. Pellegrini, J.P. Balbuena, D. Bassignana, E. Cabruja, C. Fleta, C. Guardiola, M. Lozano, D. Quirion, M. Ulln, Nucl. Instr. and Meth. available online at http://dx.doi.org/10.1016/j.nima.2012.05.087.

2011 *Silicon detectors for the sLHC* CERN RD50 Collaboration, Nucl. Instr. and Meth. A 658, 11-16.

2010 *New silicon microstrip detectors optimized for tracker alignment* M. Fernandez, I. Vila, M. Lozano, G. Pellegrini, D. Bassignana, Nucl. Instr. and Meth. A 624, 340-343.

Patents

2011 Semiconductor 2D postion-sensitive detector , aiming to technological transfert Pat. **PCT/ES2011/070088**. Inventors: D.Bassignana, M.Lozano, G.Pellegrini.

Conferences and workshops

Speaker or poster presenter

2011 *19th RD50 - Workshop on Radiation hard semiconductor devices for very high luminosity colliders*, CERN Geneve (Switzerland), 21-23 Nov 2011. **Talk**: *Characterization of the new stripixel detectors* .

2011 *IEEE Nuclear Science Symposium and Medical Imaging Conference*, Valencia (Spain), 23-29 October 2011. **Talk**: *Upgrade of a novel 2D position-sensitive semiconductor detector concept* and **Poster**: *New 3D stripixel detectors* .

2011 *XXXIII Bienal de Física*, Santander (Spain), 19-23 September 2011. **Talk**: *Upgrade of a novel 2D position-sensitive semiconductor detector concept* .

2011 *9th International Conference on Position Sensitive Detectors*, Aberystwyth (Wales), 12-13 September 2011. **Talk**: *Development of a novel 2D position-sensitive semiconductor detector concept* .

2010 *16th RD50 - Workshop on Radiation hard semiconductor devices for very high luminosity colliders*, Barcelona (Spain), 31 May-2 June 2010. **Talk**: *New 2D position sensitive detectors* .

2010 *12th Vienna conference on Istrumentation*, Vienna (Austria), 15-20 February 2010. **Poster**: *Silicon microstrip detectors for future tracker alignment systems* .

2009 *XXXII Bienal de Física.* UCLM Ciudad Real (Spain), 7th -11th September 2009. *Talk*: *IR Transparent Microstrip Detectors for a Laser Alignment System for future Silicon Trackers at ILC* .

Co-author

2011 *19th RD50 - Workshop on Radiation hard semiconductor devices for very high luminosity colliders*, CERN Geneve (Switzerland), 21-23 Nov 2011. **Talk**: *Progress with 2D microstrip detectors with polysilicon electrodes* , speaker: I. Vila.

2011 *International Workshop on Future Linear Colliders*, Granada (Spain), 26-30 September 2011. **Talk**: *A Novel 2D Position-Sensitive Semiconductor Detector Concept* , speaker: I. Vila.

2011 *XXXIII Bienal de Física*, Santander (Spain), 19-23 September 2011. **Talk**: *Infra-Red transparent microstrips detectors for tracker alignment* , speaker: F.J. Munoz.

2011 *Technology and Instrumentation in Particle Physics*, Chicago, (USA), 9-14 June 2011. **Talk**: *New semiconductor 2D position-sensitive detector* , speaker: F.J. Munoz.

2011 *18th RD50 - Workshop on Radiation hard semiconductor devices for very high luminosity colliders*, Liverpool (England), 23-25 May 2011. **Talk**: *Update of 3D Simulations and Processing of New BNL 3D-Trench-Electrode Detectors* , speaker: Z. Li.

2010 *17th RD50 - Workshop on Radiation hard semiconductor devices for very high luminosity colliders*, CERN Geneve (Switzerland), 17-19 November 2010. **Talk**: *A novel two-dimensional microstrip sensor with charge division readout* , speaker: I. Vila.

2009 *11th European Symposium on Semiconductor Detectors*, Wildbad Kreuth (Germany), 7-11 June 2009,. **Poster**: *New Silicon Microstrip detectors optimized for track alignment* , presenter: M. Fernandez.

Contents

1 Silicon detectors and tracking systems **1**

1.1 Working principle of semiconductor detectors 2

1.1.1 Basic physics of semiconductor substrates 2

1.1.2 The p-n junction properties 7

1.1.3 Basic diode detector 9

1.2 Position sensing 12

1.2.1 Microstrip detectors 13

1.2.2 Pixel detectors 16

1.2.3 3D detectors 17

1.2.4 Further design considerations 19

1.3 Signal processing 21

1.3.1 Basic front-end electronic 21

1.3.2 Noise analysis 23

1.3.3 Ballistic deficit 27

1.4 Applications in tracking systems 29

1.4.1 Future accelerators 32

2 IR Transparent detectors **37**

2.1 Laser alignment for tracking systems 39

2.1.1 AMS Tracker Alignment System 39

2.1.2 CMS Tracker Alignment System 39

2.2 Full simulation of the passage of light through a microstrip detector . . 40

2.2.1 Starting point: optical representation of a microstrip detector . 40

2.2.2 Preliminary optimization of the design 44

2.3 Layout of the detectors 46
2.4 Fabrication process and technology monitoring 48
2.4.1 Thermal grown silcon dioxide 50
2.4.2 Metallization with aluminium alloy 55
2.4.3 Passivation: an anti-reflection coating 61
2.4.4 Etch and deposition profile 67
2.4.5 Deposition of polycrystalline silicon 70
2.5 Electrical characterization 72
2.6 Optical characterization 75
2.7 Summary and discussion 80

3 New 2D position sensitive detectors 83
3.1 Principle of operation: resistive charge division in microstrip detectors . 85
3.2 Proof-of-concept prototypes 86
3.2.1 Specifications and fabrication 86
3.2.2 Modelling and simulation of the detector 88
3.3 Laser characterization 93
3.3.1 Experimental setup 93
3.3.2 Longitudinal scan results 94
3.3.3 Spatial resolution and noise considerations 97
3.4 A possible alternative configuration of the electrode 103
3.5 Summary and discussion 105

4 Stripixel detectors 109
4.1 Stripixel detector concept: state of the art 110
4.2 New prototype generation: a single side double strip detector 113
4.2.1 Optimization of the design: device simulation 113
4.2.2 Layout of the detectors 119
4.3 Fabrication process 121
4.3.1 Dual-column electrodes 122
4.3.2 Double metal deposition 125
4.3.3 Fabrication process monitoring 130
4.4 Electrical characterization 131

4.5 TCT measurements 134
4.5.1 TCT set-up and experimental technique 134
4.5.2 Measurements results 136
4.6 2D position sensitivity and spatial resolution 141
4.6.1 Laser characterization 141
4.7 Summary and discussion 144

5 Conclusions 147

Introduction

In view of the new generation of high luminosity colliders, HL-LHC [1] and ILC [2], a farther investigation of silicon radiation detectors capabilities, new designs and technologies are demanded in order to satisfy the stringent requirements of the experiments at such sophisticated machines. The upgrade of luminosity envisaged for the HL-LHC (from 10^{34} cm^2s^{-1} to 10^{35} cm^2s^{-1}) will impose a severe radiation environment characterized by fluences of heavy particles of the order of $10^{14}n_{eq}cm^{-2}$ at a distance of 20 cm from the interaction point and of $10^{15}n_{eq}cm^{-2}$ at about 4 cm from the impact point. This means that very high radiation hard detectors have to be developed in order to replace the current sensible elements in the inner tracking and vertex detector systems of the main experiment at LHC [3]: CMS [4] and ATLAS [5]. On the other hand, the International Linear Collider is a project concerning the precise measurements of the Higgs and/or new physics expected to be discovered at the LHC. The nature of the colliding beams (e^--e^+) and the goals established put many constraints to the tracking system and the vertex detector design of any possible experiment at the facility. The main challenges in this case are a high position resolution, especially in the vertex detector, and low mass of the tracking components to avoid multiple scattering preserving lepton ID and ensuring high performance of the calorimeters.

The investigation of new substrate material and technologies for high radiation hard semiconductor detectors is being mainly carried out by the members of the CERN RD50 collaboration [6], while the SiLC R&D collaboration [7] has the aim of developing new silicon radiation detectors that can satisfy the requirements of future tracker systems at the ILC.

At the IMB-CNM of Barcelona [8], thanks to the in-site clean room facilities, prototypes of silicon detectors can be fabricated for investigation purposes. Over the years, planar and 3D technologies have been developed matching the requirements of different experiments with the fabrication process techniques capability.

This thesis relates the development of three different silicon detector technologies for applications mainly in tracker detector systems.

The first deals with improving IR light transmittance of microstrip detectors for future alignment systems tuning and monitoring technological parameters during the detector fabrication. The second is the development of a new single-sided strip detector

that provides two coordinates of an ionizing event by means of the integration of double-read resistive electrodes and the use of the charge division method to obtain the spatial information. The third project is the new design of stripixel detectors, a 2D position-sensitive detector based on single-sided double columns 3D technology.

After a brief presentation of silicon properties and working principle of semiconductor detectors, in chapter 1, different technologies for position-sensitive detectors will be compared to each other: microstrip detectors, double-sided microstrip detectors, pixel detectors and 3D detectors. Then, an overview of the applications of silicon position-sensitive detectors in tracker systems will be reported with emphasis on the requests of future colliders.

Chapter 2 deals with the new silicon transparent detectors. The optical model developed by the IFCA group of experimental physics in Santander [9] to study transmittance of light in the sensors will be introduced. Then, the layout of prototype baby sensors will be described together with the main processes involved in their fabrication. The results of optical and electrical characterisations of the prototypes will be finally discussed.

In chapter 3 the novel 2D position-sensitive microstrip detector will be introduced. The resistive charge division method was implemented in the sensors by replacing the metallic electrodes with resistive electrodes made of polycrystalline silicon. Working principle and advantages will be described and a first study of the performance of baby sensors will be presented. An electrical model of two prototypes has been developed in order to simulate the effects of a short shaping time of the front-end electronics on the coordinate reconstruction. Then, after their fabrication, the samples have been characterized using a laser set-up to test the reconstruction of the longitudinal beam position using the resistive charge division method. The results obtained will be presented and discussed.

Chapter 4 is dedicated to the design and fabrication of the new stripixel detectors, the most complex detector fabrication process ever performed at the IMB-CNM clean room facility. The new device is a dual-column 3D detector in which the p^+ and n^+ columns are both processed on one side of the wafer and connected to a net of perpendicular strips defined on the surface (by means of two different metal layers) to allow a projective X-Y read out. Investigations of their detection capability and internal

structure have been carried out by Transient Current Technique measurements and a laser characterization: the results will be presented in this chapter.

Finally, chapter 5 will report the conclusions and the main important results obtained in the work presented in the previous chapters, discussing different aspects of their development, their applications and the future work and investigation that will be carried out.

Chapter 1

Silicon detectors and tracking systems

Nowadays silicon position-sensitive detectors find large application in the tracking system of high-energy physics experiments as well as in space experiments. The great advantage of semiconductors in radiation detection systems is that the average energy required to create a basic information carrier, i.e. an electron-hole pair, is some 10 times smaller than that required for gaseous detectors and 100 times smaller than that for scintillation detectors, that ensure high intensity of the detection signal. Then, because of their greater density, semiconductor detectors have a greater stopping power than gas detectors, so they are compact in size and can have relatively fast timing characteristics.

Among all, silicon is the most commonly used in semiconductor industry for different reason that spread from its large availability in nature, some physics characteristics as its band gap narrow enough to require low energy for ionization but large enough to allow operating at room temperature, and also thanks to technological advantages as the possibility of growing layer of silicon dioxide in thermal oxidation processes, which is a strong and stable dielectric.

In order to make easier appreciating the different features of the detectors presented in the next chapters, a brief description of the working principle of semiconductor detectors is presented in section 1.1 with emphasis on silicon substrate characteristics. It will be followed by an overview of the most relevant position sensitive devices (section 1.2) and by an introduction to the basic elements of the signal processing (section 1.3). Most of the information used to write this chapter are taken from textbooks by G.Lutz [10],

S.Sze [11], and H.Spieler [12]. The chapter will end with a brief overview of the applications of silicon position-sensitive detectors in tracking systems.

1.1 Working principle of semiconductor detectors

Regardless of their substrate and electrode structure, all semiconductor detectors are basically solid state ionization chambers. Briefly, when an ionizing particle (radiation) passes through the detector volume, it loses a quantity of energy that depends on the energy and on the type of the particle (radiation) itself as well as on intrinsic and geometrical characteristics of the substrate, like its density and its volume thickness. The deposited energy can then generate free electrons-holes pairs, whose number depends on the energy band gap width of the semiconductor. The free carriers movement, under the influence of the electric field appositely generated between the electrodes, finally induces an electrical signal that can be read and processed by an appropriate readout electronics, coupled with the electrodes contacts.

1.1.1 Basic physics of semiconductor substrates

Crystal structure

The substrate of a silicon particle detector is a wafer, a slice from a large single crystal, characterized by high resistivity and low impurities concentration. Crystals grown by Flow Zone technique with resistivity in the range of 1 - 10 kΩ are normally used for the purpose, although other silicon substrates are being investigated for high radiation-hard detectors [6].

Semiconductor materials are characterized by a crystalline structure in which the atoms are held together by covalent bonds forming a three dimensional periodic lattice. Silicon, with atomic number 14, has a diamond structure with each atom sharing its outermost electrons (valence electrons) with its four neighbours (figure 1.1 (a)). Within the crystal lattice it is possible to identify sets of equally spaced parallel planes that can be defined by the Miller indices. Miller indices use the direct basis vector system to define the crystal orientation by a tern of numbers. Let consider figure 1.1 (b), where three different planes in the silicon lattice are shown. On the left the plane

highlighted crosses the x-axis at α and the other two at infinite: the vector with the intersection coordinates is $(\alpha\ \infty\ \infty)$. The plane definition results from the reciprocal of the intersection coordinates $(1/\alpha\ 0\ 0)$ and a transformation that lead to the smallest set of integers with the same ratio, <100>. The other crystal directions have an analogues definition. Crystal orientation defines some mechanical and physical characteristics

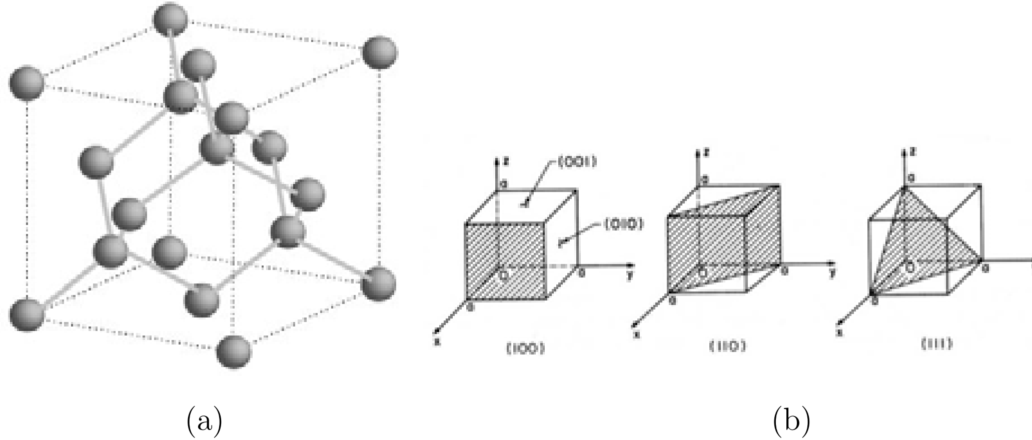

Figure 1.1: *(a) Diamond structure of the silicon crystalline lattice. (b) Three different orientation of the crystal defined by the Miller indices.*

of the substrate. For instance, <111> orientation provides a smaller probability of channelling, i.e. the passage of particle through the "free channels" of the crystal without interaction, while <100> orientation has smaller number of bonds per unit area, that reduces the density of interface traps (see sections 1.2.4 and 2.4.1) which is advantageous in MOS structures.

In an isolated atom (e.g in a gas) electrons can occupy discrete energetic levels. However, when atoms are bounded into a crystalline solid the wavefunctions of the valence electrons overlap and their levels are split into a large number of energy states very close to each other, generating almost continuous bands of energy, that may be separated by energy gaps. Thus, the solid's electrical behaviour depends on its bands structures. Insulators are characterized by an high energy gap between the valence and the conductive bands, which means that thermal energy can not excite electrons to the conductive band in normal conditions. In a conductor there is no band gap between the occupied and not occupied states and the electrons are able to move freely even at low temperature. In a semiconductor at T=0°C all the electrons occupy the lower-energy

valence band. Due to the narrow energy gap, with increasing temperature some of the electrons become thermally excited to the conduction band leaving unoccupied states (holes) in the valence band. Both the free electrons in the conductive band and the holes in the valence band can gain kinetic energy and momentum generating current flow. The energy necessary to create an electron-hole pair depends on the band gap width. The band structure of silicon is characterized by an energy gap of 1.12 eV. It is high enough to allow silicon detectors work at room temperature (differently from Germanium, which energy gap is 0.66 eV), but low enough to ensure high signals generation, i.e. high signal to noise ratio in proper conditions.

Intrinsic and doped silicon

The electrical properties of a semiconductor highly depend on the concentration of impurities into its crystal lattice. A semiconductor is referred to as intrinsic if the concentration of impurities is lower than the concentration of thermally generated free carriers, that can be obtained by integrating over all the states of the valence and conductive bands the density of states available with the probability of a state being occupied by an electron (Fermi-Dirac distribution). Being n and p the concentration of electrons and holes respectively, it gives:

$$n = N_c exp\Big(- \frac{E_c - E_F}{kT}\Big) \quad and \quad p = N_v exp\Big(- \frac{E_F - E_v}{kT}\Big) \tag{1.1}$$

where N_c and N_v are the density of the states in the conduction and valence band respectively, k is the Boltzmann constant, T the temperature and E_F the Fermi level, the energy state with 50% chance of being occupied by an electron. In intrinsic silicon the Fermi level is placed in the middle of the band gap (E_c-E_F = E_F-E_v) and carriers concentration is the same for electrons and holes, $n = p = n_i$, as they are produced in pairs by thermal excitation. $n_i \approx 10^{10}$ cm^{-3} at T=300 K, that can be compared with copper in which $n_i \approx 10^{23}$ cm^{-3} at the same temperature.

The presence of impurities in a semiconductor introduces new energy level inside the band gap altering its behaviour. Silicon and the elements of group IV of the periodic table have four valence electrons. Group V elements, such as Phosphorous, have 5 valence electrons and are referred to as donors. In the crystal, the extra electron is not bound and occupy a level just below the edge of the conductive band. Thermal exci-

tation will let it pass to the conductive band leaving a fixed positive ion in the crystal lattice. If the concentration of donors $N_d >> n_i$, then the electrons concentration will be $n=N_d$ and the material will be referred to as n-type doped. In this case the Fermi level shifts towards the conductive band, due to the higher probability of occupation of the states in the conductive band. Similarly, the group III elements, such as Boron, having only 3 valence electrons, leave an empty level just above the valence band edge, that will be occupy by an electron of the lattice (valence band). The result is a negative fixed ion in the lattice and an hole in the valence band. If $N_a >> n_i$, then the hole concentration will be $p=N_a$ and the material referred to as p-type doped. In this case the Fermi level shifts towards the valence band.

In general the carrier concentration is affected by both thermal generation and electron-hole recombination, but in thermal equilibrium the rate of generation and recombination will be equal and the carrier concentration will obey the action-mass lay:

$$np = n_i^2 \tag{1.2}$$

Carrier transport and resistivity

Free electrons and holes move randomly into the crystal under thermal motion. Two effects can cause a current flow of carriers: drift in an electric field and diffusion from regions of high to region of low carrier concentration.

When an ionizing event occurs into the detector substrate, the free carriers created must be collected by the electrodes in order to read and record the information. So, an electric field is established in the active volume by applying a potential between the electrodes. Under the influence of the electric field E, electrons and holes are accelerated along the field lines and scatter frequently losing part of their momentum in each collision. The resultant average drift velocity is given by:

$$v_n = -\mu_n E \qquad v_p = \mu_p E \tag{1.3}$$

where μ_n and μ_p are the mobility of electrons and holes respectively. In intrinsic silicon, as well as in doped silicon up to a concentration $\approx 10^{16}$cm^{-3}, their values are 1350 cm2/V·s and 480 cm2/V·s. The higher the electric field value, the higher the velocity of the carrier and the faster the response of the detector. Although, for high

values of the electric field the carrier velocity stop increasing assuming a saturation value, due to the high rate of scattering.

The contribution of diffusion to the net motion of carriers depends on the diffusion constant $D_{n,p} = \mu_{n,p}\frac{kT}{q}$ (with q the charge of the electron) and on the carrier concentration gradients n and p respectively. So, the overall current densities of electrons and holes can be written as:

$$J_n = q\mu_n nE + qD_n \quad n \qquad J_p = q\mu_p pE + qD_p \quad p \tag{1.4}$$

The relationship between the current flow and the generation and recombination of carriers is described by the carriers continuity equations. The rate of change in electrons and holes concentration in an infinitesimal volume is given by:

$$\frac{\delta n}{\delta t} = G - R + \frac{1}{q} \quad \cdot J_n \qquad \frac{\delta p}{\delta t} = G - R + \frac{1}{q} \quad \cdot J_p \tag{1.5}$$

where G is the carrier generation rate and R is the recombination rate.

In carrier transport phenomena, mobility is a key parameter, that represent the ability of an electron or hole to move inside a material under the influence of an electric field. It can be also used to express the resistivity of the material:

$$\rho = \frac{1}{q(\mu_n n + \mu_p p)} \tag{1.6}$$

that can be simplified to $\rho = \frac{1}{q\mu_n N_d}$ or $\rho = \frac{1}{q\mu_p N_a}$ in n-type or p-type doped semiconductors. At room temperature, resistivity of intrinsic silicon is $\approx$ 235 kΩ·cm, but it fall off to values of the order of the 1-10 kΩ·cm in doped p- or n-type silicon.

To establish a high field with a small quiescent current, the conductivity of the absorber must be low. As an estimate, applying 30V across a 300 μm thick absorber yields an average field of 10^3 V/cm, so the velocity of electrons is about $1.4{\cdot}10^6$ cm/s and it will take about 20 ns for an electron to traverse the detector thickness. Considering the detector has a surface of 1 cm^2 and a resistivity of 10 kΩ·cm. This means that its total resistance is 300 Ω, so the quiescent current flowing in it will be of order 1 mA. Since signal currents are typically of order μA, resistance has to be reduced. A solution is generating reverse-biased diode structures.

1.1.2 The p-n junction properties

The basic structure of a diode is a junction between n-type and p-type materials. For example it can be obtained diffusing sufficient p-type impurities into a homogeneous region of n-type material so as to change the diffusion region into a p-type semiconductor. In this way a junction is formed at the p-n interface.

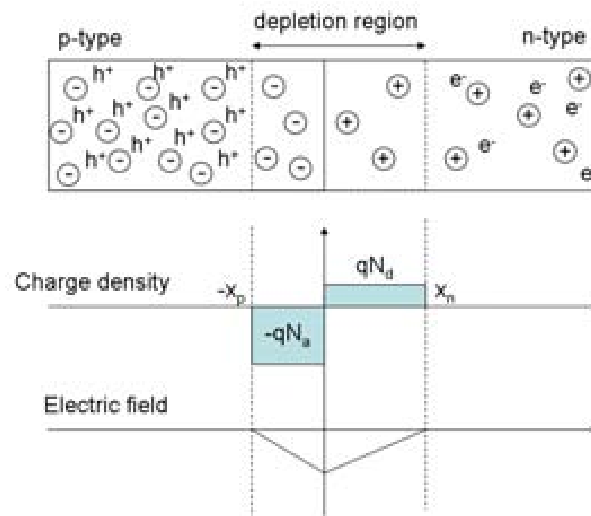

Figure 1.2: *Schematic of the p-n junction in equilibrium. Charge distribution and electric field inside the depleted region are shown.*

The difference in the holes and electrons concentration gradients at the interface causes diffusion of holes from the p-type to the n-type region and of electrons from the n-type to the p-type region. Due to this migration, a depleted zone is created around the junction, with much lower carrier concentrations than in the bulk and with uncompensated negatively-charged acceptors in the depleted p-type material and positively-charged donors in the n-type material (see figure 1.2). The depletion region extension is $W = x_p + x_n$, where $N_a x_p = N_d x_n$. At the same time, this space charge produces an electric field, inside the depletion region, which cause carrier to drift in the opposite direction of diffusion current, reaching a state of equilibrium where the net current is zero. the voltage difference between the edges of the depletion region is called the built-in potential which is normally of the order of 0.6 V to 0.8 V.

If we consider a p^+-n (n^+-p) junction, where the sign + indicates an high level of dopants, the depletion region will extend practically only in the n-type (p-type) re-

gion, W $\approx$ $x_{n,p}$ and all the space charges in the depletion region will have the same sign. Asymmetrical junction are normally created in semiconductor radiation detectors where an external positive voltage V_a is applied to the n-type region and a negative voltage to the p-type. In this configuration V_a has the same polarity (inverse polarization) of the built-in voltage, with the result of increasing the depletion region extension in the less doped region. Let consider a p^+-n junction, where the space charge has an effective density $N_{eff} = N_d$-N_a. Using the Poisson equation:

$$-\frac{d^2V(x)}{d^2x} = \frac{\rho(x)}{} \tag{1.7}$$

the electric field can be written as:

$$E(x) = \frac{qN_{eff}}{}(x - W) \tag{1.8}$$

with $E(x = W) = 0$. A second integration with $V(x = W) = 0$, gives:

$$V(x) = -\frac{qN_{eff}}{2}(x - W)^2 \tag{1.9}$$

So, the depletion width W is:

$$W(V_a) = \sqrt{\frac{2}{q\quad N_{eff}}(V_{bi} + V_a)} \tag{1.10}$$

where   is the product of the electric constant $_0$ and the relative permittivity of the semiconductor $_r$, which is 11.8 for silicon.

In a device with finite substrate thickness the full depletion width d is reach for a value of the applied voltage V_{dep}. Since it act as an insulator layer, to the depleted region is associated a capacitance per unit area that can be demonstrated to depend quite only on the depletion width:

$$C = \frac{}{W} = \begin{cases} \sqrt{\frac{e\ \varepsilon N_{eff}}{2V_a}} & \text{for} \quad V_a < V_{dep} \\ \frac{\varepsilon_{Si}\varepsilon_0}{d} & \text{for} \quad V_a \geq V_{dep} \end{cases} \tag{1.11}$$

V_{bi} has been omitted because it is normally one order or two lower than V_a.

In the inverse polarized p-n junction just a low leakage current flow through the depleted region. In an ideal diode it is due to diffusive motion of the few free carriers that remain in the space charge region. But in a real device diffusive current results

negligible compared to the current due to the generation of $e^- - h$ pairs by these impurities or defects that introduce new energetic levels inside the band gap.

The generation current density is given by:

$$J_g = qn_i \frac{W}{\tau_g} \tag{1.12}$$

where τ_g is the life time of the carriers generated due to the contribution of all the levels in band gap:

$$\tau_g = \left(\sum_i \frac{1}{\tau_i} \right)^{-1} \tag{1.13}$$

The value of J_g depends on the depletion width, i.e. on the voltage applied $J_g \quad W \quad \overline{V_a}$ and have a saturation value:

$$J_g = \frac{qn_i d}{\tau_g} \tag{1.14}$$

In the reality leakage current never saturate, because of superficial currents that introduce more charges in the diode although in a small quantity with respect to the charges generated by the defects. Finally, the current density value depends strongly on the temperature of the structure:

$$J_g \quad T^2 e^{\frac{\Delta E_i}{kT}} \tag{1.15}$$

where ΔE_i is the difference in energy between the levels where the pair $e^- - h$ is generated and the closest energy band: valence or conduction.

Now, considering the example at the end of the last section, generating a diode structure in the silicon substrate and applying the same reverse-bias of 30V, we will obtain a device with a leakage current 5 order of magnitude lower.

1.1.3 Basic diode detector

The simplest semiconductor radiation detector is a planar diode. Its structure is shown in figure 1.3. It is fabricated on a silicon n-type (can be p-type) wafer slightly ($\approx 10^{12}$ cm^{-3}) doped with phosphorous (can be boron) and hundreds of micron thick. On the front and on the back surfaces, narrow, highly doped, regions (electrodes) are created with thickness of the order of the micron and doping peak concentration of over 10^{18} cm^{-3}. A reverse bias is applied to the structure through metal contacts placed on the highly doped regions.

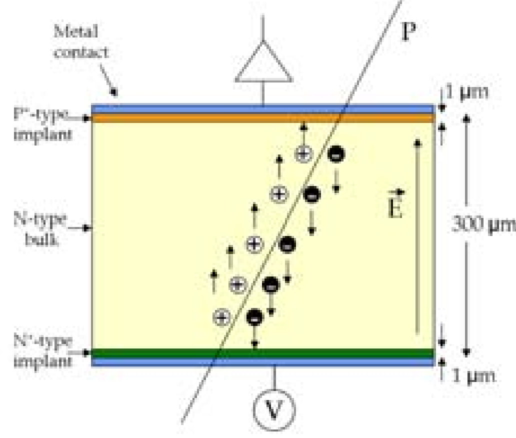

Figure 1.3: *Schematic of a p^+-in-n diode.*

The depletion voltage from equation 1.10, considering negligible the build-in voltage, is given by:

$$V_{dep} = \frac{q \quad N_{eff} \quad d^2}{2} \tag{1.16}$$

In this configuration the detector can be assimilated to a capacitor in which the depletion region is the dielectric and the high doped regions are the electrodes. The value of the associated capacitance is given by equation 1.11. In order to experimentally find the depletion voltage value, it is useful explicitly expressing the dependence of $1/C^2$ on V_{bias}:

$$1 \ C^2 = \frac{W^2}{2} = \begin{cases} \frac{2\varepsilon}{q\,N_{eff}} V_{bias} & \text{for} \quad V_a < V_{dep} \\ \frac{\varepsilon^2}{d^2} & \text{for} \quad V_{bias} \geq V_{dep} \end{cases} \tag{1.17}$$

$1/C^2$ shows two different trends: initially it grows linearly with V_{bias} up to the full depletion (V_{dep}), then it assumes a constant value independent of the voltage applied, that depends on the thickness of the depletion region. Fitting two lines to the curve in both the range of V_{bias}, (0-V_{dep}), (V_{dep}-) it is possibile to estimate the depletion voltage from the intercept between the lines.

When an ionizing radiation or particle crosses the depletion region (active volume) of the detector, electron-hole pairs are created proportionally to the energy deposited in the crystal. The free charges then drift through the device under the influence of the applied electric field. The signal is formed when the liberated charge carriers start moving, which changes the induced charge on the sensor electrodes proportionally to the distance travelled. The induced charge development with time can be calculated

using the Ramo s theorem [13], which demonstrates how it is due to the movement of the charges fields inside the substrate, rather than by their collection. Actually, although electrons are collected by the n-type electrode and holes by the p-type, the signal induced in both electrodes is the same with opposite charge and results from the superposition of the signals induced by both types of carriers. Then, as they move towards opposite directions, the signals they induce in each electrode have the same sign. The signal current begins when the carriers begin to move from the place in which have been generated and finishes when all the charges are collected. The collection time depends on the velocity of the carrier, i.e. on the electric field strength according to equation 1.3, t=x/μE. Due to the difference in the mobility of electrons and holes ($\mu_e \approx 3\mu_h$) electrons can be collected faster than holes. For instance, in a field of 2.5×10^3 V/cm the electron velocity is $3.3\cdot10^6$ cm/s, which means that in a device 300 μm thick electrons can be collected at least in 9 ns. In the same conditions holes will be collected in 27 ns. A faster response can be obtained by increasing the electric field strength or reducing the electrodes distance. Electric field can not be increased indiscriminately. At fields $>10^5$ V/cm, electrons acquire sufficient energy to form secondary electron-hole pairs, ultimately leading to a destructive avalanche, called breakdown . On the other hand, reducing the electrodes distance in planar detectors, will also reduce the active volume, causing a sensible decrease of the energy loss by the radiation (particle), and an increase of the total capacitance of the detector, that would affect the signal to noise ratio of the detector (see section 1.3.2).

Fixed the material and the geometry of the detector, the quantity and distribution of the electron-hole pairs generated by ionising radiation will depend on the type of radiation. In general, semiconductor detectors require a relatively low input of energy to create an electron-hole pair, for example, the mean energy in silicon is 3.6 eV, compared to 30 eV or so for gas detectors.

Photons will primarily interact with semiconductors by the photoelectric effect, where the photon is absorbed in a single interaction and an electron gains its energy. To generate an electron-hole pair, the photon energy must exceed the width of the bandgap. So, for example, since silicon has 1.12eV bandgap it is transparent to infrared light at wavelengths of beyond 1100nm (see chapter 2 and section 4.5). Photons of visible light will produce a single electron-hole pair. X-ray photons, however, have

energies of thousands of electron volts, and will produce large numbers of electron-hole pairs in a small spatial region where the photon was absorbed. The absorption of these photons is probabilistic, so if we have a beam of X-rays the flux reaching a depth x will be described by the Beer s law $I=I_0 e^{-\alpha x}$, where α is the absorption coefficient.

Unlike a photon, a charged particle will undergo a series of Coulomb interactions as it passes through silicon. These can be regarded as a series of collisions between the particle and the electrons in the silicon. When a charged particle passes through matter, its rate of energy loss with distance is given by the Bethe-Bloch formula [14], assuming that the particle is not deflected by the collisions:

$$\frac{dE}{dx} = 2\pi N_0 n_e^2 m_e c^2 \rho \frac{Z}{A} \frac{z^2}{\beta^2} \left[ln \left(\frac{2 m_e c^2 \gamma^2 \beta^2 W_{max}}{I^2} \right) - \beta^2 - \delta - 2\frac{C}{Z} \right] \tag{1.18}$$

where x is the path length in g/cm^2, N_0 is the Avogadro s number, r_e is the classic radius of the electron, m_e is the electron mass, ρ is the density of the medium, Z its atomic number, A its atomic weight, z is the charge of the incident particle in units of e, $\beta = v \; c$ of the incident particle, $\gamma = \frac{1}{1-\beta^2}$, W_{max} is the maximum energy transferred in a single collision, I is the mean excitation potential, δ is a density correction and C is a shell correction. At non-relativistic particle energies, the energy loss rate is inversely proportional to the energy, through β^2. Then the loss rate reach a minimum which is quite independent of the material traversed. Particles with this energy are referred to as Minimum Ionizing Particle (MIP) and are used as a reference in characterizing detection efficiency of detectors.

Since these interactions between charged particles and the semiconductor are statistical in nature, the total energy deposited by each particle will vary. However, in thin layers of solid material as in semiconductor detectors for tracking applications, the energy distribution produced over a large number of events is predictable, and follows a Landau distribution.

1.2 Position sensing

The development of semiconductor position-sensitive detectors was made possible by the adaptation of technologies used in Very Large Scale Integration (VLSI) microelectronics for the fabrication of silicon devices. In recent years, a very large variety

of detectors based on VLSI technology have been developed for many different applications in nuclear or particle physics tracking system as well as in space experiments. However, in this section just the three main types of detector structures based on semiconductor technology will be introduced, as a background of the detectors presented in the next chapters: microstrip detectors, pixel detectors and 3D detectors. Further design considerations will be add at the end of the section.

1.2.1 Microstrip detectors

Starting from the diode detector described above, a position sensitive microstrip detector can be obtained dividing the p^+ electrode into thin, parallel strips. Figure 1.4 is a representation of a silicon microstrip detector. Each strip forms a p^+n-diode. The gaps between strips must be electrically controlled to maintain isolation between adjacent diodes.

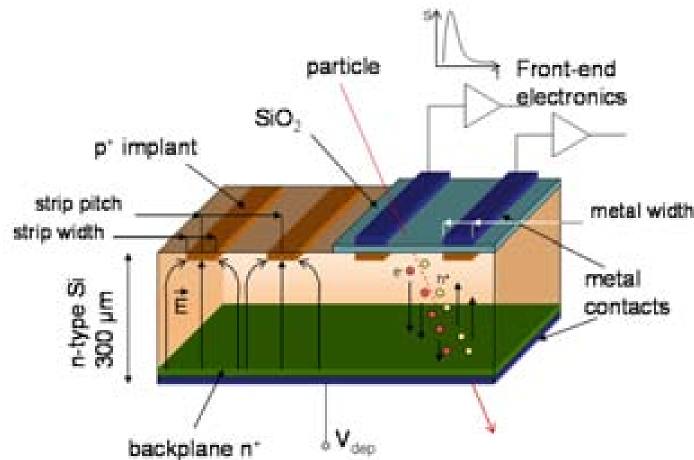

Figure 1.4: *Schematic of a microstrip detector AC coupled.*

A layer of thermally grown oxide provides this isolation. An aluminium layer deposited on the electrodes provides a low-resistance signal path to the readout electronics at the end of the detector. In order to decouple the strip diode biasing from the readout electronics, decoupling capacitors (thin SiO_2 layer) are normally integrated all over the strips while the bias voltage is applied through integrated polysilicon resistors connected to a bias ring, a p^+ implant that surround the detector area and is directly connected through a metal contact to the high voltage supply.

The electric field lines remain parallel in the detector until near the surface, where they bend along the surface and end on the electrode. The electrical segmentation is determined by the electrode pitch (p), rather than the width. In a colliding-beam experiment the strip pitch (centre-to-centre distance) is typically 25 - 100 μm and the maximum strip length (l) per sensor is limited by wafer size (10 - 15 cm for detector-grade Si).

Considering each strip separately, the bulk capacitance associated to each one can be expressed as :

$$C_d = \frac{pl}{d} \tag{1.19}$$

Then, consecutive implants are linked to each other by interstrip capacitances which value depends on the geometry of the strip (w p, with w the strip width) and which rule in the Signal to Noise ratio determination will be explained in section 1.3.2.

When a photon or a charged particle passes through the detector volume it induces current signal to the electrodes, as discussed above. Segmentation of the electrode in parallel strips makes the sensor sensitive to the position of the impinging radiation/particle along the direction transversal to the strip length. A simple valuation of the spatial resolution is given by the geometric resolution σ=p/ $\overline{12}$.

As explained in section 1.1.1, in addition to drift driven by the electric field, the charges are also subject to thermal diffusion, which spreads the charge cloud transversely with an rms width:

$$\sigma = \overline{2Dt} = \sqrt{\frac{2\mu kTt}{q}} = \sqrt{\frac{2kTx}{qE}} \tag{1.20}$$

which is the same for electrons and holes. So, in a device 300 μm thick, with an electric field of 2.5×10^3 V/cm, σ $\approx$6 μm. Although it might seems to degrade the obtainable position resolution, it can, in fact, improve it, increasing charge sharing between electrodes. Actually, even if only one p^+ electrode collects the charge, a signal is induced also to its neighbours: a larger cloud of charges will involve more strips in the induction process. Thus, when signals from each of the strips are read out separately, the hit search can be done using cluster-finding algorithms (CFA), tailored according to the geometry of the tracks [15] and a spatial resolution better than the geometric resolution can be achieved. The range of charge interpolation can be extended by introducing intermediate strips that are not connected to readout channels. The bias

resistors keep all strips at the same quiescent potential, but the time constant formed by the bias resistance and the strip capacitance is made so large that the potential of a floating strip can change individually in response to signal charge. The charge induced on the “floating” strips is then coupled capacitively to its neighbours.

Double-side microstrip detectors

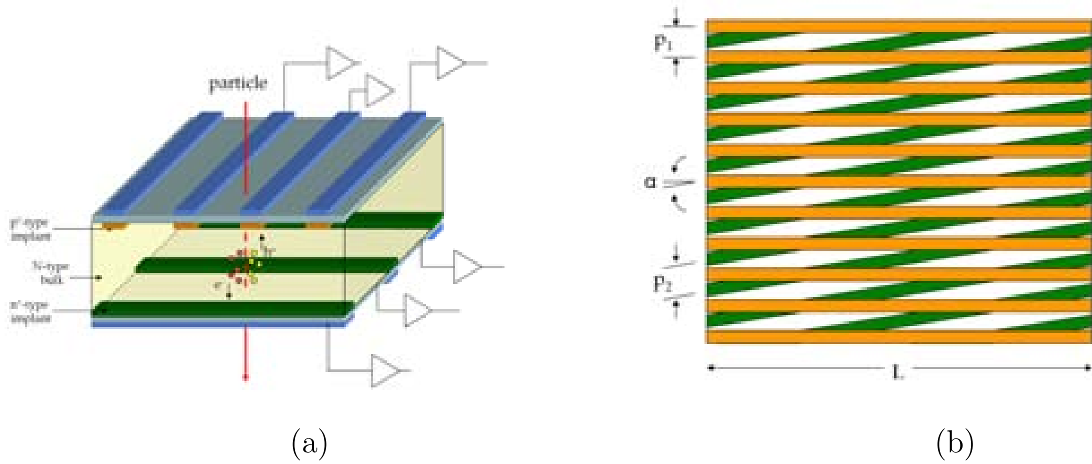

Figure 1.5: *(a) Schematic of a double-sided strip detector. (b) Electrodes arrangement where the strips subtend a small angle in order to partially resolve the multi-hit ambiguity problem.*

Two-dimensional position sensing can be obtained segmenting also the n-type electrode (double-sided process) in the direction perpendicular to the p-type strips (see figure 1.5 (a)). This configuration has some limitations at high hit densities. Each hit generates an x- and a y-coordinate. However, n tracks generate n x-coordinates and n y-coordinates, simulating n^2 hits of which n^2 - n are fake. The ambiguity can only be resolved with additional information to eliminate coordinates not consistent with tracks. A compromise solution, that is often adequate, utilizes “small-angle stereo”, where the strips subtend a small angle, rather than 90°. Small-angle stereo is illustrated in figure 1.5 (b). The area subtended by two sensing elements (strips) of length L1 and L2 arranged at an angle 90° is $A = L_1 L_2$, so a hit in a given strip can form combinations with hits on all of the transverse strips. The probability of “ghosting” is maximal. However, if the angle α subtended by the two strip arrays is small (and

their lengths L are approximately equal), the capture area is:

$$A \approx L^2 \frac{p_2}{p_1} \tan\alpha + L p_2 \tag{1.21}$$

The probability of multiple hits within the acceptance area, and hence the number of ghosts, is reduced as α is made smaller, but at the expense of resolution in the longitudinal coordinate.

1.2.2 Pixel detectors

Standard pixel detectors consist of two-dimensional diode arrays and electronics which are usually built on a separate substrate. The pixels are created by dividing the front surface into an array of electrodes with a common back contact. A very large number of connections are required to read out all the pixels. This is achieved by giving the readout chip the same pixel structure as the sensor, with each pixel containing the electronics required to process one readout channel. Each pixel on the sensor and the readout chip has a metal pad, and the two chips can be connected together face-to-face with metal bumps as shown in figure 1.6. This process is called bump bonding, and the finished assembly is referred to as a hybrid pixel detector. The size of the bump bonds and factors such as alignment accuracy will determine the minimum possible pixel size, i.e. the higher spatial resolution. Also in this case charges diffusion in the horizontal direction increase charge sharing between adjacent electrodes (pixels) so as to allow using hit finding algorithms in order to obtain a sub-pixel spatial resolution.

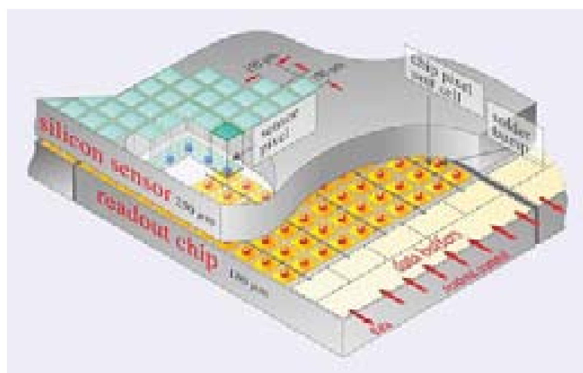

Figure 1.6: *Schematic of a pixel detector equipped with the readout electronics.*

1.2.3 3D detectors

A 3D detector is a variety of semiconductor diode detector where the p-i-n structure is formed by columns of p- and n-type material (normally polysilicon) passing vertical through the thickness of the substrate. The structure was proposed by S. Parker et al. in 1997 [16], and is illustrated in figure 1.7 with the typical geometry and dimensions. One set of electrodes are connected separately to readout electronics eventually in strips arrangement, like in a standard planar diode, and the other set are connected together and used to bias the device. When the device is depleted, electron-hole pairs generated by ionising radiation will be swept horizontally to the neighbouring electrodes.

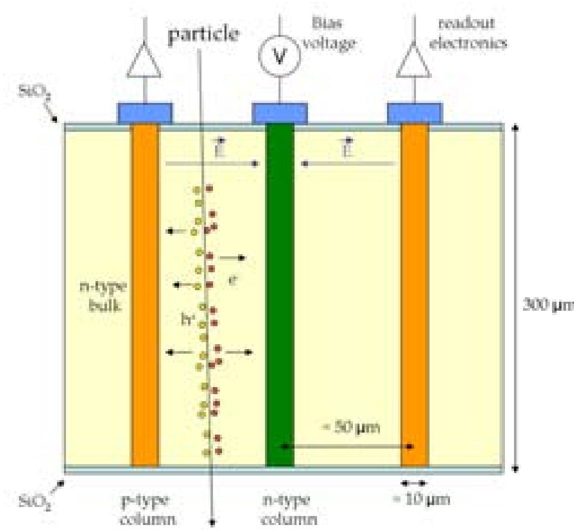

Figure 1.7: *Schematic cross section of a 3D detector.*

In the case shown in figure 1.7, the electrode columns pass through the full thickness of the substrate, and are connected out on the front surface. However, in the detectors normally produced by CNM the two sets of columns are fabricated from opposite sides of the substrate, and do not pass through the full substrate thickness [17]. Moreover, columns are not completely filled and the holes are passivated with silicon dioxide. More details on the 3D detector technology developed at the CNM will be discussed in chapter 4. The main advantage of the 3D structure is that, unlike in a planar detector, the spacing between p- and n-type electrodes is not determined by the substrate thickness. So, it becomes possible to achieve little electrode spacing, while still maintaining a sensitive thickness of a few hundred microns. Firstly, the reduced electrode spacing

dramatically reduces the depletion voltage. As shown by equation 1.16, the depletion voltage in a planar detector is proportional to the square of the electrode spacing. In a 3D detector, the situation is more complicated. The depletion region around each column will initially grow as a cylinder, finally reaching the other columns arranged in a squared grid. In a first cylindrical approximation the depletion voltage can be written as:

$$V_{dep} = \frac{qN_d}{2}\left(r_d^2\left[ln\left(\frac{r_d}{r_c}\right) - 0\ 5\right] + 0\ 5r_c^2\right) \tag{1.22}$$

where r_d is radius of the depleted region and r_c the radius of the column itself. So in this case too, the depletion voltage depends on the square of the electrode spacing: reducing this distance of a factor 10 would reduce the depletion voltage of the same factor, as an example one can compare the results shown in section 2.5 for planar strip detectors with substrate 300 μm thick and resistivity in the range 5-7 kΩ·cm, with the ones of section 4.4 where the characterization of 3D detectors with electrode spacing 56.6 μm and processed on wafer with the same characteristic is presented. In the first case the depletion voltage has a value of about 40 V, while in the second case it is less than 4 V. Similarly, the charge carriers collection time is determined by the collection distance, which is dramatically reduced by the 3D structure, and the field strength, which will be higher in a 3D detector (at a given bias). So, the 3D detector achieves fast charge collection, which is particularly important for radiation hardness of the device.

Lifetime of silicon detectors in a severe radiation environment like accelerators depends strongly upon their resistance to the radiation-induced damage. The main effect of this damage consist in increasing the number of extra levels in the band gap that can act as generation centres of e^--h^+ pairs or as traps for the free carriers, altering the electrical behaviour of the substrate and the detector performance. The generation centres are responsible of an increase in the leakage current and in the depletion voltage, while the traps will affect the charge collection of the carriers produced by ionizing event.

Thanks to the very short distance between electrodes, the depletion voltage of 3D detectors is substantially reduced with respect to planar detectors, and it should be possible to fully deplete them even after high radiation doses (expected at HL-LHC) as well as reducing the charge path to the electrodes, the number of trapped carriers

should be reduced, reducing charge collection degradation.

The 3D structure also reduces charge sharing between adjacent pixels [18]. Firstly, the fast collection time means that the carriers have less opportunity to diffuse outwards before being collected. Secondly, the 3D detector structure makes the carriers drift horizontally to the columns, keeping them away from the pixel boundaries. In contrast, in a planar detector the carriers drift vertically through the detector towards the electrodes, and are free to diffuse horizontally across the pixel boundaries. The reduced charge sharing is not an advantage in every application. As mention in the previous sections, charge sharing can be use to obtain a spatial resolution beyond the pitch or pixel size. Other disadvantages of 3D detectors are, the difficult and expansive fabrication process (see chapter 4.3), the inactive zone created by the electrode columns themselves [19] and the high capacitance of the device. The electric field will be negligible within the doped polysilicon (due to the high carrier concentration and high conductivity or to the empty/passivated volume inside them), and a signal will only be produced by the small number of carriers which diffuse out of the polysilicon into the depletion region. Than, following the approximation to cylindrical depleted region, the associated capacitance can be written as:

$$C = \frac{2\pi \ l}{ln(\frac{r_d}{r_c})} \tag{1.23}$$

that would be higher for smaller spacing of the electrodes like in the case of 3D detectors compared with planar detectors. We will see how this fact represents a disadvantage for what concern the electronic noise in section 1.3.2.

1.2.4 Further design considerations

In the previous sections, semiconductor detectors characteristics have been presented focusing the attention on the characteristic of the semiconductor substrate itself and on the different solutions one can achieve by choosing a proper geometry of the electrodes. In this section, some important details concerning the active volume boundaries will be discussed together with the designs and technologies developed to improve the detector performance.

Charge accumulation at the silicon-oxide interface

As explained below, SiO_2 is normally grown on the substrate surfaces to isolate adjacent electrodes or to create decoupling capacitors between the implant electrodes and the metal contacts. The resultant silicon-oxide interface is affected by dangling bonds due to the crystal structure mismatch (see section 2.4.1) that act as traps for the holes that slowly diffuse through the oxide towards the substrate, creating positive state charges. When electron-hole pairs are generated in silicon dioxide by ionising radiation, the electrons have a high chance of diffusing out of the oxide, whereas holes which have low mobility, can be trapped, creating positive state charges. This charge will attracts a layer of electrons to the silicon-oxide interface, which will affect the electrical behaviour in this region. In a detector with p-type readout electrodes, a higher field region will be created where each p-type implant meets the electron layer, ie at their boundaries. In a detector with n-type readout electrodes, the electron layer will short the n-type implants together, causing unwanted signal sharing. In order to avoid this effect, two common technologies have been developed [20] [21] , both concerning the use of additional p-type dopants to generate a p-spay layer or a p-stop implant. The p-spray is a uniform p^+ layer across the entire surface (with much lower concentration than the n^+ electrodes), while the p-stop consists in strips or rings (see chapter 4) of p^+ implant between the n^+ electrodes. Being the p-type implants close to the n-type electrodes high-field regions can be generated.

Edge effects and guard structures

A silicon wafer may contain many detector devices. So it must be diced to separate the chips, and this is typically done using a diamond saw. The saw-cut edges will contain many defects and dangling bonds. These defects make the edge more conductive than the bulk material, and will also allow increase electron-hole pairs generation. If the depletion region of the detector reaches the edge, then there can be a large current flow from the edge to the junction and from one side to another of the bulk if doped differently, affecting the sensor behaviour. To prevent this, there is typically an insensitive area around the chip, generally at least 100 μm wide, containing guard ring structures [22] that can stop currents from the edge and can define the edge of the active area of the detector. These structures are rings of doped implant of the same

type as the readout electrodes, in planar detectors, or rings of doped columns in 3D detectors (see chapter 4). Generally, at least one of the guard rings will be biased. Inactive areas are undesirable in detectors system like particle trackers, expecially in these regions where high granularity and sensitivity is demanded. e.g. vertex detectors. A mechanical solution is overlapping sensors modules where it is possible. As an instance, in visible light and x-ray detectors overlapping does not help, as photons are absorbed in the dead regions and lost for detection. A technological solution has been proposed [23] for all these applications that need reducing the dead area around the detectors. It concerns with using deep, reactive-ion etching in order to create deep trenches all around the detector area and then doping properly and passivating the edges obtaining active (electrodes) edges.

1.3 Signal processing

The readout electronic connected to the electrodes of a particle detector has many different functions concerning basic signal processing on the data. The raw detector signal is normally amplified and shaped through a filters system which tailors the overall frequency response to optimize signal-to-noise ratio, while limiting the duration of the signal pulse to accommodate the signal pulse rate. Pulse shaping determine both the total noise and the peak signal amplitude at the output of the shaper. In this section a brief analysis of the basic front-end electronics will be reported identifying the noise sources in the circuit and the effects of short peaking time constant.

1.3.1 Basic front-end electronic

In figure 1.8 a diagram of a diode detector connected to the bias circuit and to the basic front-end electronic is drawn. A capacitance C_d is associated to the sensor, which is a good representation of most detectors. A bias voltage is applied through a resistor R_b and the signal is coupled to the preamplifier through a capacitor C_{ac}. As seen in previous sections, normally, both R_b and C_{ac} are integrated in the microstrip detector itself. The series resistance R_s represents the sum of all resistances present in the input signal path, e.g. the electrode resistance and parasitic resistances in the input transistor.

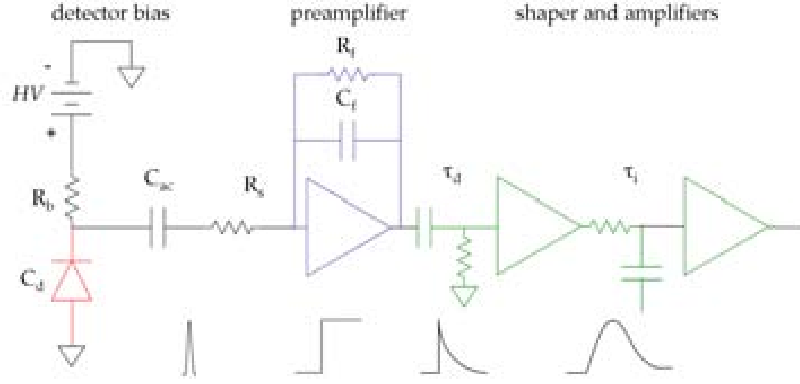

Figure 1.8: *Schematic of the basic front-end electronics connected to a semiconductor detector.*

As shown above, the passage of an ionizing particle through the detector volume cause induced charges at the detector electrodes. This signal charge can be quite small, about 4 fC (4×10^{-15} C) in a typical high-energy tracking detector, so it must be amplified. For this purpose, a charge sensitive preamplifier is normally used, in which almost all the current from the detector, $i_i(t)$, flows into the feedback capacitor C_f charging it up. The output voltage is given (ideal preamplifier, i.e. infinite gain) by $V_{out} = Q_i/C_f$, where Q_i is the total charge. Then, the capacitor will discharge through an high resistor, represented by R_f. After the preamplifier, additional amplifiers can also be used to increase the amplification.

The step-function signal at the output of the preamplifier is then processed by the shaper. In figure 1.8, a first order CR-RC shaper is depicted. Although pulse shapers normally have a more complicated structure, the CR-RC shaper contains the essential features of all pulse shapers, reducing the frequencies spectrum of the signal to a limited band. A high-pass filter (differentiator) sets the duration of the pulse by introducing a decay time constant τ_d. Next a low-pass filter (integrator) increase the rise time to limit the noise bandwidth. The overall frequency response is the product of the individual frequency responses $G(f) = G_{int}(f) \cdot G_{diff}(f)$. Since in the Fourier transform a product in the frequency domain is expressed in the time domain as the convolution, the output pulse shape of the CR-RC shaper is the convolution of the input signal with the time responses of the individual stages:

$$V_{out}(t) = V_i(t) * g_{int}(t) * g_{diff}(t) = \frac{Q_i}{C_f}\frac{\tau_d}{\tau_d - \tau_i}\left[e^{-t/\tau_d} - e^{-t/\tau_i}\right] \tag{1.24}$$

where τ_d and τ_i are the time constants of the differentiator and the integrator respectively. When τ_d=τ_i=τ

$$V_{out}(t) = \frac{Q_i}{C_f}\frac{t}{\tau}e^{-t/\tau} \tag{1.25}$$

is a good representation. The output pulse assumes its maximum at the peaking time $T_P = \tau$. The noise performance of this simple shaper is only 36% worse than the optimum filter. Thanks to its simplicity, the CR-RC shaper can be used for simple estimation of the shaper performance.

1.3.2 Noise analysis

Reading out the signal produced by radiation/particle detectors, will always lead to handle with electronic noise. It has many different sources, depending on the devices involved in the readout electronic chain. In general, the amplitude distribution of the noise is Gaussian, so noise fluctuations superimposed on the signal also yield a Gaussian distribution. Thus, by measuring the width of the amplitude spectrum of a well-defined signal, one can determine the noise level.

Electronic noise places a lower bound on the detectable signal level and also determines the ability to distinguish signal levels or measure them precisely. In semiconductor position sensitive detectors, spatial resolution also depends on the Signal-to-Noise ratio (S/N), thus improving this value, i.e. reducing the noise signal, is an important goal that has to be taken into account since in the detector and the front-end electronic design. Noise is due to many different effects.

Thermal noise, unavoidable at non-zero temperature, is due to the thermal agitation of carriers in conductors and cause fluctuation of the carrier velocity, it is associated to the resistors and its spectral density versus frequency is:

$$\frac{dP_n}{df} = 4kT \tag{1.26}$$

where k is the Boltzmann constant and T the absolute temperature.

On the other hand, shot noise generates time-dependent fluctuations in the current signal and is caused by the discreteness of the electron charge. It is typical of solid-state devices based on p-n junctions. The spectral density of the current fluctuations can be expressed as:

$$\frac{di_n^2}{df} = i_n^2 = 2eI \tag{1.27}$$

where I is the average current and e the electronic charge.

The noise spectrum becomes nonuniform whenever the fluctuations are not purely random in time, for example when carriers are trapped and then released with a time constant τ. With an infinite number of uniformly distributed time constants the spectral power density assumes a pure 1/f distribution. A finite number of time constants will reduce the 1/f distribution to a limited frequency range. The voltage spectral distribution is given by:

$$\frac{de_n^2}{df} = e_n^2 = \frac{A_f}{f} \tag{1.28}$$

where A_f depends on the device.

Considering the front-end electronic described above it is possible to study the main noise sources that affect the signal readout from a generic solid state detector.

Figure 1.9 represents the equivalent circuit of the detector front-end presented in figure 1.8. The main noise sources inside and outside the detector are represented by current (parallel component) or voltage e_n (series component) sources along the circuit, with current or voltage spectral density $i_n = di_n^2 \ df$ and $e_n = de_n^2 \ df$ respectively. Note that all the sources considered are placed before the preamplifier and shaper stage: actually, the noise signal act as any other electric signal, being amplified by the correspondent circuital elements, so any other noise source after the preamplifier input is negligible.

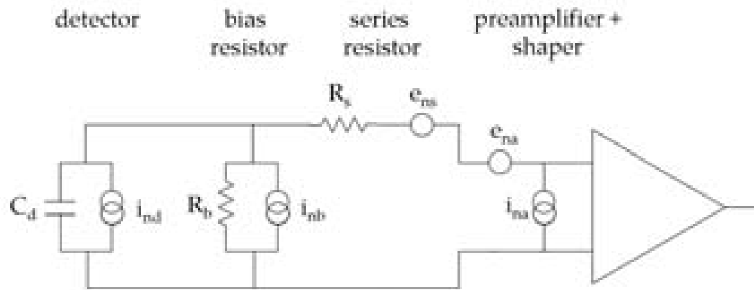

Figure 1.9: *Equivalent circuit for noise analysis of the detector connected to its front-end electronics.*

The noise sources due to the detector concern with the leakage current (I_d), the bias resistor (R_b) and any resistive component in series (R_s) to the preamplifier input, e.g. the electrode resistance. The leakage current and the bias resistor components can be modelled as current sources in parallel to the detector or the resistance respectively,

with spectral density:

$$i_{nd}^2 = 2eI_d \qquad i_{nb}^2 = \frac{4kT}{R_b} \tag{1.29}$$

In order to simplify the analysis, current sources can be converted into voltage sources in series to the input obtaining respectively:

$$e_{nd}^2 = \frac{2eI_d}{(wC_d)^2} \qquad e_{nb}\ {}^2 = \frac{4kTR_b}{1+(wR_bC_b)^2} \tag{1.30}$$

The series resistance component can include effects due to parasitic resistance at the preamplifier input and can be represented by a voltage source with spectral density:

$$e_{ns}^2 = 4kTR_s \tag{1.31}$$

The noise due to the front-end electronics is mainly associated to the input transistor of the preamplifier and can be represented by a current generator in parallel to the input with current spectral density $i_{na}^2 = 2eI_a$ and voltage generator, that lead to two separated voltage generators in series with spectral density:

$$e_{nai}^2 = \frac{i_{na}^2}{(wC_d)^2} \quad \text{and} \quad e_{na}^2 = e_{nw}^2 + \frac{A_f}{f} \tag{1.32}$$

The contribute of these noise sources to the signal noise at the output of the shaper can be obtained integrating the spectral density at the input of the preamplifier $e_{ni}^2 = e_{nd}^2 +\ e_{nb}\ {}^2 + e_{ns}^2 + e_{nai}^2 + e_{na}^2$ over all the frequency spectrum and considering the transfer function A of the shaper:

$$V_{no} =_0 \int \quad e_{ni}^2(f)\ \ A_f\ {}^2\, df \tag{1.33}$$

with

$$A\ {}^2 = \frac{\tau_d^2}{(\tau_i+\tau_d)^2 + (w\tau_i\tau_d - \frac{1}{w})^2} \tag{1.34}$$

that lead to:

$$\begin{gathered} V_{no}^2 = \frac{1}{4C_d}\Big(\frac{4kT}{R_b} + 2eI_d + i_{na}^2\Big)\frac{\tau_d^2}{\tau_i+\tau_d} + \\ \Big(4kTR_s + e_{na}^2\Big)\frac{\tau_d}{\tau_i(\tau_i+\tau_d)} + A_f\frac{\tau_d^2}{\tau_i^2+\tau_d^2}log\Big(\frac{\tau_d}{\tau_i}\Big) \end{gathered} \tag{1.35}$$

Normally, the noise is expressed in terms of Equivalent Noise Charge (ENC) which represents the charge Q_n injected in the detector volume that produces the same signal

read when no particle crosses the detector. The signal to noise ratio, then can be written in terms of either the voltage signal or the charge:

$$\frac{S}{N} = \frac{V_{so}(T_P)}{V_{no}} \quad \text{or} \quad \frac{S}{N} = \frac{Q_s}{Q_n} \tag{1.36}$$

where $V_{so}(T_P)$ is the peak value of the detected signal at the output of the shaper stage and Q_s the charge associated. Considering the CR-RC shaper with τ_d=τ_i=τ, $T_P = \tau$, the ENC due to the different noise sources can be demonstrated to be:

$$Q_n^2 = Q_s \frac{V_{no}}{V_{no}(T_P)} \qquad \underbrace{\left(2eI_d + \frac{4kT}{R_b} + 2eI_a\right) \cdot \tau}_{\text{current noise}} \quad + \quad \underbrace{\left(4kTR_s + e_{na}^2\right) \cdot \frac{C^2}{\tau}}_{\text{voltage noise}} \quad + \quad \underbrace{4A_f C^2}_{\text{1/f noise}}, \tag{1.37}$$

where C is the total capacitance at the input of the preamplifier, that is practically equal to the detector capacitance C_d. The transfer function, then, introduces a dependence to the peaking time τ. Higher peaking time would increase the current noise charge, but decrease the voltage noise charge: the lower total noise would be achieved for a value of τ that would make equal both the current and voltage components. 1/f noise results independent of the constant time. For what concern the detector, its design and technology should be developed accounting for reducing the series resistance, the leakage current and the total capacitance, as well as obtaining an high bias resistance. In this analysis a simple diode detector has been considered. The same results can be achieved considering one channel of a position sensitive detector connected to the same front-end electronics. For instance, lets consider one strip of a microstrip detector. In this case the total capacitance seen by the preamplifier input is not only the bulk capacitance. In figure 1.10, the system of capacitances connected to the electronic channels can be observed. A p^+-in-n detector AC coupled (C_{AC}) to the preamplifiers is considered. So, C_{met} is the capacitance between two adjacent metal strips, C_{imp} the capacitance between adjacent p^+ implants that can be express as $C_{imp} = a + b\frac{w+23}{p}$ with a and b two constants[1], p the pitch of the strips and w their width and finally $C_b = \frac{pl}{d}$ is the bulk capacitance with l the strip length and d the bulk thickness.

In this way the total capacitance at the preamplifier input is:

$$C_{tot} = \frac{C_{AC}C_s}{C_{AC} + C_s} \quad \text{con} \quad C_s = C_b + 2(C_{is} + C_{i+1} + C_{i+2} + \quad); \tag{1.38}$$

[1] with a=0.1 and b=1.6 for substrates 300 μm thick.

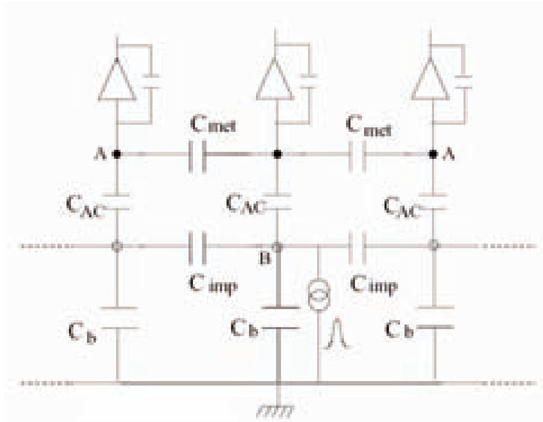

Figure 1.10: *Schematic of the capacitances system connected to the readout electronics channels of a microstrip detector . C_{met} is the capacitance between two adjacent metal strips, C_{imp} the capacitance between adjacent p^+ implants, C_{AC} is the coupling capacitance and C_b the bulk capacitance.*

where C_s account for the contribution of interstrip capacitance between first neighbouring strips (C_{is}), second neighbours (C_{i+1}), and so on. Since the coupling capacitance is normally one or two orders of magnitude higher than the other capacitances and $p < d$, the most important contribute to the total capacitance is given by the interstrip capacitance.

Further considerations on noise will be presented in section 3.3.3, where a microstrip detector with resistive coupling electrodes and read out at both sides of each strip will be considered.

1.3.3 Ballistic deficit

As seen above, the peaking time of the shaper has a relevant influence on the total noise charge. We will see in this section that another consideration in the choice of time constants is the rise time of the input pulse applied to the shaper. Figure 1.8 shows a δ signal at the output of the detector, converted in a step function with zero rise time by the ideal preamplifier. This representation is convenient when characterizing the pulse shaper alone. In reality the rise time is increased by the collection time of the detector and the limited response time of the preamplifier. In many systems the input rise time is much smaller than the shaping time, so the step input is an acceptable approximation. However, when using short peaking times as in high-luminosity collider

detectors, the sensors collection time may be a substantial fraction of the shapers peaking time. Figure 1.11 shows the shaper output response to an input rise time

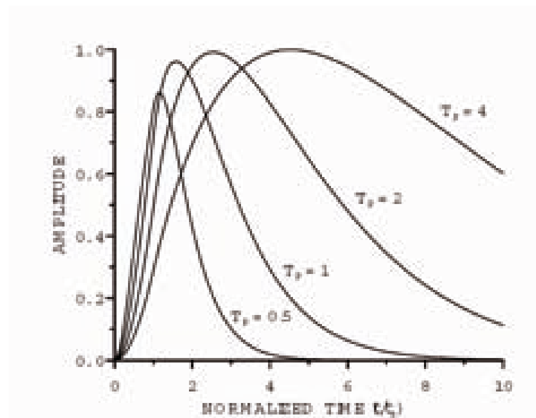

Figure 1.11: *Response of a CR-RC shaper with $\tau_d = \tau_i = T_P$ to an input rise time t_r. All times are expressed in units of the rise time t_r. The shaper peaking times T_P range from 0.5 to $4t_r$[12].*

t_r for CR-RC shapers with peaking times $(T_P)_i = \alpha_i t_r$, with α_i ranging from 0.5 to 4. The CR and RC time constants are equal. We would expect to see each output signal S_i reaching its peak at $t = (T_P)_i$. Nevertheless the finite rise time of the input delays the time of maximum signal for all shapers. This is most pronounced for the $T_P = 0.5t_r$ shaper which shows the output signal peaks at $t = 1.2t_r$. Furthermore, its peak amplitude is 14% smaller than for a step input. Since the noise level is independent of the input signal, this reduces the signal-to-noise ratio. The loss in pulse height is called "ballistic deficit". Although analytical techniques usually assume step inputs, analysis with realistic sensor pulses is advisable.

Besides the detector collection time, also the electrodes transport time can cause non-zero rise time, as for in the case of resistive electrodes. Resistive electrodes represent diffusive RC line in which a current pulse undergoes both an amplitude attenuation and an increase of the rise time the further it travels. In chapter 3 a first investigation of a novel 2D position-sensitive microstrip detector with resistive coupling electrodes will be presented. The effects of a short shaping time on a non-constant rise time will be discussed.

1.4 Applications in tracking systems

The development of position-sensitive semiconductor detectors was initiated by experimental particle physicists [24], with the purpose of obtaining a device that could recognize particle tracks with an accuracy of a few tens of microns and, at the same time, operate at interaction rates of up to 10^8Hz. Soon after their application had spread in many different fields. The experiment Mark II at the Stanford Linear Collider was the first in employing a silicon strip vertex detector [25] at a lepton collider facility. Then, a real boom of silicon vertex detectors started with the LEP collider [26]. ALEPH [27] and DELPHI [28] were equipped with a silicon vertex detector, made up of layers of double-side detectors, right from the beginning, while OPAL [29] and L3 [30] added it in later upgrade programs. CDF (Collider Detector at FermiLab) [31] at the Fermi National Accelerator Laboratory installed a silicon vertex detector early in its operation in 1987 and since then has operated a succession of upgraded detectors. The system included many layers of double-side microstrip detectors characterized by different stereo angles. Belle at KEK [32] and BaBar at SLAC [33] also use double-sided strip sensors with orthogonal strips in their vertex detectors, but the biggest tracking system totally equipped with silicon detectors is the one implemented in the CMS (Compact Muon Solenoid) [4] experiment at LHC (Large Hadron Collider) [3], where silicon sensors cover a total sensible area of about 230 m^2, organized in coaxial layers around the collision point. Divided in strip tracker detector and pixel vertex detector, the total system is read out using more than 50 millions of electronic channels. All the others experiments at LHC also include in their tracking system layers of silicon detectors: ATLAS (A Toroidal LHC ApparatuS) [5] uses strip detectors and pixel detectors, LHCb [34] strip detectors as well as TOTEM (Total Cross Section, Elastic Scattering and Diffraction Dissociation at the LHC) [35] and ALICE (A Large Ion Collider Experiment) [36] strip, pixel and drift detectors. Compactness in size of silicon position-sensitive detectors makes them also suitable for application in space experiments. For instance, the AMS (Anti Matter Spectroscope) tracker system [37] consists of eight layers of double-sided Si detectors, the Pamela (a Payload for Anti-matter Matter Exploration and Light-nuclei Astrophysics) tracker [38] is made up of 6 layers of double-sided silicon microstrip detectors and the GLAST (Gamma-ray Large Area Space Telescope) tracker [39] consists of 80 m^2 of silicon strip detectors. As seen,

different devices are used depending on many factors as the requirements of each experiment and facility or the preference/experience of the designers of/in some particular detector. For instance, a comparison between the tracker system of two general-purpose experiments (CMS and ATLAS) at the same collider facility (LHC) is shown in figure 1.12. The CMS tracker is totally equipped with silicon FZ detectors. It is divided

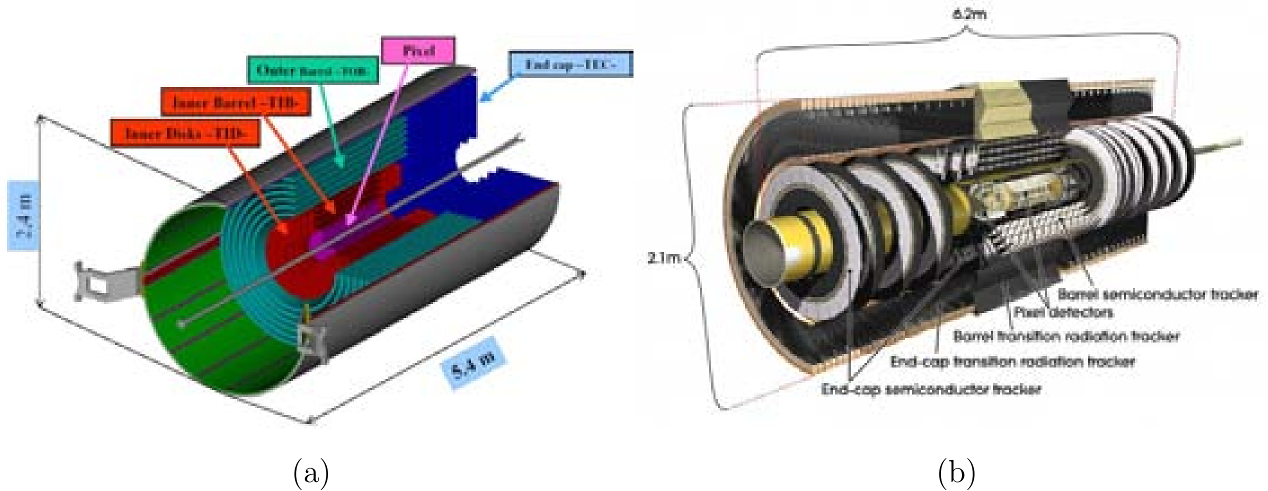

(a) (b)

Figure 1.12: *(a) Schematic of the CMS tracking system (b) Schematic of the ATLAS tracking system.*

in a vertex detector and a tracker detector. The vertex detector is composed by pixel detectors n^+-in-n mounted on three barrels with radius 4 3 cm $< r <$ 10 2 cm from the collision point and two couple of end-cup disks at $z = \pm$ 34.5 cm and $z = \pm 46.5$ cm from the collision point. The tracking system is equipped with silicon strip detectors with different pitch and thickness depending on the layer. The inner tracker consists of four barrels and two couples of three end-cup disks with detectors 320 μm thick and pitch of 80 or 120 μm. Some layers are covered with double-sided modules, obtained by mounting two single-sided detectors face to face slightly tilted. The outermost barrel includes 6 layers of microstrip detectors 500 μm thick with pitch of 122 μm or 183 μm. The tracker is then closed by two systems of end-cup disks (nine each one) where sensors with thickness of 320 or 500 μm and pitch between 81 μm e 205 μm are placed.

The ATLAS tracker adopted another strategy combining silicon DOFZ detectors with transition radiation detectors. The vertex detector is still composed by silicon pixel n^+-in-n detectors arranged in three layers with radius 5 05 cm $< r <$ 12 25 cm

from the collision point and three end-cup disks on each side between radii of 9 and 15 cm perpendicular to the beam. Outside the vertex detector, a Semiconductor Tracker (SCT) composed of silicon strip detectors with pitch 80 μm, is organized in four layers with radius 29 9 cm $< r <$ 51 4 cm and nine end-cup disks at each side. In he barrel the same double-sided modules configuration as in CMS is used. In the outer region, the tracker system is completed by a Transition Radiation Tracker (TRT), based on the use of straw detectors.

For what concern the facilities, tracking and vertex detectors at lepton colliders have to face simpler event topologies than at hadron colliders, free of the large backgrounds inherent to hadron interactions. However the momenta of the particles of interest are frequently low, so minimizing material in the active volume is crucial to limits multiple scattering enhancing leptons id. Then, lepton colliders typically have a well-localized interaction region, especially in linear colliders, allowing the tracker system to cover a limited volume around it. On the other hand, experiments at hadron colliders must deal with much higher interaction rates, which increases demands on rate capability. Since most of the interactions are background, pattern recognition is crucial, which increases the number of layers required for efficient track reconstruction. Furthermore, the interaction region tends to be much more spread out in length, so the detectors must be longer.

In general in a tracking system low mass is required to reduce multiple scattering, low noise is requested to improve S/N, thus spatial resolution and momentum resolution, fast response need to face high interaction rate, low power is desirable to reduce the costs and simplify the cooling system and finally, but not less important radiation tolerance of the components is needed to ensure a long life of the experiment.

All these requirements can not be satisfied at the same time, but exploiting the silicon versatility, different compromises can be achieved. For example, in order to reduce the system mass it is possible to thin the sensors bulk, that also improve radiation hardness of the sensor and response velocity. However thinning the sensor also lead to lower signal amplitude and higher capacitance, i.e. higher noise. A lower noise can be achieved with higher power and high rate can be faced increasing granularity, that would reduce interaction rate in each element (channel). 2D position sensitive detectors are a solution to reduce the total mass of the system. Most recent studies, then,

demonstrate the high radiation hardness of 3D detectors, which are good candidate for the CMS and ATLAS vertex detector upgrade for HL-LHC.

Finally, due to the multi-layers configuration of a silicon-based tracker, its precision in track reconstruction, thus in momentum measurement, also depends on the stability of the whole system, that can be achieved only implementing a proper alignment system. As better explain in chapter 2 a laser alignment system (like that used by CMS and AMS) provides good alignment without adding any other material to the detector.

1.4.1 Future accelerators

Looking at the future, two new big projects in high energy physics experiments call for a continuous and deeper investigation of silicon position-sensitive detectors: the upgrade of the LHC to HL-LHC and the building of the International Linear Collider (ILC) [2]. The detector technologies developed in this thesis and presented in the next chapters, find their motivations in this context, ruled by improvement and innovation urgency.

The LHC upgrade: HL-LHC

The Large Hadronic Collider (LHC) is a proton-proton collider installed at CERN [40] (Geneva), in the 27 km tunnel (figure 1.13) that firstly housed LEP, the Large Electron Positron collider. In the tunnel the two protons beams are contained in two pipes enclosed within superconductive magnets cooled by liquid helium. The beams are composed of 2808 bunches containing 10^{11} protons each one and travel in opposite directions colliding in four location along the tunnel with an centre-of-mass energy of 14 TeV. Currently LHC is working at a luminosity of $6.7\times10^{30}\text{cm}^{-2}\text{s}^{-1}$, but it is designed to reach a peak value of $10^{34}\text{cm}^{-2}\text{s}^{-1}$. For this reason the sensible components of the four experiments installed in correspondence of the collision points have been designed and fabricated so that properly work in a radiation environment characterized by a fluence of heavy particles of $10^{14}\text{n}_{eq}\text{cm}^{-2}$ at a distance of 20 cm from the interaction point (IP) and of $10^{15}\text{n}_{eq}\text{cm}^{-2}$ at about 4 cm from the IP.

The upgrade of the LHC to High Luminosity-LHC (HL-LHC) envisaged for 2020, foresee a luminosity increase from 10^{34} cm^2s^{-1} to 10^{35} cm^2s^{-1}, that will require silicon detectors in the central tracking detectors with unprecedented radiation tolerance.

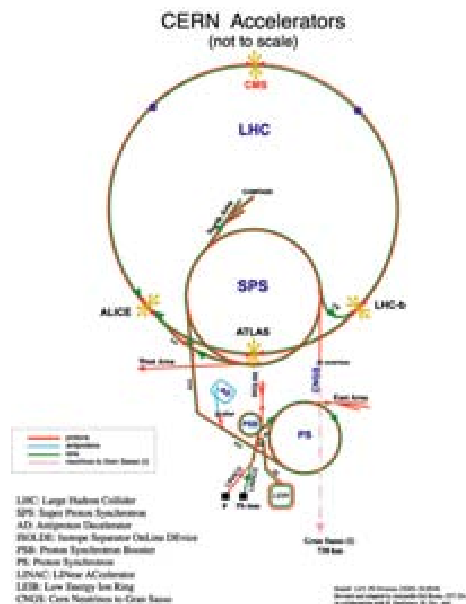

Figure 1.13: *The LHC accelerator and the beams injection system*

Current radiation field simulations for the general-purpose experiments ATLAS and CMS foresee radiation levels of around 2.0×10^{16} n$_{eq}$/cm^2 for the innermost pixel layers and 1.0×10^{15} n$_{eq}$/cm^2 for the innermost strip layers.

The luminosity can be expressed as:

$$L = \frac{\gamma f k_B N_b N_{b'}}{4\pi\epsilon_n\beta^*} \tag{1.39}$$

where γ is the Lorents factor, f is the revolution frequency and the denominator is basically the beam transverse area (β^* is the amplitude function) multilied by γ. Definition and value of the other parameters are given in table 1.1 for both accelerator, LHC and HL-LHC.

These HL-LHC fluences exceed the LHC values by about an order of magnitude, which means that with the HL-LHC, detectors in the innermost layers of the vertex and tracking systems of ATLAS and CNM have to be replaced by a new generation of highly radiation hard detectors.

CERN RD50 is an international collaboration of over 250 scientists from 47 institutes, working on semiconductor detectors to meet the challenges from high luminosity colliders and hence high radiation environments [41]. The RD50 activities are grouped into five different research lines: defect and material characterisation, defect engineering, new structures, pad detector characterisation and full detector systems. A full

Table 1.1: *Comparison between LHC and HL-LHC.*

Parameters	LHC	HL-LHC
Number of bunches, k_B	2808	up to 5616
Beam particles per one bunch N_b	1.15 10^{11}	up to 1.7 10^{11}
Other Beam particles per bunch $N_{b'}$	1.15 10^{11}	up to 1.7 10^{11}
β-value, β^* (cm)	55	up to 25
Normalized Emittance , ϵ_n (microns)	3.75	3.75
Bunch separation , Bsep (nsec)	25	up to 12.5
Energy , E(GeV/particle)	7000	up to 14000
Peak Luminosity $L_p(\mathrm{cm^2s^{-1}})$	10^{34}	10^{35}

overview of the RD50 activities and results can be found in reference [42]. Besides investigating new sensor substrates e.g. silicon Magnetic Czochralski and Epitaxial silicon or substrate doping e.g. n^+-in-p detectors, the collaboration is carrying out a systematic research on 3D detectors as they seam to be good candidate for the new pixel vertex detectors. For what concern the tracking systems, the main choose remain silicon microstrip detectors similar to the ones used in the CMS tracker, but with new features in order to face the request of an higher granularity and radiation hardness. Short strip sensors seam to be promising for the inner tracker layers.

The International Linear Collider

The International Linear Collider (ILC) is a proposed future linear electron-positron collider. Nearly 300 scientific institutions around the world are involved in the project, with more than 700 people working on accelerator design and more than 900 people working on detector developments, with the aim to give precise measurements of the Higgs and/or new physics expected to be discovered at the LHC. ILC will be probably installed in Japan and its design parameters are being defined each day more precisely. Stretching approximately 31 kilometres in length, it will consists of two linear accelerators that face each other (see figure 1.14). Superconducting accelerator cavities operating at temperatures near absolute zero will give leptons growing energy that will force them to collide to each other with a centre-of-mass energy of 500 GeV and a

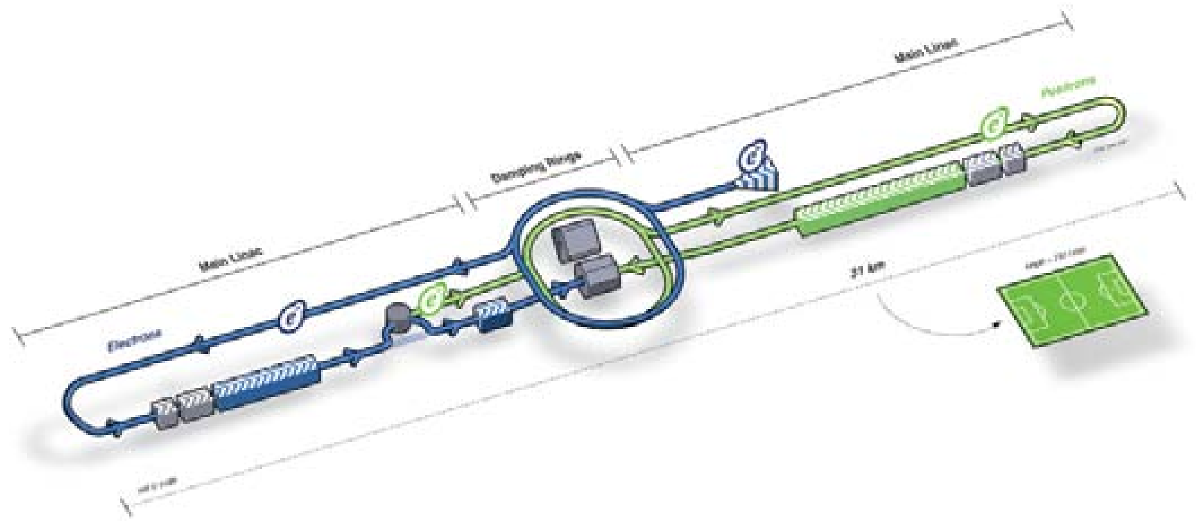

Figure 1.14: *The ILC accelerator geometry and the positrons source*

peak luminosity of $2.0{\times}10^{34}$ cm^{2}s^{-1} ($\approx$ LHC). Each beam will consist of 2625 bunches of $2{\cdot}10^{10}$ leptons and the collision frequency will be just 5 Hz, to be compared with 40 MHz of LHC. The energy of the ILC will be sufficient to produce a very large number of $t\bar{t}$ pairs, which will allow top-quark physics to be studied with unprecedented precision. The energy range of the ILC spans all predictions for the mass of a Standard Model Higgs boson based on the precision electroweak data and any supersymmetric particles found by LHC will open the eyes over a great number of new phenomena at ILC.

Tracking at the ILC has multiple challenges. The momentum resolution is the most important and difficult to achieve and it has to be matched with the need of minimal material in the tracking components to preserve lepton id and high performance calorimetry. Position resolution must be in the range 5-8 μm with excellent two hit resolution. Good S/N performance is also requested. Then, low duty cycle of the machine will allow reducing the total power spent by the electronics as well as material of the cooling systems, but an high number of readout channel is still necessary.

The ILC environment also poses significant challenges to vertex detector design. Vertex detection efficiency, angular coverage and impact parameter resolution will be very important to have a good tagging of heavy particles. Improving the point resolu-

tion per measurement and reducing the thickness of the detector sensors and supports is then advisable. The low ILC radiation load admits a much wider selection of technologies than are possible at the LHC.

SiLC (Silicon tracking for the International Linear Collider) is a generic R&D collaboration aiming to develop the next generation of large area Silicon Trackers for the ILC. The effort of the collaboration is focused on three main challenges: very high precision on momentum (10 times better than in LEP), spatial resolution (better than 4 μm, in certain regions, average 7-8 μm) and large angle coverage. The request of low material budget and low cost put constraints to whatever proposal. So, thin detectors as well as 2D position-sensitive detectors are favoured and different solutions are being investigated.

Chapter 2

IR Transparent detectors

In a semiconductor tracker detector system the precision in track reconstruction and charged particles momentum measurements depends on the spatial resolution of the sensing components as well as on the stability of the mechanical support on which the sensors are mounted. In the experiments at accelerators as well as in space experiments, many environmental disturbances cause stability of any supporting structure to be affected at the micrometer level. In the first case the detector is subject to local temperature gradients (produced by operation and cooling of detectors) or humidity changes while, in the second one, it undergoes vibrations during the transport before deployment and rapid periodic changes in the thermal settings due to solar radiation and cooling while in the shadow of Earth. Improving mechanical stability is currently out of the technological reach, so other solutions have to be considered. The successful experiences of the experiments AMS and CMS demonstrate that a Laser Alignment System (LAS) is an elegant solution to achieve relative alignment between modules to better than few microns. As shown in figure 2.1 it basically consists in a IR laser beam, generated out of the tracker detectors nutshell, which traverses consecutive layers of silicon microstrip sensors. The beam plays the role of an infinite momentum track, not bent by magnetic field and even if silicon is almost transparent to IR light, its absorption is enough to produce a signal that the sensors DAQ electronics can read directly: beam position across several sensors can thus be monitored. Using the sensors as their own alignment system, no mechanical transfer errors between fiducial marks and the modules are introduced, neither additional material or costs are needed, that assure a minimum impact on the system integration.

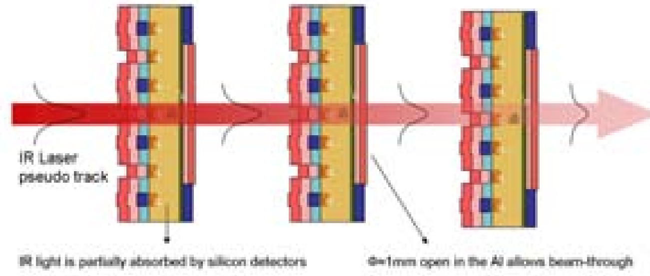

Figure 2.1: *Laser Alignment System concept. The laser beam traverses consecutive layers of silicon microstrip sensors producing a signal the sensors DAQ electronics can read directly, allowing its tack reconstruction i.e. the sensors alignment. The higher transmittance of the detectors, the more modules can be aligned with a single beam.*

This chapter relates the upgrade of dedicated sensors for an equivalent laser alignment system, focusing the attention on the detectors transmittance to the IR light. The higher transmittance of the detectors, the more modules can be aligned with a single beam and then the simpler the system becomes. Following the experience of the cited experiments, in addition to open a window in the metal backelectrode of the interested sensors, both geometrical and technological parameters have to be tuned in order to maximize transmission to the laser light without affecting detection efficiency. With the purpose of understanding the influence of different parameters on light transmission, a complete model of a microstrip detector has been developed by the IFCA group of experimental physics in Santander and the passage of a coherent beam of light through its active volume has been simulated identifying the minimum changes in the design and technology to maximize the transmittance. Then I have designed the mask of the first prototypes and have been in charge of production in the IMB-CNM clean room facilities in Barcelona, where I carried out a technology monitoring at different steps of the processes flow. The transmittance and the reflectance have been measured at intermediate steps as well as at the end of the fabrication process. In this chapter the development of the sensors and the final results of their characterization are presented.

This project has been a collaborative effort between the Physics Institute from Cantabria (IFCA), whose researchers have developed and carried out the simulation study and the IMB-CNM of Barcelona where the prototypes of the simulated detectors have been design, produced and tested. The whole work has been realized within the SiLC R&D collaboration, a generic R&D collaboration with the aim of developing the

next generation of large area Silicon trackers especially suited for performing very high precision measurements in spatial position and momentum at the International Linear Collider (ILC) machine (see section 1.4.1).

2.1 Laser alignment for tracking systems

Before introducing the new detectors, the choices adopted by the previous experiments will be briefly presented in this section together with the results obtained.

2.1.1 AMS Tracker Alignment System

The AMS tracker consists of 8 layers of double-sided 300 μm thick Si strip detectors. The strip (readout) pitch is 27.5 (110) μm for the p-type side and 104 (208) μm for the n-type side. The alignment system is equipped with 2×10 pairs of beams at $\lambda = 1082$ nm crossing selected sensors in each layer. For these sensors windows in the aluminium backelectrode has been created in order to allow the beams pass through the whole detector towards the next one. Then, the readout strip metallizationzation has been narrowed to 10 μm width and removed from the implants not used for the readout. Passivation layers of SiO_2 and Si_3O_4 have been deposited on both sides of the detectors as Anti-Reflection Coating (ARC). The final transmittance achieved for these devices is above 50%.

2.1.2 CMS Tracker Alignment System

CMS tracker components vary depending on the region of the multi-layer system they occupy: they are single-sided p^+-on-n strip detectors whose thickness range between 320 and 500 μm and strip pitch between 80 and 205 μm. Strip width/pitch is a constant parameter for every detector, including the ones dedicated for the alignment system, whose metallizations have not been narrowed. In this case, the only modification made to these detectors was opening a circular window in the backside ohmic contact and coating it with an ARC made of selected thickness of Ta_2O_5 and SiO_2. The system employs a total of 40 laser diodes working at $\lambda = 1075\pm3$ nm. The resultant transmittance at the AMS working wavelength is 21%.

2.2 Full simulation of the passage of light through a microstrip detector

With a view to the integration of the alignment concept in the fabrication process of the device, optical properties of a complete strip detector have been investigated considering structural characteristics and materials composition alike. In this section the development of the optical model of the sensor will be explained and the results of the simulation of a laser beam passing through its active volume will be discussed.

2.2.1 Starting point: optical representation of a microstrip detector

A silicon microstrip detector, from an optical point of view, is a complex superposition of different materials layers grown or deposited on the substrate, in order to create and insulate from each other the strips diodes and their electrodes.

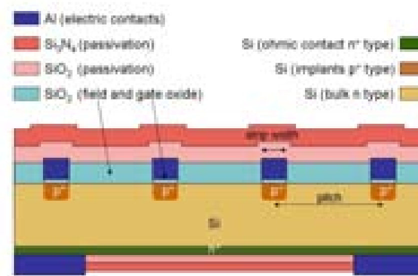

Figure 2.2: *Schematic cross section of a microstrip detector. Geometrical and technological characteristics of optical interest are shown. Drawing not to scale.*

Figure 2.2 shows a schematic cross section of a standard CNM detector in which a circular window has been opened in the metal backcontact. The p^+ strips are implanted on a n-type bulk 300 μm thick and AC coupled with metal contacts through a thin layer (normally 36.5 nm) of silicon dioxide (gate oxide). A thicker thermal oxide layer ($\approx$1 μm) is grown in order to insulate the electrodes from each other. The upper surface is finally passivated with a SiO_2 and Si_3N_4 coating with a thickness of the order of hundreds of nanometres. On the backside, the window in the metal contact is passivated in the same way.

Silicon, Aluminium, Silicon Dioxide and Silicon Nitride can be considered as homogeneous and isotropic optical media. Any medium like this is totally characterized by its complex refraction index: $N(\lambda) = n - ik$, where k is the so-called *optical extinction coefficient*. When radiation traverses the medium, its intensity is attenuated to 1 e of its initial value after a distance given by

$$\frac{1}{\alpha} = \frac{\lambda}{4\pi k} \tag{2.1}$$

where α is the so-called *absorption coefficient* and has the units of inverse distance.

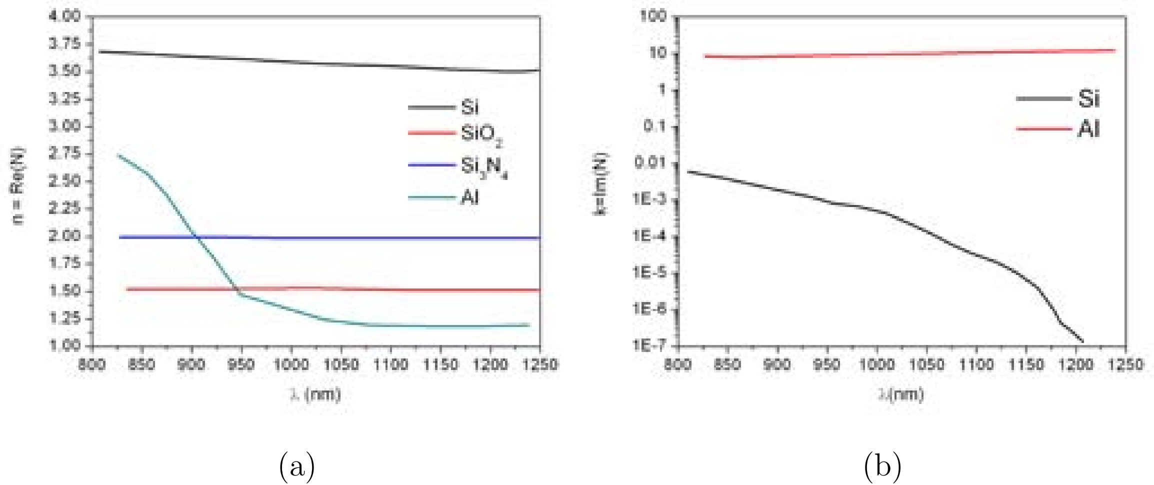

(a) (b)

Figure 2.3: *Real part (a) and Imaginary part (b) of the refraction index of the materials involved in a silicon microstrip detector fabrication.*

Materials with a numerically high extinction coefficient k are less transparent than those with lower values, e.g. 1 μm thickness of Al attenuates the equivalent of 10^5 μm of Si at $\lambda = 1$ μm, while SiO_2 and Si_3N_4 are not absorbing materials (k = 0). A comparison of the real and imaginary part of the refraction index around the wavelength range of interest is shown in figures 2.3 (a) and (b) respectively [46], [47], for different materials.

When a laser beam passes through the detector, its energy will be partially absorbed, reflected and transmitted, in a proportion that depends on the sequence and thickness of the materials traversed as well as on the obstacles found along its way. Silicon displays moderate absorption in the NIR range, slightly above its band gap (1 μm). Thus, laser beams above that wavelength are able to traverse 300 μm of Si. The rest of layers of the sensor have thickness comparable to this wavelength. That is

the reason why small changes in the thickness of the materials can have an impact on the overall transmittance of the detector changing the refraction angle of the incoming beam.

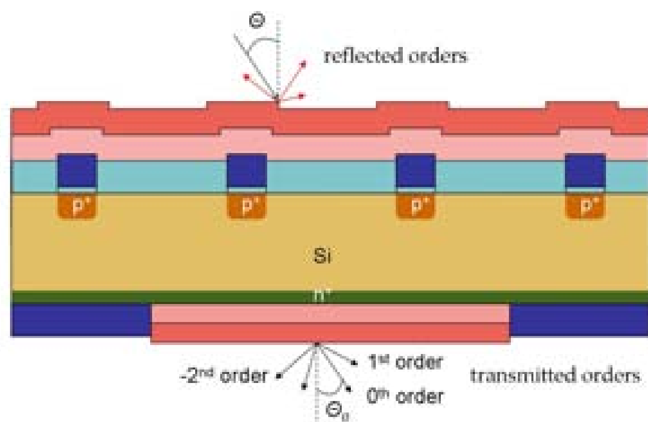

Figure 2.4: *Representation of the incoming energy splitter between reflected (red arrows) and transmitted (black arrows) directions. Only a few refraction orders have been drawn.*

When the light impinges on the interface between two homogeneous media with different refraction index, the energy is split between reflected and transmitted waves. The segmentation of the strip electrodes then forces all the layers above them to adapt to the underlying orography, converting the detector surface in a discontinuous layer, that will act as a linear grating. Considering the incoming light as a plane wave, the propagating directions of the refracted waves are given by a grating equation of the form (see figure 2.4):

$$sin\Theta_m \ = \ sin\Theta \ + \ m\frac{\lambda}{d} \tag{2.2}$$

where Θ is the incident angle, Θ_m the diffraction angle, λ the wavelength in air, m the order of diffraction (integer number) and d the pitch. Consecutive layers act as overlapping diffraction gratings. The beam then is reflected and transmitted in a discrete set of directions each time the interface between 2 adjacent media is traversed. Once reached the last boundary, after crossing the bulk volume, some light will be reflected back too. So, transmitted and reflected waves will interfere many times between each other travelling through the sensor by different paths, causing the beam intensity distribution across the detector to finally show interferential maxima and minima.

A faithful simulation of light propagation in a real detector consists in a precise calculation of the final amount of transmitted, reflected and absorbed energy, by solving

Maxwell s equations in the input, grating and output regions fulfilling the boundary conditions for the tangential electric and magnetic field components at the respective interfaces [43]. Two open source programs, from the photonics group of the Department of Information Technology at Ghent University (Belgium), RODIS and CAMFR [44] [45], have been employed for this purpose.

At this first stage, optical characteristics of the materials involved in the sensor schematics have been taken from literature: refractive index of SiO_2, Si_3O_4, Al from reference [46]; precision measurements of Silicon within the absorption gap from reference [47].

Figure 2.5: *Picture of the wafers used to crosscheck doped silicon properties defined in literature and the simulation tool. Left to right , top to bottom: a reference wafer without doping implants, wafer with increasing doping concentration. Different thickness of SiO_2 and Si_3N_4 are deposited on the four quadrants of the wafers.*

Optical properties of doped Si are reported to be very different from intrinsic Si (see

for instance [48]). In order to crosscheck these measurements and validate the simulation tool, many wafers produced at CNM within the GICSERV access framework have been used [49] [50]. Four double-side polished wafers have been used to implant on one surface boron atoms with increasing doping concentrations and total thickness of 1 μm. The wafers have been measured with a grating spectrometer (1.2 nm spectral resolution) operating in the wavelength range 950-1150 nm. Contrary to what was expected, the same light transmittance has been measured from all the wafers regardless of doping concentration. The different thicknesses of SiO_2 and Si_3N_4 have been deposited on the four quadrants of each wafer in order to study their optical properties. A picture of all the wafers used for this test is shown in figure 2.5. Simulation of the diffraction effects due to the metal strips has been tested by means of known structures of metal strips 1 μm thick, 30 μm wide and with a pitch of 80 μm deposited on a thin film of silicon dioxide (36.5 nm) grown on a silicon bulk (285$\pm$15) μm thick (bottom wafer in figure 2.5). The simulation has been carried out keeping 40 diffraction orders in the calculation and assuming a roughness $\approx$ 45 nm for the aluminium (measured by an Atomic Force Microscopy (AFM)), that accounts for decreasing of specular reflectance, (see section 2.4.2).

2.2.2 Preliminary optimization of the design

The full optical tool presented in section 2.2.1 has been used to study the key parameters that determine the transmittance of the detector to the IR light. Both layout parameters and material layers thickness have been taken into account.

At first, the thicknesses of the material layers were fixed to the ones of the standard CNM fabrication process [53] and the attention was focused on the effects of the grating parameters.

Figure 2.6 shows how the simulated transmittance changes as a function of the pitch and of the (metal) strip-width of the sensor: the transmittance increases for larger strip pitches at a fixed value of the strip width and for a smaller strip width at a fixed pitch value. For a baseline pitch of 50 μm (fixed by the SiLC Collaboration for the experiment at the ILC) a metal strip width $\leq$ 5 μm (strip-width/pitch ratio $\leq$ 10%) optimizes the transmittance.

In a second time, these geometrical parameters were fixed and the same structure

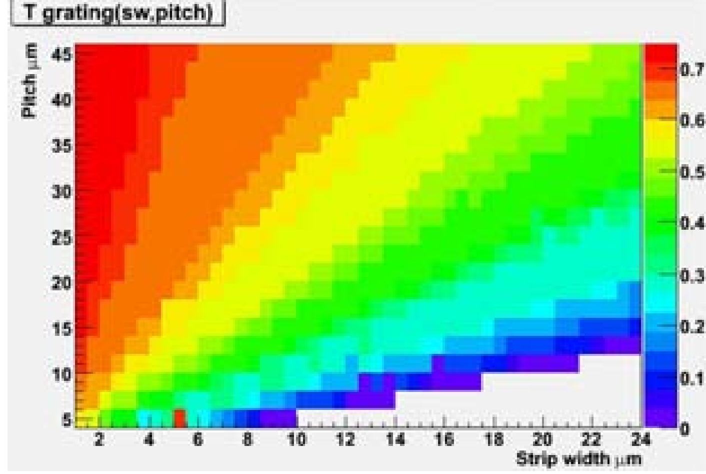

Figure 2.6: *Transmittance as a function of the relative values of strip pitch and metal width.*

was simulated, adjusting the thicknesses of the different material layers. The choice of layers thickness was constrained by some IMB-CNM design guidelines especially for what concern the thickness of field oxide, electrodes and gate oxide. Top and bottom passivation thickness were forced to vary with less restrictions. Furthermore, thick (>1 μm) layers of Si_3N_4 are not advised due to the different thermal expansion coefficient of the nitride compared to silicon, leading to overstress of the wafers (see section 2.4.3). The set of thickness values that fullfil these constraints and still lead to maximum transmittance are presented in table 2.1.

Table 2.1: *Set of optimized thickness leading to maximum %T on 50 μm pitch microstrip detectors.*

Layer	Si_3N_4 Top	SiO_2 Top	Al	SiO_2 Field oxide	SiO_2 Gate oxide	Si bulk	SiO_2 Bottom	Si_3N_4 Bottom
thickness (nm)	1046	1006	950	1000	47.5	285×10^3	1020	1005

Calculated values of Transmittance (%T), Reflectance (%R) and Absorption (%A) are depicted in figure 2.7 in the range of wavelengths of interest, for a detector with strip width 15 μm, metal width 3 μm and 1 intermediate strip. (see the detectors layout in the next section). Notice that transmittance reachs its maximum when reflectance reachs its minimum. Thicknesses of the material layers have been considered with a precision of 5%. The same precision, i.e. uniformity within the detector (wafer) surface,

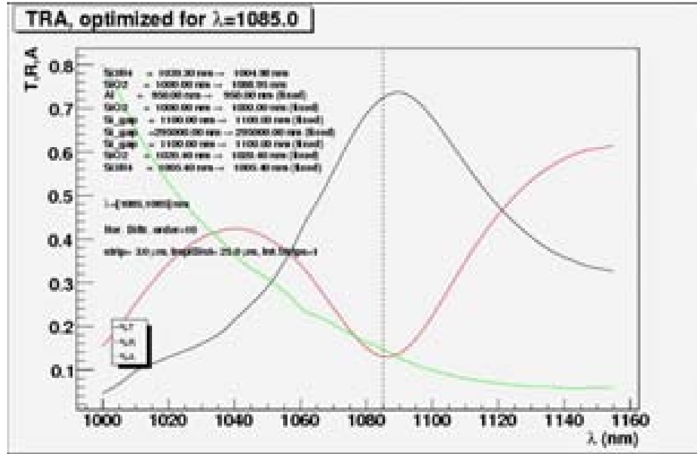

Figure 2.7: *Values of Transmittance (%T) (black line), Reflectance (%R) (red line)and Absorption (%A) (green line) calculated in the range of wavelengths of interest. Transmittance has been maximized (reflectance minimized) for λ = 1085 nm (vertival line) setting the thickness of the different materials to the values listed in table 2.1.*

is thus requested to the fabrication process used to grow or deposit the real materials to garantee the reproducibility of the sensor optical characteristics in a bunch of wafers.

2.3 Layout of the detectors

The layout for the first prototype detectors has been designed respecting simulation hints. Mask design includes twelve baby sensors equipped with 256 readout strips with a pitch of 50 μm. The active area is about 1.2 $\times$ 1.5 cm^2 surrounded by nine guard rings. A circular window (1 cm diameter) has been opened in the aluminium backplane to allow the laser beam passing through. The width of the aluminium electrodes and p$^+$-implants were varied from sensor to sensor within the wafer to study the dependence of transmittance and electrical behaviours on these layout parameters. Figure 2.8 shows the arrangement of sensors in the wafer and their characteristics.

The layout of the 6 sensors in the upper half (S1-S6) includes intermediate strips without aluminium coating (one within two readout strips), that have the function of increasing the spatial resolution by means of capacitive charge division.

For instance, details of the layout of sensor S4 and S6 can be seen in figure 2.9 (a) and (b) respectively. In both cases, superposition of mask levels (better described in the next section) are depicted: among all, one can recognize the metal coating of strips

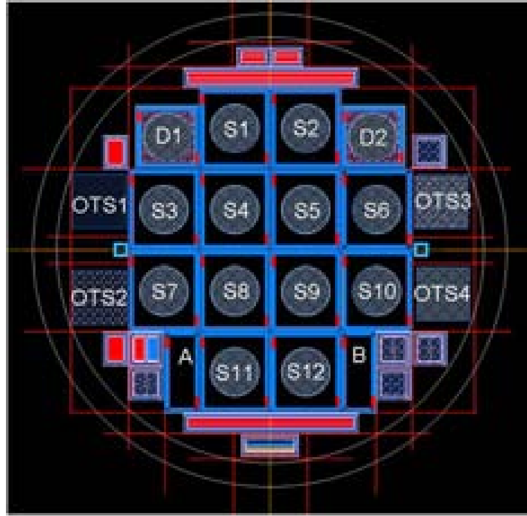

(a)

Sensor	Implant width	Metal width	Inter. strips
S1	15um	10um	1
S2	15um	15um	1
S3	17.5um	5um	1
S4	15um	5um	1
S5	15um	3um	1
S6	12.5um	5um	1
S7	12.5um	5um	no
S8	15um	5um	no
S9	15um	3um	no
S10	17.5um	5um	no
S11	15um	10um	no
12	15um	15um	no

(b)

Figure 2.8: *Mask design for the sensors production (a). Layout specifications are listed in the table on the right (b). Diode structures D1, D2 are included in the mask as well as optical test structures (TS1-TS4) and other electrical test structures. Sensors A and B are described in chapter 3.*

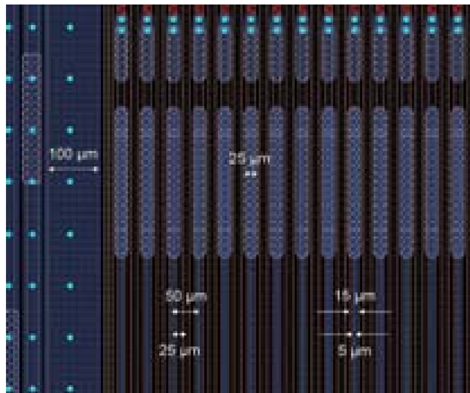

(a)

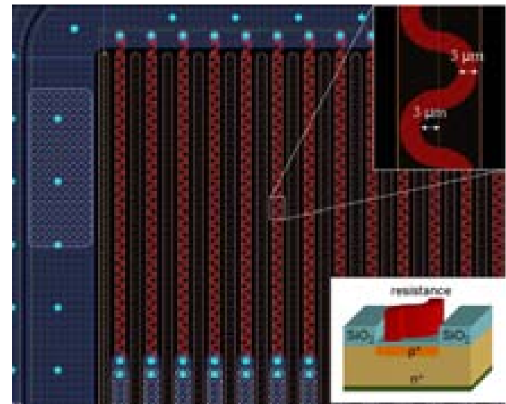

(b)

Figure 2.9: *Details of the mask design of sensor S4 (a) and S6 (b). On the left, the implant (readout) pitch and implant (metal coating) width are indicated while on the right the design of bias resistance is shown.*

and bias (guard) ring colored in blue, the p^+ implants drawn in yellow (borders and dots inside), and the polysilicon bias resistors in red. On the left, dimensions of interest are indicated like the implants (readout) pitch (25 μm, 50 μm) and the implants and metal coating width (15 μm, 5 μm). On the right, the attention is focused on the bias resistors. They have been designed adapting their geometry to the orography

of silicon dioxide on which polysilicon is deposited (see drawing within the figure), aiming a proper value of the resistance while keeping limited their total length and respecting photolithography precision limits for microelectronic processes set to 3μm (see section 2.4.5). The intermediate strips are connected to the bias ring on the other end, in order to further preserve resistances from shorting.

Referring to figure 2.8 (a), one leftmost and one rightmost structures in the top row (Diode 1 and 2) are control diodes. Unpatterned optical test structures (OTS1 to OTS4) are placed in rows second and third. These structures, described in section 2.6, allow to extract and monitor optical constants (refraction index and thickness) of the materials employed in the production.

Finally, these wafers also include test structures designed by HEPHY-Vienna [51] for CMS experiment (that can be used for indirect measurements of the detectors electrical parameters) and prototype sensors with polysilicon strips to investigate tracking by charge division that will be the subject of chapter 3.

2.4 Fabrication process and technology monitoring

Silicon detectors fabrication processing uses the same techniques and hardwares developed in the last fifty years by the semiconductor industry. The IMB-CNM clean room facility with a surface of 1500 m^2 has the capability of fabricating integrated devices with CMOS processes and includes microsystem-specific and nanofabrication processes.

The detectors described in this chapter have been processed on float-zone n-type silicon wafers by Topsil [52] with $< 100 >$ crystal orientation. Their nominal thickness is 285 ± 15 μm and resistivity between 5 and 7 kΩ·cm.

As mention in section 2.2.1, the finished device results from the superposition of different grown or deposited material layers on which structures are defined by photolithography processes. Photolithography is the patterning process that transfers the design layout from the mask to the photoresist on the wafer surface. It is the most crucial process step, since the device design is transferred to the wafer by either etch or implantation through the pattern defined on the photoresist. It requires high resolution, high sensitivity, low defect density and precise alignment between different level of

the mask, in order to guarantee high quality of the device. The IMB-CNM clean room

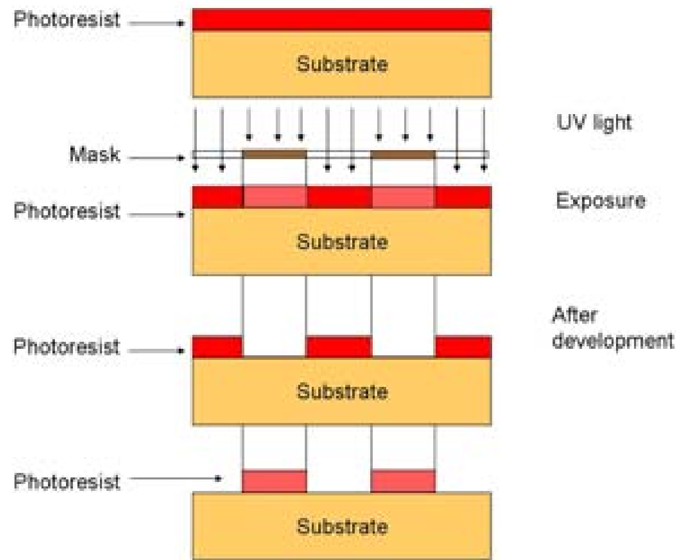

Figure 2.10: *Main steps of the photolithography process. Both positive and negative photoresists are shown.*

instrumentation for microelectronics processes can achieve a minimum feature size of 2.5 μm. The photolithography process can be subdivided into three main operations: photoresist coating, alignment and exposure and photoresist development. First, the wafer surface is coated with a thin layer of photosensitive material (see figure 2.10), called *photoresist*, which is exposed to ultraviolet light through a mask or reticle with the pattern of clear and dark areas generated by the plotter based on the device design. The chemistry of the exposed areas will change under photochemical reactions. For the positive photoresist the exposed areas will be dissolved in the developer solution, while for negative photoresist the exposed areas become cross-linked and polymerized on the wafer surface after development.

For the transparent detectors fabrication a mask made up of 9 levels (see table 2.2) has been used, corresponding each one to a photolithography process step.

A bunch of 5 wafers has been processed using the mask described above and the standard flow of processes developed by the the IMB-CNM radiation detectors group for the fabrication of silicon microstrip detectors [53]. A wafer populated with detectors without any window in the back electrode has been fabricated too as a reference. Deposition parameters have been set to obtain the material layers thickness required

Table 2.2: *Mask levels for the IR transparent detector fabrication run carried out at the IMB-CNM clean room facilities.*

Level	Pattern	Comments
N-DIFF	channel stopper	phosphorus implantation along the device cutline
P-DIFF	p^+ implants	p^+ strips implantation
POLY CONTACTS	polysilicon contacts	high doping region for polysilicon/metal contacts
POLY	resistors	definition of resistors shape
WINDOW	metal/silicon DC contacts	windows through the gate oxide for DC contacts
METAL	metal contacts	shape definition of the metal contacts
BACK METAL	circular window	opening the circular window in the backcontact
PASSIV	metal pads	opening windows on the metal connection pads
BACK WINDOW	back contact	etching the back passivation around the circular window

by the simulation for the transmittance optimization to the IR light. Monitoring steps have been added in order to measure the real thickness after each oxidation or deposition process in order to verify their values and uniformity over the detectors set: a precision of 5% ensures reproducibility of devices with the same optical characteristics.

In the following subsections the materials involved in the fabrication of the transparent detectors will be introduced, focusing the attention on their characteristics. Their applications will be explained within the mean processes carried out in the detector fabrication as well as the results of the process monitoring. Many informations used to write this section have been extracted from Introduction to Semiconductor Devices Manufacturing technology by Hong Xiao [54].

2.4.1 Thermal grown silcon dioxide

Dry and wet oxidation

Silicon is very reactive to oxygen, thus, in nature most of silicon exists in the form of silicon dioxide, SiO_2, such as quartz sand. Even when bare silicon is exposed to the atmosphere, it reacts almost immediately with oxygen or moistures in the air and

forms a thin (10-20 $\mathring{A}$) film of silicon dioxide called *native oxide* able to stop oxidation at room temperature. Silicon dioxide, is a very stable and strong dielectric material easily formed by high-temperature process, which is one of the reason why silicon is so largely used in the semiconductor industry. Oxidation is an adding process in which oxygen reacts with the silicon substrate surface forming a solid silicon dioxide layer. While the dioxide layer is growing, it consumes the silicon surface, approximately a 45% of the final thickness of the oxide. When the oxide has just started to grow and the oxide layer is very thin ($< 500\mathring{A}$), oxygen molecules can penetrate the oxide with few collisions in the oxide layer and reach the silicon to react and continue to grow the silicon dioxide film. In this first step, called the *linear growth regime*, the oxide thickness is linearly increasing with the growth time. When the oxide film become thicker, oxygen molecules have to diffuse across the growing oxide to reach silicon and react. In this called *diffusion-limited regime*, the reaction rate is considerably slower. The two regimes can be described respectively as follow:

$$X = \frac{B}{A}t \qquad X = \overline{Bt} \tag{2.3}$$

where X is the Oxide thickness, t the oxidation time and A and B are two coefficients related to oxide growth rate, which are determined by many factors, such as oxidation temperature, oxidation source (O_2 or H_2O), silicon crystal orientation, dopant type and concentration, pressure, etc... Quality of the grown film also depends on many factors. In the limits imposed by the process hardware (quartz tubes start to sag at 1150°C), the higher the temperature, the faster the oxidation and the higher the quality of the film. For what concern oxygen sources, dry oxidation with O_2 is sensible slower than wet oxidation with H_2O, but at the same time the film quality obtained is higher. Therefore thin oxide layers are normally grown in a dry atmosphere, while thick ones are usually grown in a wet process. The chemical reactions are respectively:

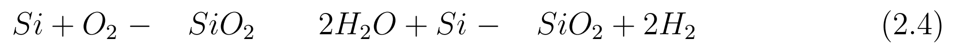

$$Si + O_2 - \quad SiO_2 \qquad 2H_2O + Si - \quad SiO_2 + 2H_2 \tag{2.4}$$

Oxidation process normally operates at temperature around 1000°C, temperature at which crystallization of SiO_2 is favoured especially in presence of defects or moisture in the Silicon surface. For this reason before an oxidation process a cleaning procedure of the wafer has always to be performed. Then, to achieve high quality of the layer,

special attention has to be paid to the resultant silicon-silicon dioxide interface, where always dangling bonds are left because of the crystal structure mismatch, as shown in figure 2.11. These dangling bonds induce so-called interface state charge, which is positive charge that affect the performance of the device (section 1.2.4). Therefore, in dry oxidation, proper concentration of HCl is commonly used for chlorine property of integrating into silicon dioxide layer and binding with silicon at silicon-silicon dioxide interface.

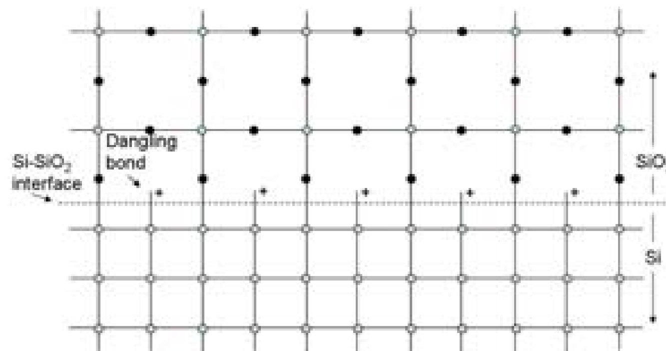

Figure 2.11: *Dangling bonds at the silicon-silicon dioxide interface. Full circles represents oxygen atoms while empty ones represents silicon atoms.*

Using vaporized H_2O instead of O_2 as the oxygen source, steam oxide can be obtained by means of a faster oxidation. The disadvantage is a less quality of the oxide. For this reason after the initial temperature ramp-up and temperature stabilization steps of the wet process, O_2 flows are used to help growing a thin layer (few hundreds $\AA$) of better quality oxide on the wafer surface as a barrier layer for the less-high quality steam oxide and to reduce defects at the silicon-silicon dioxide interface. In the same way before the final temperature ramp-down a dry oxidation is used to define a better final silicon -silicon oxide interface.

Oxidation is not selective on the wafer surface. In each process SiO_2 grows in both sides of the substrate.

Silicon dioxide grown by both dry and wet oxidation show the same optical characteristic, with refraction index like in figure 2.3

Applications to the detector processing

The fabrication process of the detectors presented in this chapter starts with a general cleaning of the wafers to remove impurities from the surface followed by the growth and etching of 400 nm of silicon oxide on both sides: removing native oxide and defects from the wafer surfaces prepares them to the other processes.

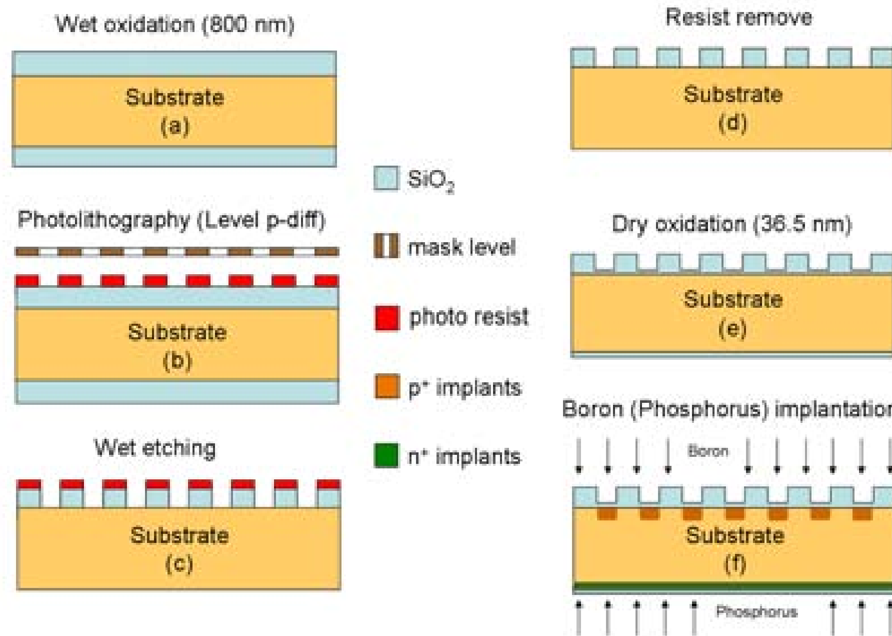

Figure 2.12: *Consecutive processes involving thermal oxide in the detectors fabrication.*

Following the schematics depicted in figure 2.12 from the top left to the bottom right, the first adding process is a wet oxidation at 1100°C to grow 1 μm of silicon dioxide (a), the so-called field oxide. It is selectively removed by means of a photolithography process (b) followed by a wet etch (c), that opens the grooves for p-type implants formation and remove the oxide from the back side. After removing the resist (photoresist) (d), a dry oxidation at 950°C is used to grow a dioxide layer 470 $\AA$ thick (gate oxide) (e) on the bare region of the substrate surfaces. The thin film will act as a screen layer on silicon surfaces, front and back side, during ion implantation of Boron and Phosphorus respectively (f).

Ion implantation is an adding process by which dopant atoms are forcefully added into the silicon substrate in the form of energetic ion beam injection. Ions penetrate the target, gradually lose their energy through collisions with the atoms in the substrate

and eventually rest inside the substrate. The distance reached from the substrate surface, the so-called *projected range*, depends on the energy of the ions, and generally for a monoenergetic beam has a Gaussian distribution, because of different path each ion follows. Due to the single-crystal structure of the silicon wafer, channeling effect can interest ions impinging vertically on the silicon surface, letting them penetrate deeply into the substrate, originating tails in the dopant distribution, i.e. anomalies in the semiconductor junction. Implantation through a thin layer of screen silicon dioxide (in this case the same 470 $\mathring{A}$ thick gate oxide) can reduce this effect. Crossing an amorphous material, implanted ions collide with and scatter silicon and oxygen atoms reaching the silicon crystal with a different pitch angle. Moreover, channeling can be reduced using a non zero tilt angle (7° in our process) during implantation. A thicker layer of silicon dioxide, 1 μm thick field oxide, acts as a barrier for ions, totally screening substrate regions under its pattern, so the process does not need any other protection on the surface. A final high temperature annealing helps recovering silicon lattice damages close to the surface and diffuse and activate dopants into the substrate. Table 2.3 summarizes the parameters of ion implantation processes included in the detectors fabrication.

Table 2.3: *Parameters of ion implantation.*

Dopant	Dose [at/cm^2]	Energy [keV]	Final conc. [at/cm^2]	Junction depth [μm]
Boron	1.5×10^{14}	100	$\approx10^{20}$	≈1
Phosphorus	1×10^{13}	50	$\approx10^{19}$	≈1

Process monitoring

Thickness and uniformity of field and gate oxide on the front side of the wafers have been measured with the use of a NANOSPEC 6100 spectroscopic reflectometer able to measure the thicknesses of up to three different layers of transparent materials. Measurements took place in the same clean room facilities where the fabrication processes were carried out, preserving wafers from external contamination. For each wafer measurements have been performed in 5 different points distributed within its surface.

Mean values obtained for all the wafers are shown in table 2.4. Values expected were

Table 2.4: *Mean values of field oxide and gate oxide measured on all the wafers*

Wafer	Field oxide [$\AA$]	Gate oxide [$\AA$]
1	10027	495
2	9965	438
3	10025	492
4	10026	490
5	10013	490

(10000) $\AA$ for the field oxide and (470) $\AA$ for the gate oxide, both with a precision of 5%. Uniformity achieved within all the wafer surfaces is around 2‰ for field oxide and 3% for the gate oxide.

2.4.2 Metallization with aluminium alloy

Sputtered Al-0.5%Cu

Aluminium is the forth-best electrical conducting metal (resistivity = 2.65 $\mu\Omega$·cm), after silver, copper silver and gold. But it is the only one of the four that can be easily dry etched to form tiny metal interconnection lines. Metallic aluminium is a polycrystalline material, which consists of many small monocrystalline grains. When electric current flows through an aluminium line, a stream of electrons constantly bombards the grains causing *electromigration* of the smaller grains. This effect creates points along the line of higher current density that can generate heat that eventually causes the breakdown of the metal line. When a small percent of copper is alloyed with aluminium, its electromigration resistance can be significantly improved, since copper acts as a glue between the aluminium grains and prevents them from migration. The higher the concentration of copper, the better the electromigration resistance. However higher concentrations of copper make metal etching more difficult. For these reasons in our silicon detector fabrication, aluminium alloy with copper (Al-0.5%Cu) is normally used in the metallization processes to make conducting lines on the strips to transport signals, metal contacts for the connection with the electronics and any

other conductive layer in the devices. Sputtering deposition is the physical vapour deposition (PVD) process used for metallization. It consists in bombarding a target of the aluminium alloy with highly accelerated ions from an argon plasma. Repeated collisions generate atoms dislodging from the target surface. These free atoms travel inside the vacuum in the form of metal vapour. When they reach the surface of the wafer, they move on it clustering around nucleation sites in single-crystal structure, generating the grains. When the grains grow and meet with other grains, they form a continuous polycrystalline metal thin film. The border between grains can scatter electron flows and cause higher resistivity. So the bigger the grains, the better the conductivity. Dimension of the grains also influences reflectivity of the metal film: the smaller the grains, the higher the reflectivity. High reflectivity of the metal layer is normally undesirable because it affects the precision of the pattern definition through the photolithography process. In this particular case lower reflectivity translate also into higher transmittance of the laser light for the alignment system. The grain size is mainly determined by surface mobility of the atoms during the sputtering process, which is related to many factors, such as wafer temperature. Normally higher temperature results in larger-sized grains. Since a metal film with large grain size is hard to etch with smooth sidewalls, it is preferred to deposit the metal with smaller grain size at lower temperatures and anneal the film at higher temperature after the metal etch and photoresist strip. Melting point of aluminium is relatively low, 660°C, so after metallization processes on the wafer, any other thermal process exceeding 450°C is forbidden.

Metallization process steps

The first metal layer is deposited just after the processes dedicated to the bias resistors formation, that will be explained in section 2.4.5. The main processes are depicted in figures 2.13 and 2.14. Starting from figure 2.13, the aluminium alloy with copper is sputtered on the front side to form a layer 950 nm thick (a), on which a photolytography (b) and a wet etching processes (c) are then used to define the strips on the implants. Figures refers to the particular case of a detector (S5) with intermediate strips and implants (metal) width equal to 15 (5) μm. Meanwhile, the back surface of the wafer is protected by a thin (470 $\mathring{A}$) film of silicon dioxide covered

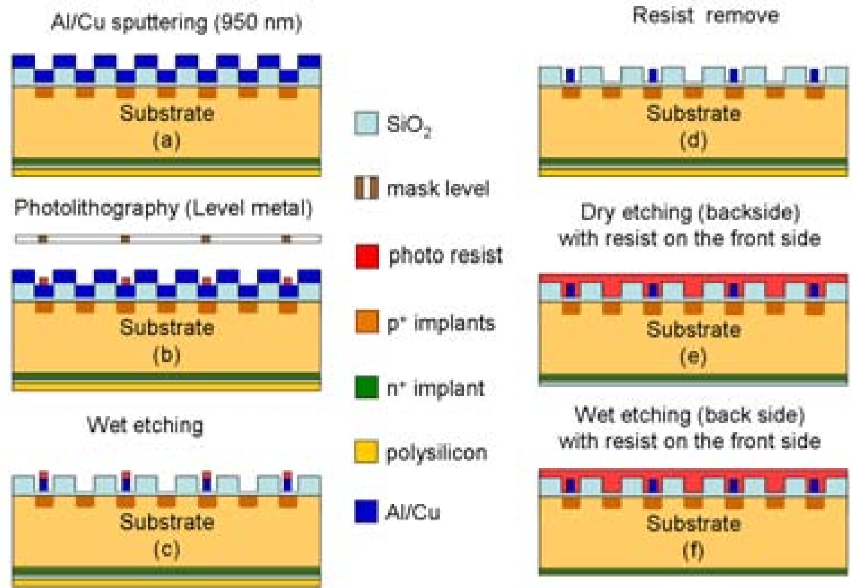

Figure 2.13: *First steps of the metallizations in the front side and in the back side of the detectors.*

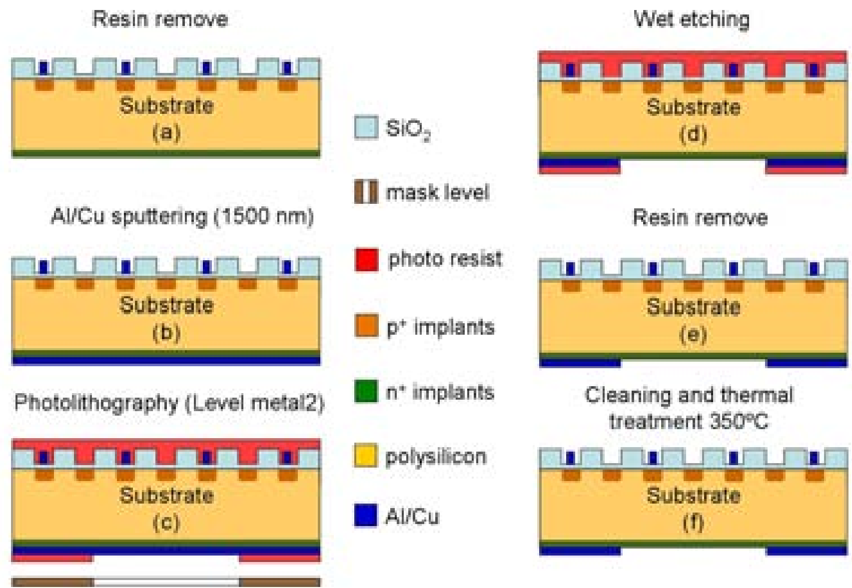

Figure 2.14: *Final steps of the metallizations in the front and in the back side of the detectors. The process flow immediately follows the last step presented in figure 2.13*

by a thicker (600 nm) layer of polysilicon, which will be separately etched in the next steps protecting the front surface with resist (e)(f). Protection of the back side during the aluminium sputtering is mainly mechanical. Sputtering is a process that involve one side of the wafer at the time, but wafers need to be leant on the reactor support to

be processed. Following figure 2.14, 1.5 μm of metal is sputtered in the backside (b) and resist is used to cover all the front surface and define the circular or squared windows in the back side of all the detectors or the optical test structures (c). The metallization process finishes with a metal etching (d) step and resist stripping (e). At this point, after a general cleaning of the wafer, a thermal treatment at 350°C is performed. As explained before, this step will act on the metal grains enlarging their size improving, in this way, the metal conductivity and reducing its reflectivity. For what concern the front surface, the metal alloy is deposited on silicon dioxide in order to decoupled the electronics connection from the diodes structures (strips) of the detector by means of the gate oxide. This solution permits to decouple direct current signals (like leakage current) from the pulses induced by the passage of particles or ionizing radiation. Connection with the implants (bias and guard rings or dc pads of the strips) are previously opened etching SiO_2 through the patterns defined by a lithography process. On the other hand, in the backplane an ohmic contact is created, depositing the aluminium directly on the silicon surface doped with phosphorus. In this case, silicon can dissolve into aluminium and aluminium can diffuse into silicon forming aluminium spikes through the n^+n junction. The final annealing at 350°C also forms Si-Al alloy at the silicon-aluminium interface, which helps to prevent aluminium-silicon interdiffusion and junction spiking.

Process monitoring

Thickness and uniformity of the metal structures on the front side of the detectors have been measured by means of a contact profilometer as well as the metal strip width. Metal on the backside is not of interest for the optical characterization, because the laser beam is supposed to pass through the circular window. Five different measurements, as for the thermal oxide, have been performed in different region within the surface of each wafer. Figure 2.15 shows the procedure followed for one of them. The region chosen in this case is the cut line between two sensors, in which all the layers grown (oxide) or deposited (polysilicon and metal) have been removed at each etching process in order to leave only bare silicon on the path prepared for the diamond saw that would be used to separate the individual chips on the wafers. Each device is surrounded by a metal ring deposited on the channel stopper defined with the first level of the mask.

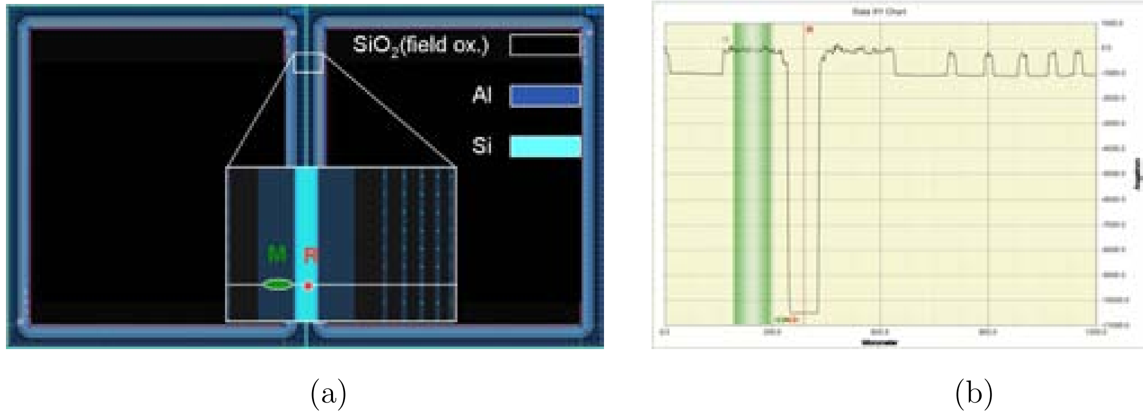

(a) (b)

Figure 2.15: *Details of a metal thickness measurement with the profilometer. (a) This particular case refer to the thickness of the metal ring deposited all around the detector edges. The wafer profile selected by the white line is shown (b). Distance between metal surface and the bare silicon substrate (marked with M and R respectively) gives the value of the metal thickness (see table 2.5.*

Extrapolating the profile of the wafer surface along a line (white in the figure) crossing the cutline, the thickness of the aluminium layer can be measured considering the distance of its surface (M) from the silicon substrate reference (R). Due to the metal roughness, the measurement is averaged on a region defined by the green marker.

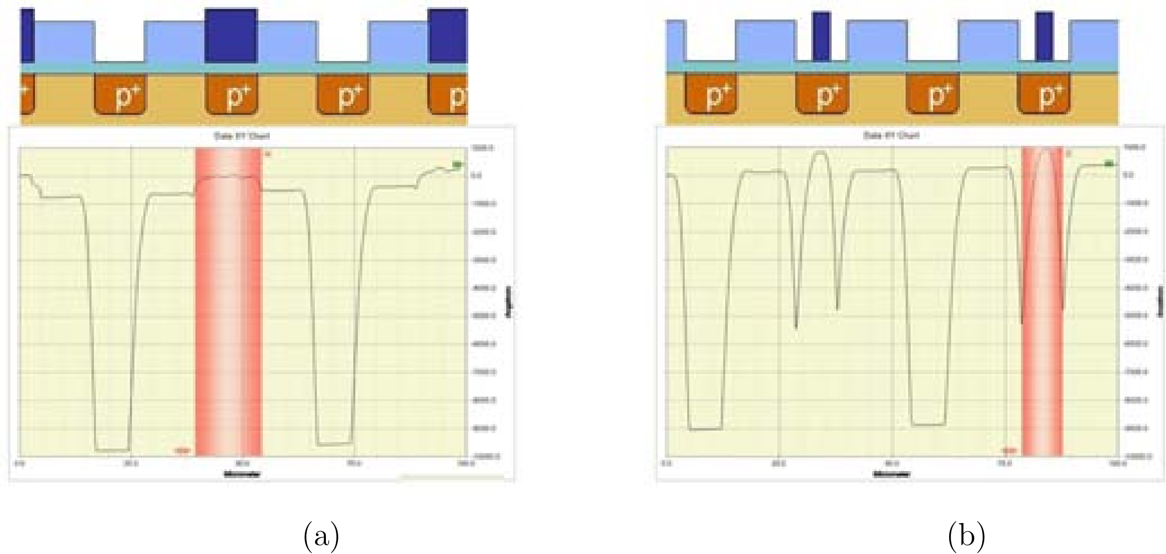

(a) (b)

Figure 2.16: *Surface profiles of two different detectors: sensor S1 with strip(metal) width = 15(15) μm (a) and sensor S5 with strip(metal) width = 15(5) μm (b). Schematics of the detectors surface composition are added to each image.*

Table 2.5: *Mean values of the metal thickness and its uniformity within the wafer surface. Expected value is 950 nm.*

Wafer	Thickness [nm]	Uniformity
1	940	5 %
2	995	6 %
3	929	5 %
4	972	5 %
5	965	6 %
6	961	5 %

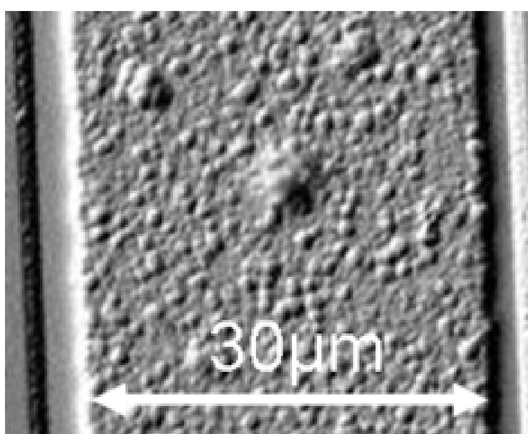

(a)

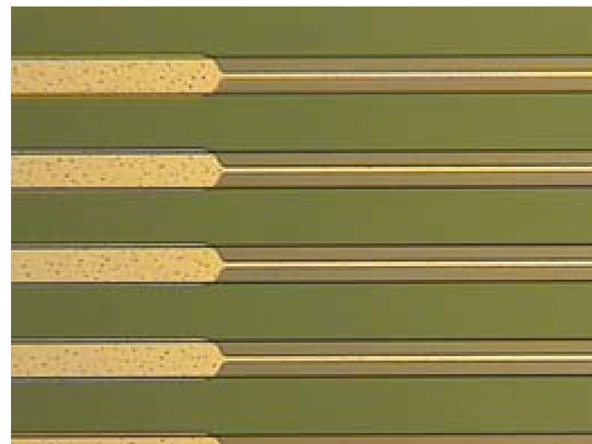

(b)

Figure 2.17: *Roughness of sputtered aluminium (a) and detail of sensor S9 with strip(metal) width = 15(3) μm at the end of the fabrication process (b).*

Main results and uniformity of the measurements are listed in table 2.5. In order to check the metal strip width, other measurements have been performed monitoring the orography of some detectors in the strips region. In figure 2.16 two examples are given. Only a qualitative analysis can be done because of instrumental limits in following the grooves profiles on the strips when the metal strips are narrowed. Other considerations on the real shape of structures on a detector will be presented in section 2.4.4, with the use of some pictures taken with a scanning electron microscope (SEM). Pictures of the detectors are shown in figures 2.17 (a) and (b). In particular a SEM image

of a 30 μm wide strip of Aluminium and its grains composition are shown. Value of 40 nm roughness has been measured and used in the detector model to better predict reflectivity of aluminium in the optical simulation: reflection, no absorption, result to be the main interaction of aluminium with IR light. The second picture, taken with an optical microscope, refers to a detail of sensor S9 in the region where the metal lines meet the electric pads on the strips.

2.4.3 Passivation: an anti-reflection coating

PECVD of SiO_2 and Si_3N_4

After the last metal layer definition, a passivation layer is normally deposited on the wafer to protect the chips from impurities, moisture or scratches. A good barrier layer deposited at low temperature ($< 450°C$) with high dielectric strength and high mechanical strength is demanded for a reliable passivation. Silicon nitride satisfy all of these requirements and is commonly used as the last passivation layer, deposited on a silicon oxide pad layer, as a buffer against strong tensile stress of nitride. Both

Table 2.6: *Properties of oxide and nitride.*

Oxide (SiO_2)	Nitride (Si_3N_4)
High dielectric strength, $> 1 \times 10^7$ V/cm	High dielectric strength, $> 1 \times 10^7$ V/cm
Lower dielectric constant, $k = 3.9$	Higher dielectric constant, $k = 7.0$
Not a good barrier for moisture and mobile ions	Good barrier for moisture and mobile ions
Refraction index ($\lambda = 633$ ns), n = 1.46	Refraction index ($\lambda = 633$ ns), n = 2.01

silicon oxide and silicon nitride are good electrical insulators with very high dielectric strength (breakdown voltage). Referring to table 2.6, where stoichiometric values are listed, silicon oxide has a lower dielectric constant than silicon nitride. Therefore, using oxide (thermal or deposited) in interconnection applications causes a smaller parasitic capacitance between the metal lines. On the other hand, silicon nitride provides more moisture and mobile-ion barrier than oxide, that leads definitely to the choice of silicon nitride as the last layer deposited on a chip. From an optical point of view, things are different. As explained in section 2.2, when the light impinges on the

interface between two homogeneous media with different refraction index, its energy is split between reflected and transmitted waves. The higher the difference between the refraction indices, the higher the portion of energy reflected. Considering that the refractive index of silicon is 3.88 at $\lambda = 633$ nm, then the layers order Si-Si_3N_4-SiO_2 would improve transmittance of light if used instead of the conventional Si-SiO_2-Si_3N_4. Nevertheless, remembering that the aim of this work is improving light transmittance without affecting detector operation and considering the above issues, the last sequence, Si-SiO_2-Si_3N_4, is the one used for these devices too. In section 2.6 we will see how, even in this configuration, a proper choice of the thickness of the last layers of silicon nitride (covering both the front and back surface), can improve transmittance of the laser light.

A silane-based Plasma Enhanced Chemical Vapor Deposition (PECVD) chamber can deposit both oxide and nitride with one process sequence, respecting the temperature limits imposed by the aluminium metallizations on the wafer.

CVD is a process in which gaseous chemical precursor(s) has (have) a chemical reaction on the wafer surface depositing a layer of solid by-product. This happens in a sequential process including several steps. The precursors introduced in the reactor diffuse across the boundary layer and impinge on the surface where they are absorbed by the substrate and start migrate on the surface till a chemical reaction takes place creating a solid material. The first few molecules of the solid material form nuclei on the surface, and further chemical reactions cause the nuclei to grow into islands that grow, merge and finally form a continuous thin film on the wafer surface. Since the steps in a CVD process are sequential, the one that occurs at the slowest rate will determine the deposition rate. Gas-phase processes dictate the rate at which gases impinge on the surface and are only weakly influenced by the deposition temperature. On the other hand, the surface reaction rate dependence on temperature can be expressed in this way:

$$R \; = \; A \, exp(-E_a \;\; kT) \tag{2.5}$$

where A is the frequency factor, E_a is the activation energy, k is the Boltzmann constant and T the absolute temperature. High deposition rate normally translates into high homogeneity of the layer deposited.

In PECVD, a radio frequency (RF) glow discharge can transfer energy into the

reactant gases, allowing reactions on the substrate surface at a lower temperature of the system. High deposition rate can be thus achieved as well as high quality of the layers. By reacting silane and oxygen or nitrous oxide in plasma or silane and ammonia or nitrogen in plasma at reduced temperature, silicon dioxide and silicon nitride films can be formed by the following reactions respectively:

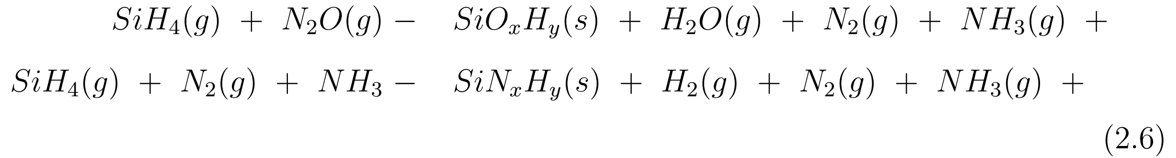

$$SiH_4(g) + N_2O(g) - \quad SiO_xH_y(s) + H_2O(g) + N_2(g) + NH_3(g) +$$
$$SiH_4(g) + N_2(g) + NH_3 - \quad SiN_xH_y(s) + H_2(g) + N_2(g) + NH_3(g) + \tag{2.6}$$

Silicon dioxide and silicon nitride obtained by means of a plasma-assisted deposition are not pure products, they always have a small amount of hydrogen in the deposited film and a no precise concentration of O or N that lead to a change in the characteristics of the materials depending on the relative concentration of each element. For instance, dielectric constant of both oxide and nitride results slightly higher than their stoichiometric value listed in table 2.6.

In silane PECVD processes the deposition rate is mainly determined by gas flow rate, especially silane flow rate. By increasing silane flow alone, the deposition rate is increased, but also the refractive index of the final layer. At the same time, higher flow of silane translates into a reduction of compressive stress of the film.

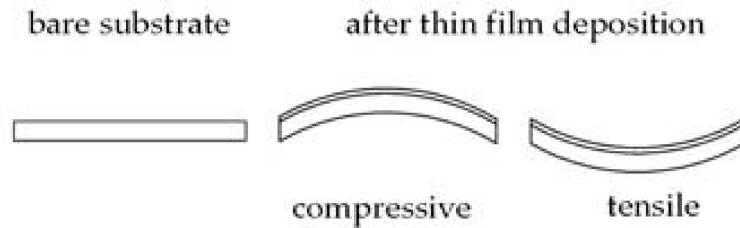

Figure 2.18: *Definition of compressive and tensile stress.*

Stress is an important issue to take into account when dielectric films are deposited on a wafer. It arises from the mismatch at the interface between different materials, such as the substrate and the film. There are two kinds of stress, intrinsic stress and extrinsic stress. The first develops during the film nucleation and growth, the second

results from differences in the coefficients of thermal expansion between the film and the substrate. It can be either tensile or compressive: figure 2.18 shows these effects. High stress on the dielectric film, whether it is tensile or compressive can cause film cracking, metal line spiking or void formation. For PECVD of dielectric thin film, intrinsic stress can be controlled by the RF power: working at high RF power, deposition rate is no longer influenced by this parameter and it can be used to control the film stress. On the other hand, extrinsic stress can be reduced depositing a layer characterized by compressive stress before another characterized by tensile stress, like in the case of silicon nitride deposition after depositing a buffer pad of silicon oxide. Evaluation of stress by means of bow measurements will be discussed in section 2.5.

Passivation processes monitoring

Table 2.7: *Mean values of the passivation silicon dioxide thickness and its uniformity within the wafers surface. Expected values are 1006 nm and 1020 nm for the front and back side respectively.*

Wafer	front side		back side	
	Thickness [nm]	Uniformity	Thickness [nm]	Uniformity
1	949	3 %	1000	2 %
2	980	3 %	1006	2 %
3	986	3 %	1001	1.6 %
4	978	3 %	1005	2 %
5	955	4 %	971	4 %

After definition of metal patterns on the wafer and their annealing, 1006 (1020) nm of silicon dioxide were deposited in the front (back) side of the wafers and the fabrication run was paused just before the deposition of the last layers of Si_3N_4. In addition to thickness measurements, this hold had the purpose of allow crosschecking the simulation model by comparison with measurements of the almost completed devices, and extrapolating real optical properties of the actual deposited materials using the control optical test structures. A new optimization of the detector transmittance was performed re-tuning the thickness of the last silicon nitride layers, taking into account

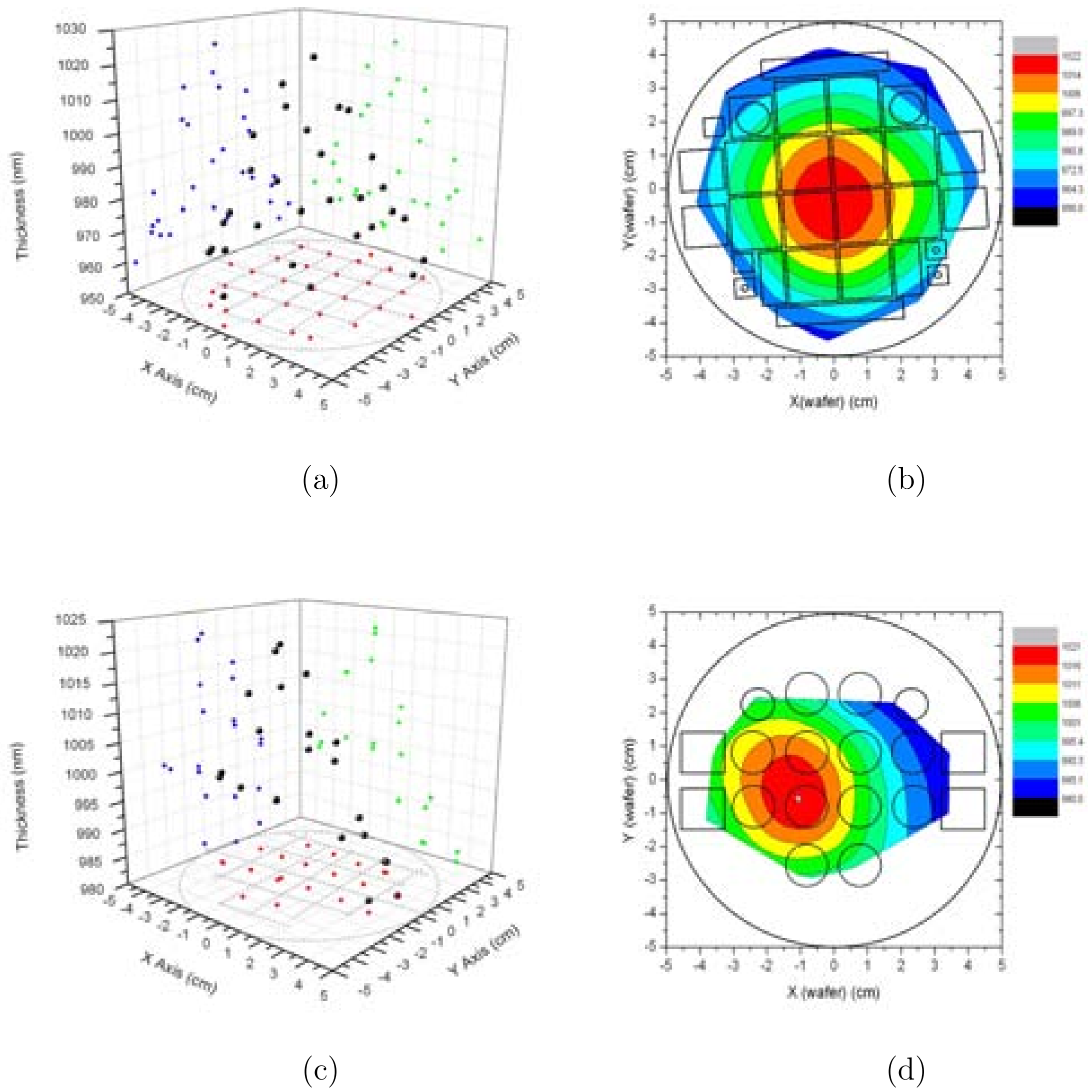

Figure 2.19: *Thickness values of silicon oxide (black balls) on the front side and on the back side of wafer 2 (a),(c) respectively. Distribution of the measurements within the wafer surfaces is highlight by the projections on the XY plane (red marks). Extrapolation of the thickness map on both sides is shown in figure (b) and (d).*

the thickness (measured) of the other materials. Optical results will be discussed in section 2.6. Thickness and uniformity of silicon oxide have been measured with the same spectroscopic reflectometer introduced in section 2.4.1 in the clean room laboratory after PECVD process [55]. For each wafer instead of the normal 5 measurements, a set of 30 (20) measurements in different points within the front (back) surface of the detectors and test structures have been performed, in order to better mapping the uni-

formity of the layers thickness. Results are summarized in table 2.7. Figure 2.19 shows a more detailed treatment of the data concerning the front side (top figures) and back side (figures in the bottom) of wafer 2. In figures 2.19(a), (c) the values obtained from all the measurements (black dots, Z axis) are presented in relation to their position on the wafer surface (projection on the XY plane). Figures 2.19(b) and (d) display the thickness contour map on both sides of the wafer. In both cases, the fluctuation in the layer thickness is not random. Thickness decrease continuously with a radial pattern from the higher value zone. Although, the thickness value within the measurements set reveal a uniformity better than 5 %. After the optical characterization carried out

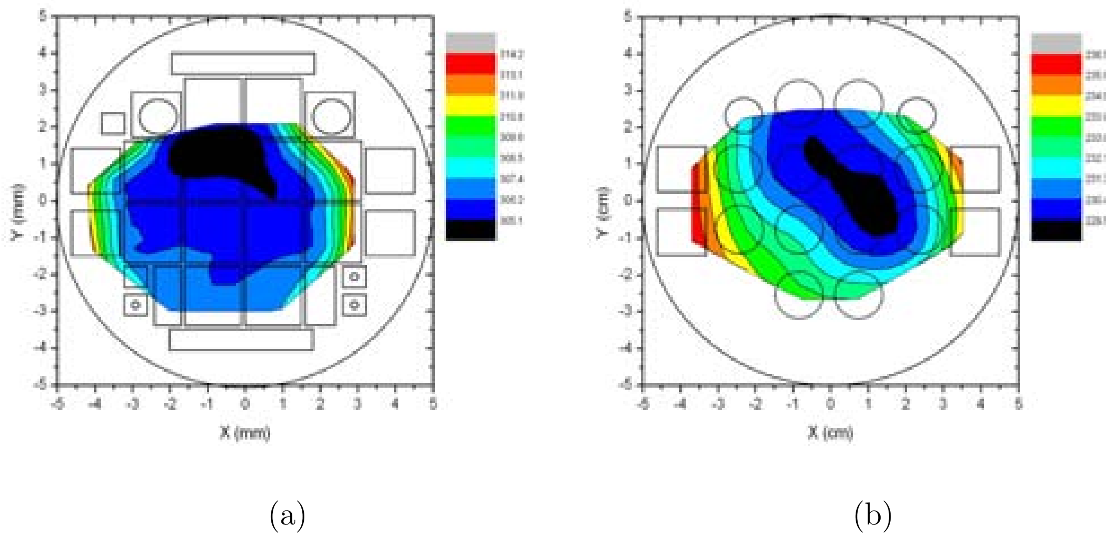

(a) (b)

Figure 2.20: *Thickness map of silicon nitride on the front side and on the back side of wafer 3 (a),(b) respectively.*

at this stage of the run fabrication, new values of the Si_3N_4 final layers have been chosen to be deposited on wafers 3-5, while the old values have been used for wafers 1 and 2. The new values were 310 (240) nm for the front (back) surface. They were measured using the same instrument as for SiO_2 thickness measurements. Figure 2.20 shows the contour map of thicknesses measured in wafer 3. The results obtained for all the wafers are listed in table 2.8. In this case too, high uniformity of the layers thicknesses has been achieved, demonstrating that the fabrication process carried out at the IMB-CNM clean room facilities is faithfully reproducible from an optical point of view.

Table 2.8: *Mean values of the passivation silicon nitride thickness and its uniformity within the wafer surfaces. Expected values are (1046±50) nm and (1005±50) nm for wafer 1 and 2 in the front and back side respectively, (310±16) nm and (240±12) nm for wafer 3,4 and 5 in the front and back side respectively.*

Wafer	front side		back side	
	Thickness [nm]	Uniformity	Thickness [nm]	Uniformity
1	1075	2 %	1013	1.5 %
2	1052	2 %	1025	1.9 %
3	308	1.5 %	232	1.5 %
4	304	2 %	234	1.6 %
5	306	2 %	234	1.5 %

The last processes performed are photolitography steps to define the openings for the bonding pads in the front side, and to open the ohmic contact around the passivated window in the back side, obtaining the final cross section shown in figure 2.21.

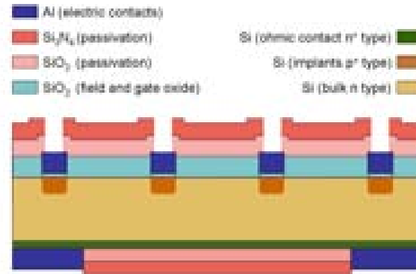

Figure 2.21: *Schematic cross section of a sensor in the contacts pad region.*

2.4.4 Etch and deposition profile

The previous sections described the most important materials of optical interest and the related processes used to fabricate the transparent detectors with emphasis on growth or deposition of the different material layers. Photolithography has been introduced as the patterning process used to transfer the design pattern from the mask to the wafer, followed by either etch or implantation through the pattern defined on

the photoresist. Figures 2.12, 2.13, 2.14 and 2.21 show a schematic cross-section of a detector during the processes flow. Is possible to appreciate strips formation with their metallization and final passivation. Images are not to scale and do not account for the real etch or deposition profiles, assuming in both cases a resultant perfect vertical profile. In this section etch and deposition profiles will be considered allowing a better understanding of the real device structure.

There are two kinds of etch processes: wet etch and dry etch. Wet etch uses chemical solution to dissolve the materials on the wafer surfaces (both at a time) not covered by the photoresist. By-products of the wet etch chemical reaction are gases, liquids, or solids that are soluble in the etchant solution. Normally this process has very good selectivity and high etch rate, wich is mainly controlled by the etchant temperature or concentration. *Selectivity* is defined as the etch ratio between two different materials: the one that needs to be etch and the other we do not want to remove. For instance, hydrofluoric acid (HF) etches silicon dioxide very fast, but it hardly etch silicon at all if is used alone. Therefore, HF is normally used to etch silicon dioxide layers grown on a silicon wafer at the beginning of the process run to prepare the silicon surface for the fabrication flow as well as in the strip grooves definition before gate oxide growth. The chemical reaction of the oxide wet etch is given by:

$$SiO_2 \ + \ 6HF \ - \quad H_2SiF_6 \ + \ 2H_2O \tag{2.7}$$

H_2SiF_6 is soluble in water, therefore the HF solution can etch away the silicon dioxide. Aluminium can be etch by a wide variety of acidic formulations. In general a component (for instance, HNO_3) oxidizes the aluminium and another (e.g. H_3PO_4) dissolves the resultant Al_2O_3 simultaneously.

In any case, wet etch is characterized by an isotropic etch profile that can be partially controlled by temperature. The perfect vertical profile shown in figures 2.12, 2.13, 2.14 and 2.21 is the favoured one, since it can transfer the patterns from the photoresist to the underneath film without any critical dimension loss. A more realistic profile after wet etch is depicted in figure 2.22 (a). Thus, the schematic (f) in figure 2.14 representing the detector after the metallization process can be more realistically represented like in figure 2.22 (b). Even if it has no influence on the optical characteristics of the detectors, doping profile has been represented in a more realistic way. Actually, as explained in section 2.4.1, after ion implantation wafers are subject to

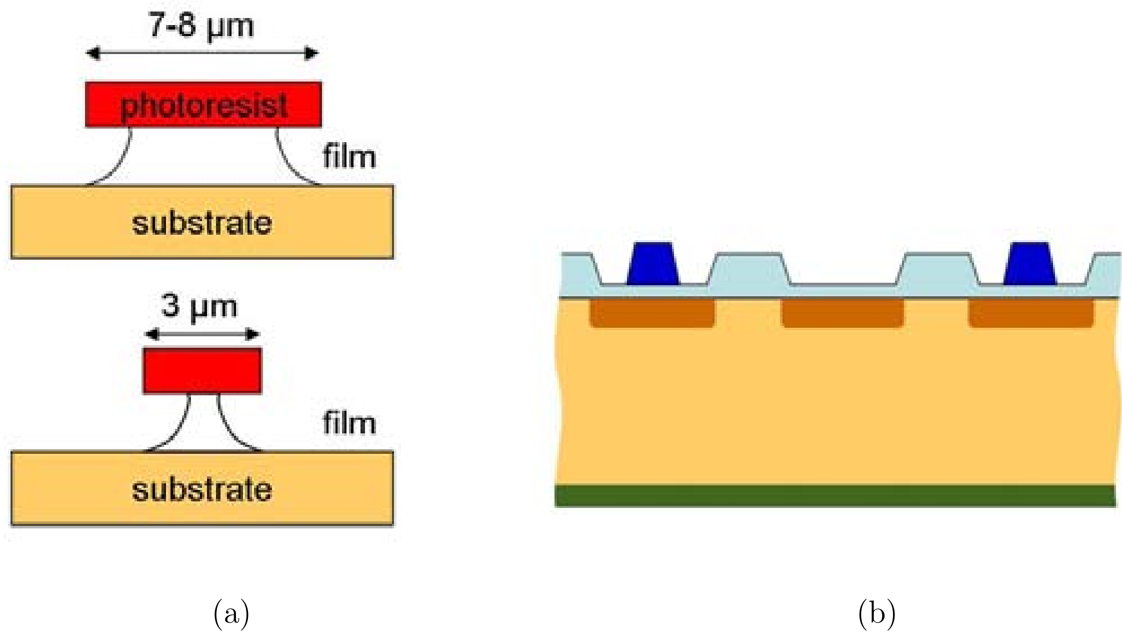

(a) (b)

Figure 2.22: *Wet etch isotropic profile (a) and detector schematic after metallization taking into account wet etch effects as well as doping real profiles. (b). Drawn not to scale.*

a reheat treatment at 950°C to diffuse and activate dopants into the substrate. Lateral diffusion is normally around 80% of the junction depth.

After defining metal patterns on the wafer, passivation layers are deposited on the surface by means of plasma enhanced chemical vapour deposition. A characteristic of this process is the so called *step coverage* that defines the deposition profile. Step coverage is a measurement of deposited film reproducing the slope of a step on the substrate surface. It is determined by both the arriving angle and the precursors surface mobility. The arriving angle on the upper corners of the step is larger than the arriving angle on the bottom step corners. Therefore the upper corners will have more precursor atoms or molecules when they diffuse across the boundary layer. If the precursors have low surface mobility, they react immediately after being absorbed on the wafer surface, instead of migrating on it to reach the regions with a smaller arriving angle. In this case, overhangs result on the upper corners that can cause undesirable voids between adjacent structures. As discussed before, in PECVD processes high surface mobility is achieved even at low temperature. The deposited film step coverage also increase the arriving angle on the substrate surface, defining a tapered angle profile during the previous etch processes. Considering that the schematic in figure 2.22 (b)

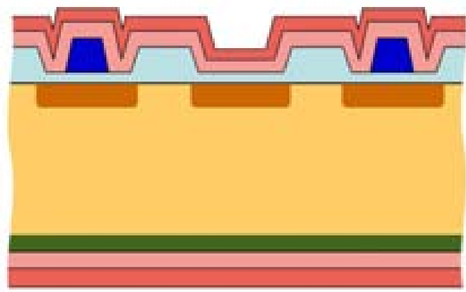

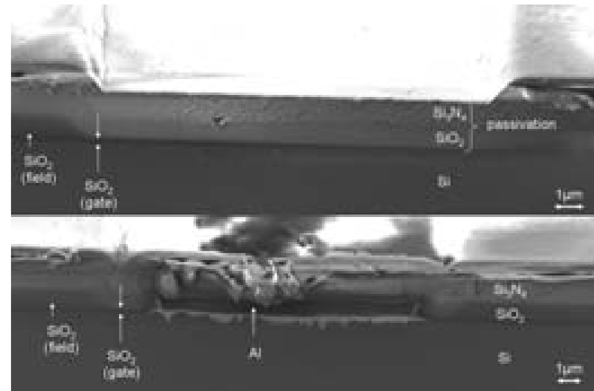

(a) (b)

Figure 2.23: *(a) Schematic of the final detector with realistic profiles. (b) SEM pictures of a cross-section of detector S1 characterized by strip (metal) width of 15 (10) μm. The upper picture refer to the region with the intermediate strip without metal coating: thermal oxide as well as the passivation layers are indicated. The bottom picture refer to a strip with metrallization.*

represents the substrate for the silicon dioxide and silicon nitride PECVD, the final result can be easily expected to be like the schematic in figure 2.23 (a). The SEM pictures on the right (figure 2.23 (b)) confirms the expectation.

The real profile angles have been measured and taken into account in the simulation model of the detector, even if their influence on light transmittance is negligible, due to the little area interested.

2.4.5 Deposition of polycrystalline silicon

In these AC coupled microstrip detectors, strips implants are connected to a bias ring, and biased through it, by means of resistors made of doped polycrystalline silicon. Since the selected region for the passage of the laser beam across the sensor is in the middle of the active area, the study of the optical properties of the device does not consider polysilicon resistors. Nevertheless they are important for the correct operation of the detector. Polysilicon has been deposited by a Low Pressure Chemical Vapour Deposition (LPCVD) at a pressure of 0.2 to 1 Torr and at 630°C using the silane reaction:

$$SiH_4 - \quad Si + 2H_2 \tag{2.8}$$

At high temperatures, silane dissociates and silicon can be deposited on the heated surface. The process is mainly controlled by process teperature, total process pressure, silane partial pressure for the diluted process and dopant concentration. In particular the resistivity of the polysilicon film highly depend on deposition temperature, dopant concentration and annealing temperature. In the same way as for aluminium sputtering, high temperature during LPCVD form larger grain size on the surface, that means lower resistivity of the film, but also possible difficulties in the etch process because of rough sidewall. Thus, polysilicon is deposited at a lower temperature to achieve smaller grain size and then, after etch and photoresist strip, it is annealed at higher temperature (950°C) to form larger grain size and lower resistivity. In the process flow for these detectors fabrication, 600 nm of polysilicon is deposited after the ion implantation processes used to create the strips and a general cleaning treatment. A Boron implantation process is then used to define the resistivity of polysilicon together with a final thermal treatment.

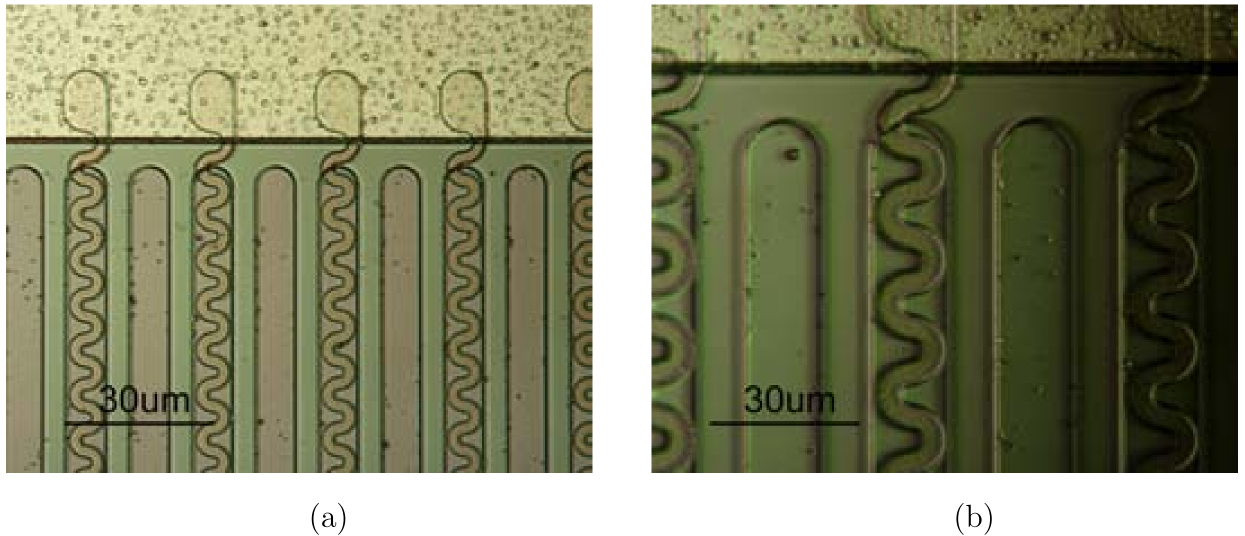

(a) (b)

Figure 2.24: *(a) Resistances of a transparent detector (optical microscope image). (b) Detail of a resistance.*

Finally, the geometry of the resistors has been chosen to reach the desired value of their resistance, 1 MΩ <R<1.5 MΩ. As mentioned in section 2.3, their layout has been adapted to the orography of silicon dioxide on which polysilicon is deposited, keeping limited their total length as much as possible and respecting photolithography minimum feature size of 2.5 μm. Figure 2.24 (a) shows a picture of the real resistances

that can be compared to the mask design presented in figure 2.9 (b). Resistances pattern has been transferred to the polysilicon layer by means of a dry etch process using Cl_2 as the main etchant. In plasma, Cl_2 molecules dissociate to generate free chlorine radicals, which are very reactive and can react with silicon and form gaseous silicon tetrachloride. Chloride tends to combine with photoresist materials and deposit a thin polymer layer on the side wall. This helps to achieve an anisotropic etch profile obtaining the result shown by the SEM image, figure 2.24 (b).

O_2 is used to improve selectivity over oxide. The electrical characterization of the devices demonstrate that the value obtained for the bias resistance R=(1.35±0.13) MΩ is in perfect agreement with the expected value.

Pictures of the front and back sides of a wafer at the end of the fabrication process are shown in figure 2.25.

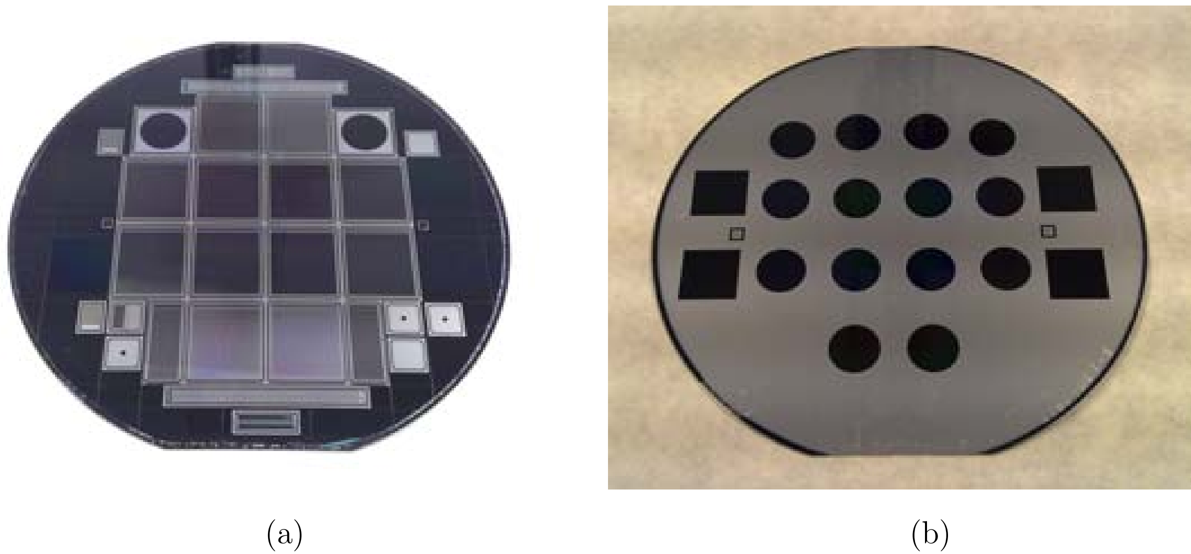

(a) (b)

Figure 2.25: *(a) Front side of a wafer at the end of the processes run. (b) Back side of the same wafer at the end of the processes run.*

2.5 Electrical characterization

The detectors have been electrically characterized in the IMB-CNM laboratories with the use of a Cascade Microtech probe station with thermal chuck, two Keithley 2410 Source/Meters and an Agilent 4284A LCR Meter (see figure 2.26). For the C-V

characteristic measurements a decoupling box designed and produced at CERN [21] has been used in order to decouple the sinusoidal signal of the LCR Meter from the high bias voltage applied by the Source/Meters. All the measurements have been carried out

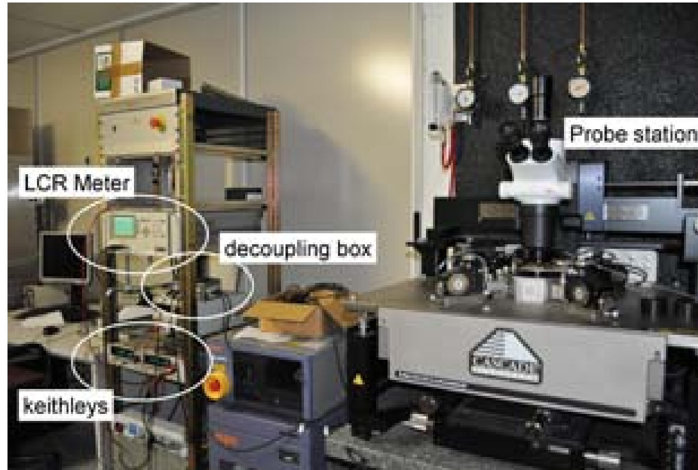

Figure 2.26: *Set up used for the electrical characterization of the detectors.*

at 20°C, following the RD50 recommendations [56]. For the I-V and C-V characteristics measurements the bias ring and the first guard ring have been both biased, while for the interstrip capacitance measurements only the bias ring has been biased by probe needle; the other three probes have been used to apply the alternate voltage between one strip and its first neighbour strip at both sides. Results show that the range thicknesses used for the material layers does not affect electrical behaviour of the detectors. In figure 2.27 the I-V and $1/C^2$-V characteristic (see section 1.1.3) of all the sensors of wafer 2 are shown. The depletion voltage of all the detectors is between 35 V (detector S2 with implant width = metal width = 15 μm and with intermediate strips) and 53 V (detector S9 with implant width = 15 μm, metal width = 5 μm and without intermediate strips). The breakdown voltage is higher than 200 V and the leakage current in general is less than 100 nA for an active area of 1.2×1.5 cm^2 for all the detectors. Differences in the layout of the structures translate into differences in the interstrip and coupling capacitance values. The interstrip capacitance is proportional to sw/p, where sw and p are the strips width and pitch respectively. The detectors are characterized by a readout pitch of 50 μm, but the six in the upper half of each wafer have an intermediate floating implant between each two strips (implants pitch = 25 μm). Then, the width of the aluminium and the p^+-implant is different from sensor to sensor, defining six

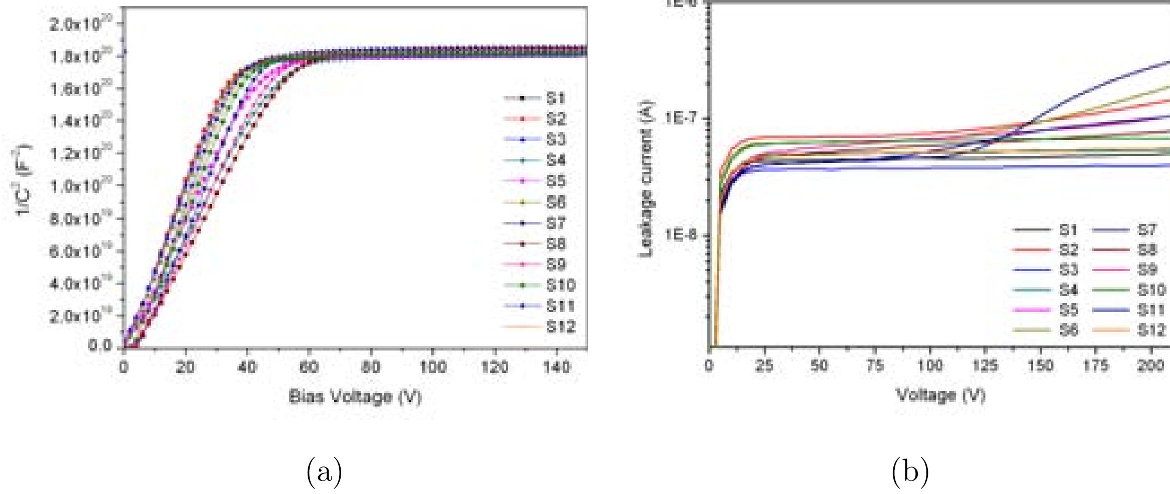

(a) (b)

Figure 2.27: *(a) $1/C^2$-V characteristic of the sensors of wafer 2. (b) I-V characteristic of the sensors of wafer 2.*

combinations. Figure 2.28 shows the results of the measurements and their dependence on the layout parameters. Wider strips translate into higher interstrip and coupling capacitance. The values related to the detectors with intermediate strips are lower than the ones of the detectors without intermediate strips, but with the same strip/metal design. For the detectors with strip width equal to 15 μm the decrease is around 15%, while it is less than 10% (more than 20%), for the sensors with strip width equal to 17.5 μm (12.5 μm).

For what concern the coupling capacitance, as expected it is smaller for the detector with narrower electrodes: in this case the metal width has the higher influence on the measure. An error in the design of the contact pads of sensor S9 forbidded measuring its coupling capacitance.

Finally, measurements of the wafer bow have been performed with a PROFORMA 300 by MTI, a manual, non-contact wafer metrology inspection system, in order to monitor the effect of the passivation layers thickness on the total stress. It is measured at the centre point of the wafer with a three point reference plane about the edge of the wafer. Results are listed in table 2.9. Bare wafers before processing had a bow varying in the range ± 10 μm.

The sign minus denotes that the tensile stress of silicon nitride layer on the front

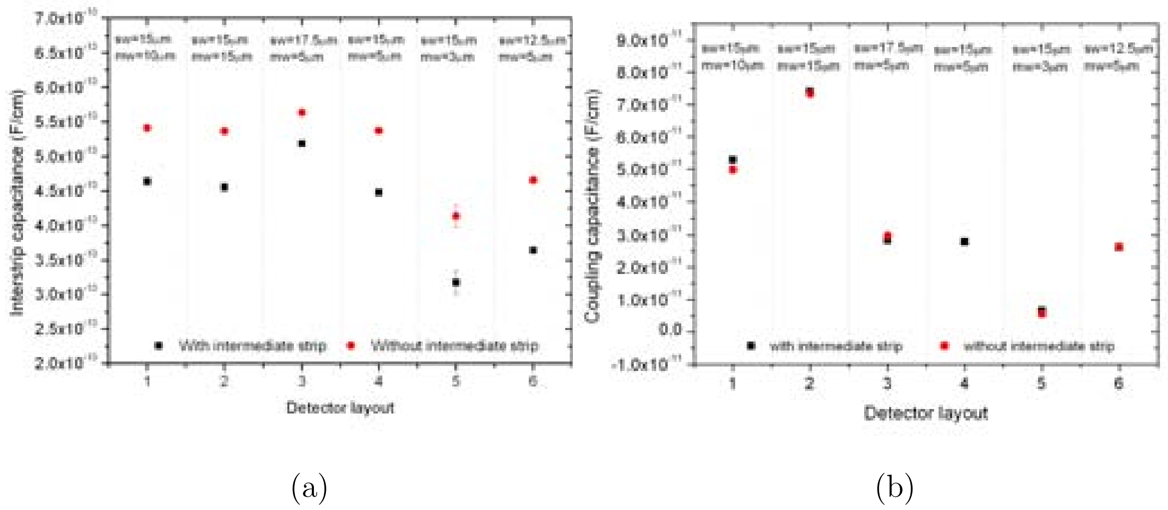

(a) (b)

Figure 2.28: *Interstrip capacitance (a) and coupling capacitance (b) as a function of detectors parameters (values for V_{bias} = 100 V).*

Table 2.9: *Values of the wafers bow after processing.*

Wafer	1	2	3	4	5
bow [μm]	-190±2	-195±2	-202±2	-181±2	-202±2

side of the wafer is dominant in all the wafers, being thicker than the layer deposited on the back side (see table 2.8).

2.6 Optical characterization

The devices have been optically characterized into the clean room at different stages of their fabrication at the same time the materials thickness has been measured. Transmittance, reflectance and absorption of IR light have been measured with the same spectrophotometer used for the first validation of the optical model of the detector for the simulations. It is a custom system from Control Development with 1.2 nm spectral resolution over the range 955-1155 nm [57]. A picture of the instrument is shown in figure 2.29, under a configuration of Transmittance measurement. Details of its working principle can be found in reference [49]. As mentioned in section 2.4.3, the

Figure 2.29: *Spectrophotometer under a configuration of Transmittance measurement.*

fabrication process was paused after the silicon dioxide deposition, in order to measure the SiO_2 layers thickness, crosscheck the simulation tool, especially with the use of the optical test structures, and re-tune the thickness of the last silicon nitride layers to maximize light transmittance of the final detectors, using the measured thickness of all the other layers and their extrapolated refraction indexes. The four optical test structures included in each wafer have been designed with the purpose of reaching the result shown in figure 2.30 (a). Each one, at the end of the fabrication run, have a different combination of material layers grown or deposited on both sides of the silicon substrate. So, using the measured thickness of all the materials layers, measured transmittance (%T) and reflectance (%R) of these homogeneous structures have been compared with the ones obtained by the simulation. Figure 2.30(b) shows the results in the wavelength range of interest, together with the schematics of the structures at the moment of holding the process before the Si_3N_4 deposition (and SiO_2 etch). The continuous (dotted) blu line represented the measured (simulated) %T value, while the continuous (dotted) red line represented the measured (simulated) %R. The good agreement reached between the results permitted to extrapolate the optical parameters values for adjusting the detector model and re-tune the Si_3N_4 layer thickness to improve the ARC on the detectors. At the same time, the real layers thicknesses (plus the ones predicted for the nitride layer) and the real profile of the detector surface discussed in section 2.4.4, have been considered to obtain a more realistic dependence

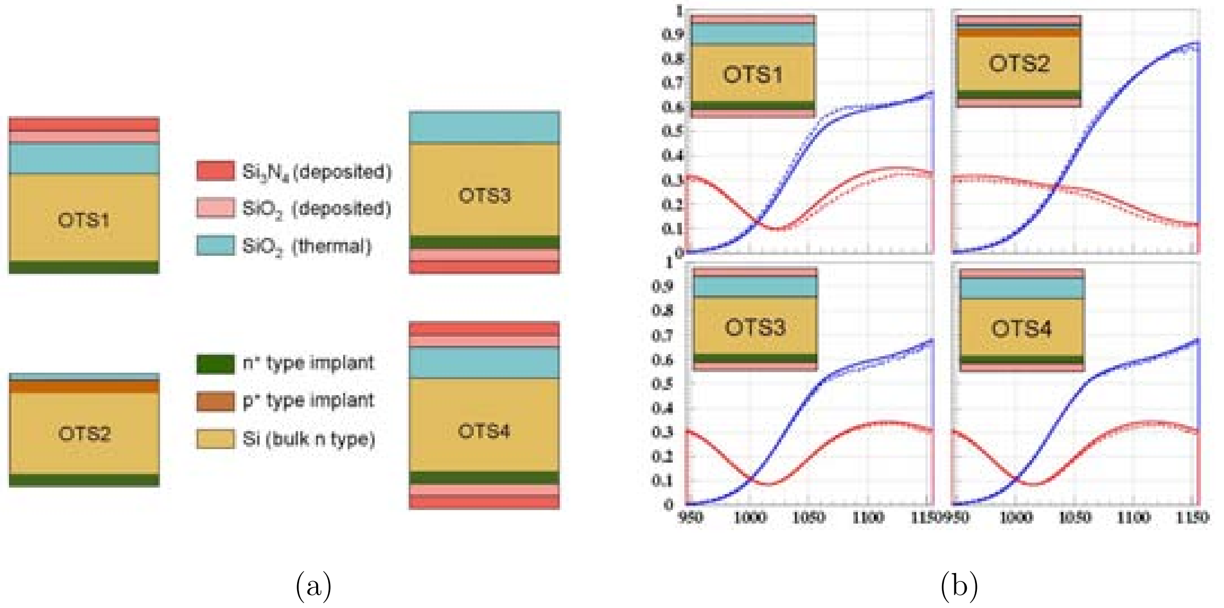

(a) (b)

Figure 2.30: *Optical test structures at the end of the fabrication process (a). Comparison between measured (continuous line) and simulated (dotted line) %T (blu lines) and %R (red lines) for the four optical test structures before the last nitride layer deposition and oxide etch (b).*

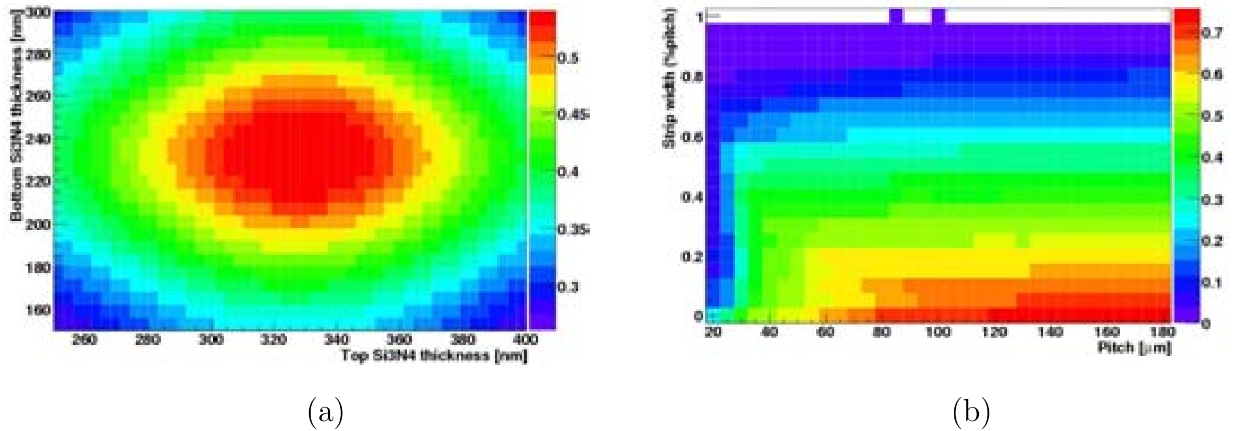

(a) (b)

Figure 2.31: *(a) Transmittance (%T) coded in colors as a function of the top and bottom Si_3O_4 layer thickness, for the particular case of detector S9 with implant (metal) width 15(3) μm and λ = 1085 nm. (b) Transmittance as a function of the strips pitch (horizontal axis) and of the metal strip width (express as a percentage of the pitch value in the ordinate axis) for λ = 1085 nm.*

of transmittance from the metal width/pitch ratio. Results of the new simulations are presented in figure 2.31. On the left, simulations refers to sensor S9 characterized by strip (metal) width 15(3) μm. The final values for the silicon nitride layers (see section 2.4.3) have been chosen within the plot region of maximum transmittance. On the

right, the dependence from the strips pitch in the horizontal axis (first order effect), and from the metal width (second order effect) is shown. For our baseline of 50 μm pitch a maximum of 50% of the transmittance can be reached for a metal width of about 5 μm. Higher transmittance can be reached only for higher values of the strip pitch. After silicon nitride deposition on wafers 3-5, new measurements have been per-

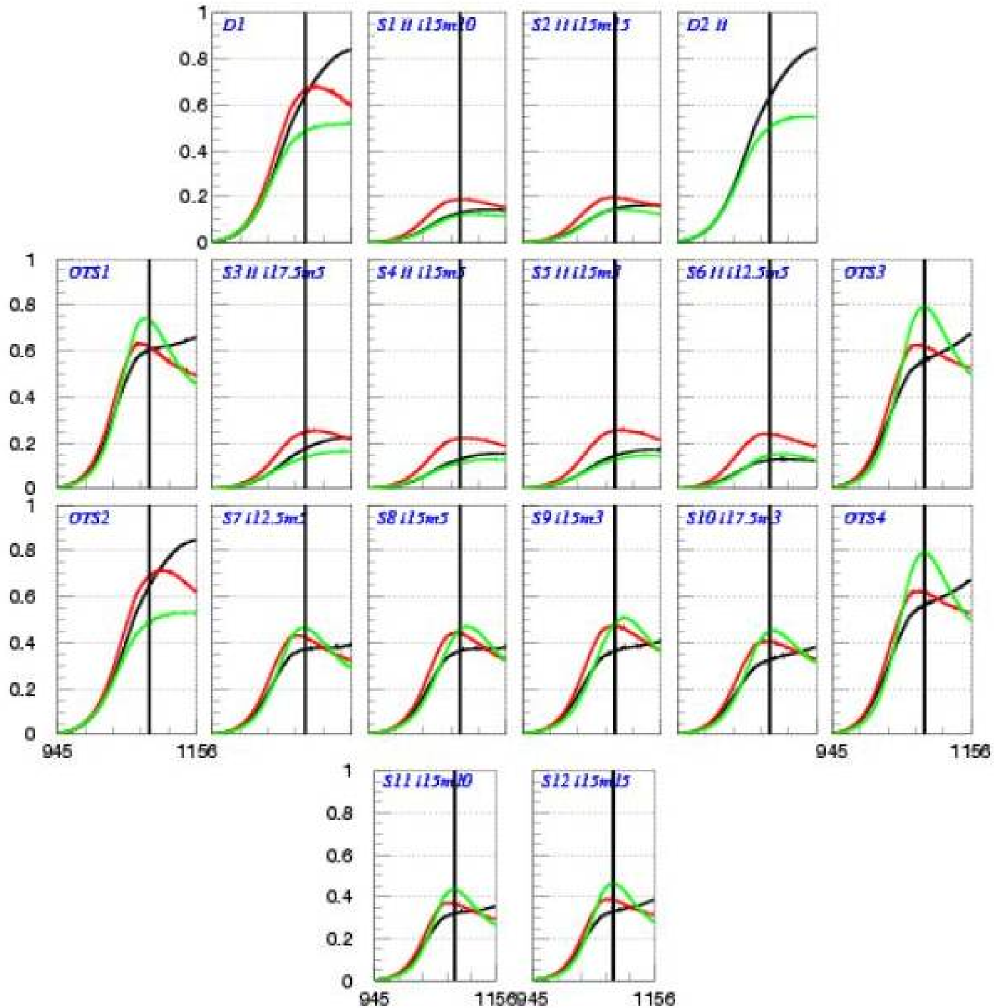

Figure 2.32: *Measured transmittance for a wafer with no nitride passivation (black line) compared to the same wafer with (top=0,bottom=230) nm nitride thickness (red color) and (top=310,bottom=230) nm (green). The horizontal axis shows the wavelength in nm.*

formed. In order to appreciate the effect of the ARC on the structures, Si_3N_4 has been firstly deposited on the back side of the detectors (230 nm) and finally on the front side (310 nm) after an intermediate measurement of the transmittance. Figure 2.32 shows the resultant %T as a function of the wavelength (horizontal axis) for all the detectors,

reference diodes and optical test structures of wafer 3 after three different depositon steps. Transmittance measured before nitride passivation is depicted in black, after nitride deposition in the back side of the wafer in red and at the end of the run in green. In general, after the first deposition in the back side transmittance shows an increase of 5% for $\lambda = 1085$ nm and reach its maximum (50% for sensor S9) at the end of the process, confirming the simulation expectation. The considerably lower transmittance for the 6 sensors in the upper half of the wafer is due to the higher diffraction angle of the transmitted beam, that removes light away from the incident direction. As explained in section 2.3, these detectors have one intermediate strip without metal coating between each two strips. The orography of the detector surface affect light transmission (increasing the diffraction angle), even without the metal reflection effect. For what concern the unpatterned optical test structures, OTS4, that has nitride coating in both sides, reach a maximum transmittance of 80% (less than 60% without nitride passivation). All the four optical test structures of wafer 2, along with sensors

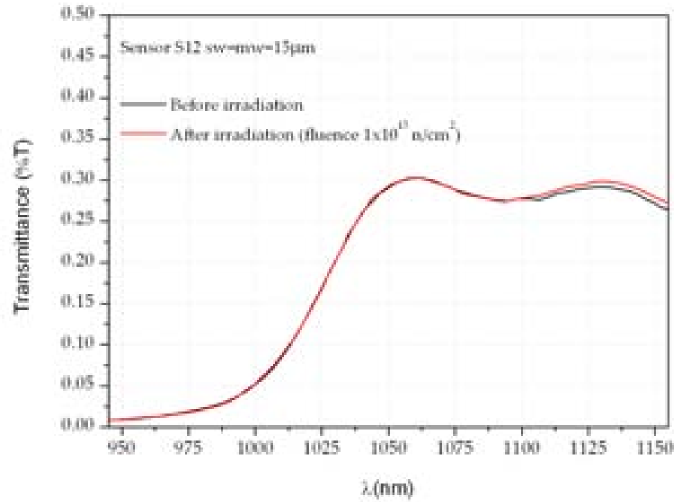

Figure 2.33: *Measured transmittance before and after irradiation of sensor S12 of wafer 2.*

11 and 12 of the same wafer, have been irradiated at the Neutron Irradiation Facility of the Jozef Stefan Institute in Ljubljana [58] with 1 MeV neutrons at a fluence of 1×10^{15} n/cm^2. Transmittance measurements have been performed after the irradiation, obtain the same results previous to the irradiation for every structure. Figure 2.33 shows the result for sensor S12.

2.7 Summary and discussion

The aim of the work presented in this chapter was the development of new microstrip detectors for the laser alignment systems of future particle trackers. It basically consisted in the improvement of transmittance of the sensors to the IR light, changing the values of key layout and technological parameters, but still using a standard fabrication process.

An optical model of the sensor has been developed by the IFCA group of experimental physics in Santander, and validated with the use of many test wafers produced in the IMB-CNM clean room laboratories. The passage of a coherent beam of light through the active volume of the detector has been simulated identifying the minimum changes needed in the design and technology to maximize the transmittance. The transmittance of a microstrip detector results to depend at the first degree on the periodicity of the strips. The lower the pitch, the higher the diffraction angle and the lower transmittance collected along the incoming propagation direction. With a baseline pitch of 50 μm, a metal-strip-width/pitch ratio $\leq$10%, together with a careful choise of the thickness of the material layers, gave the highest transmittance value (%T=50%).

The layout for the first prototype detectors has been designed respecting simulation hints. Mask design includes twelve baby sensors equipped with 256 readout strips with a pitch of 50 μm. A circular window (1 cm diameter) has been opened in the aluminium backplane to allow the laser beam to pass through and the width of the aluminium electrode and strip implant was varied from sensor to sensor within the wafer to study the dependence of transmittance and electrical behaviours on these layout parameters. Half of the detectors has also one intermediate implant within two readout strips, in order to increase their spatial resolution. Many optical and electrical test structures have been added to the mask.

The detectors have been fabricated using the standard flow of processes developed by the IMB-CNM radiation detectors group for the fabrication of silicon microstrip detectors and setting the processes parameters in order to obtain the material layers thickness advised by the simulation. The real thickness and uniformity of each material have been measured after each oxidation or deposition process: in general the values obtained are in agreement with the ones expected and their uniformity within the wafer

surface is better than 5%, value required to ensure reproducibility of devices with the same optical characteristics.

The electrical characterization of the samples demonstrates that the optimization of the passivation layers does not affect their electrical behaviour, showing the expected dependence of their characteristics on the layout parameters.

The detectors have been optically characterized with the use of a spectrophotometer in the wavelength of interest at different stage of their fabrication. Measurement results highlight the importance of the last passivation layer (silicon nitride) as an anti-reflection coating (ARC), especially for what concern the passivation of the back electrode window. Optical test structures with unpatterned surfaces reach a maximum transmittance of 80%, while the detectors with strip (metal) width 15(3) μm reach the expected value of 50% at the end of the run, validating the simulation model of the detector as a powerfull and correct tool. Detectors with intermediate strips without metal coating show a considerably lower transmittance, revealing the strict influence on light diffraction of the orography of the sensor surface. A further characterization of some samples and test structures demonstrates that the transmittance value does not change after irradiation with 1 MeV neutrons at a fluence of 1×10^{15} n/cm^2.

A transmittance value of 50% means that 5 consecutive modules can be aligned with the same laser beam. Obtaining this result with a pitch of 50μm is a very good improvement with respect to previous versions of transparent detectors. For instance, CMS obtained transmittance of 20% for a pitch of 189μm. The comparison with AMS is less direct, since the detectors are double sided, with crossed strips. For reference, the maximum transmittance achieved there was 50% with a 110 μm readout pitch in one of the sides. Considering the simulation predictions, validated by the experimental results, doubling the strip pitch in the sensors developed in this work, a transmittance value close to 70% can be achieved, that translates into increasing the number of modules that can be aligned of a factor 2.

Beam tests of some samples are in program for future characterizations in order to test the detectors efficiency and radiation hardness, especially for what concern the prototypes with extremely slim metal strips.

Chapter 3

New 2D position sensitive detectors

In the last 30 years, semiconductor sensors have been object of great interest as position-sensitive detectors. Many devices have been developed in order to obtain two coordinates of an ionizing event using double-sided processing (double-sided microstrip detectors and drift detectors) or implementing a complex readout system with a large number of electronic channels (pixel detectors). In this chapter a different approach is proposed to provide a simple single-sided detector 2D position sensitive and with a limited number of readout channel [59]. Integrating in a common microstrip single-sided detector resistive coupling electrodes and a double read out system for each strip, it is possible to obtain 2 coordinates of an ionizing event, making use of the resistive charge division method and just doubling the number of readout channels.

The resistive charge division method has been frequently used in gaseous detectors with resistive anodes [60][61][62][63] and studied for silicon pad detectors [64], but it has never been implemented in actual semiconductor microstrip detectors. Radeka, in his seminar paper [65], formulated for the first time the basic characteristics of the charge-division concept for resistive electrodes. One of the main conclusions of this study is the fact that the position resolution -assuming a readout electronics with optimal shaping time- is determined only by the electrode capacitance and not by the electrode resistance.

Recently, the use of the charge-division method in very long microstrip sensors, several tens of centimetres, has been proposed as a possible tracking technology for the International Linear Collider detector concepts. Along this application line, the behaviour of a detector equivalent RC network implemented in a PC board was used

for the benchmarking of a SPICE electronic circuit simulation [66]. The PC board was populated with discrete components with electrical specifications matching the main electrical parameters of such long microstrip detector DC coupled to the readout electronics. The simulation, supported by the RC network measurements, confirmed the overall validity of Radeka s formulation on resistive charge-division.

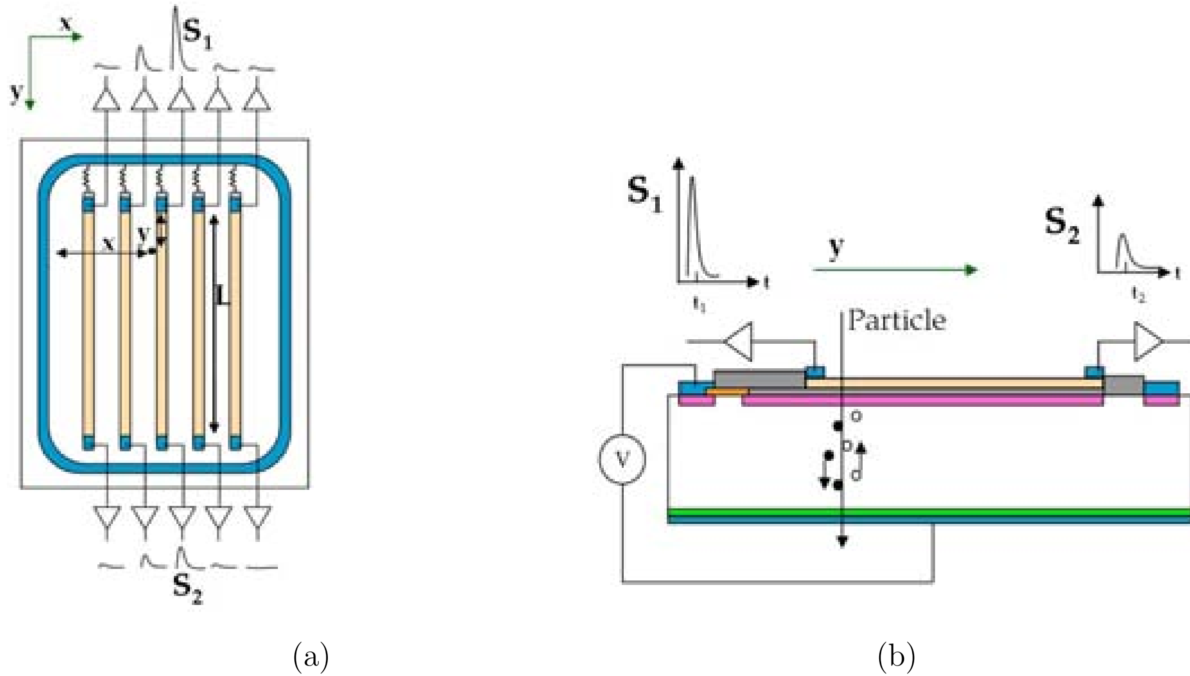

Figure 3.1: *(a) Schematic top view of the novel detector and (b) lateral cross-section of the central strip (not to scale). It is possible to distinguish the aluminium elements in blue and the resistive electrodes on the strips (light yellow regions). The aluminium pads are connected each one to a channel of the read-out electronics (two for each strip). When an ionizing particle crosses the detector, different signals (S_1 and S_2) are read by the opposite electronic channels. The X coordinate of the event can be reconstructed using the center of gravity method, whereas the Y coordinate is reconstructed comparing the signal amplitudes at the ends of strips.*

In this chapter, a novel microstrip detector concept is introduced, where the resistive electrodes (light yellow structure in figure 3.1 (a) and (b)) are made of a thin layer of highly doped polycrystalline silicon. This original approach decouples the resistive electrodes from the detector diode structure (determining the charge collection) through a coupling capacitance (gray layer in figure 3.1 (b)). In this way, it is easy to manufacture AC coupled p^+-on-n or n^+-on-p detectors, more convenient for the case of high radiation environments. The field of application of this device expands beyond the

nuclear or particle physics tracking applications, reaching other possible areas as laser-based position sensitive devices, heavy ion and other highly-ionizing particle detector, Compton cameras, medical imaging, etc.

In the next sections, the feasibility of the resistive charge division concept in a full-fledged microstrip detector is demonstrated. Then, the first results on the reconstruction of the hit position along the strip direction using the proof-of-concept prototypes is presented. The experimental method used to this purpose was the study of the output signals under a longitudinal scan of a strip, carried out with an infrared laser beam.

3.1 Principle of operation: resistive charge division in microstrip detectors

As seen in chapter 2, in a conventional microstrip detector the metal contacts of the strips extend over almost all the length of the implants and are connected each one to a read-out channel. When an ionizing particle crosses the detector, the propagation of the induced signal along the coupling electrode does not suffer significant attenuation, i.e., the signal amplitude does not depend on the particle impinging point along the electrode direction. When using, instead of metal alloy, a resistive coupling electrode equipped with metal contacts at its ends, the signal undergoes significant attenuation during its propagation towards the electronics contacts. The longer the propagation length, the larger the signal attenuation. In this way, a conventionally manufactured single-sided microstrip sensor can provide the two-dimensional coordinates of the particle impinging point; the transverse coordinate derived from the usual electrode segmentation [15] and the longitudinal coordinate determined by relating signals amplitude at both ends of the electrode.

The resistive electrode represents a diffusive RC line, in which a current pulse undergoes not only an amplitude attenuation but also an increase of the rise time the further it travels. Using readout electronics characterized by a short -compared to the RC constant of the line- shaping time, this translates into a non constant signal ballistic deficit (see section 1.3.3). The ballistic deficit can be reduced increasing the shaper peaking time; however, a longer peaking time increases the parallel readout

noise contribution (section 1.3.2). In reference [65], Radeka derived the optimal peaking time for a resistive charge division configuration, under the assumption of high electrode resistance compared to the amplifier impedance and long amplifier peaking time compared to input signal rise times.

Under these assumptions, dependence between the longitudinal coordinate of the particle position and the fractional signal amplitude read from one side of the strip is expected to be linear. The actual functional form (following figure 3.1 notation with A_1 and A_2 the amplitudes of S_1 and S_2 respectively) is given by equation 3.1:

$$y = L \times \frac{A_2}{A_1 + A_2} \tag{3.1}$$

3.2 Proof-of-concept prototypes

3.2.1 Specifications and fabrication

The resistive charge-division proof-of-concept prototypes presented here are AC coupled microstrip detectors with the upper electrodes of the coupling capacitor made of polycrystalline silicon. Two prototypes with different electrode resistivity were fabricated at the IMB-CNM clean room facilities in Barcelona, using the standard technology for single-sided p^+-on-n, AC coupled, silicon microstrip detectors (see mask levels sequence in section 2.3). A standard reference sensor and several electrical test structures [51] were included in each wafer of the fabrication run that allowed a more direct measurement of the electrical parameters of the new sensors.

Each detector consists of 384 p^+ strips (20 μm wide) with a pitch of 80 μm on a (285±15) μm thick n-type substrate. The resistive electrodes (30 μm wide) have a total length of 2 cm with linear resistance $R\ l$=2.8 Ω μm for one of the devices and $R\ l$=12.2 Ω μm for the other. The linear resistances have been defined during the processes flow dedicated to the bias resistors formation. As introduced in section 2.4.5, after the ion implantation processes used to create the strips and a general cleaning treatment, 600 nm of polysilicon is deposited by means of a LPCVD process. To better understand the electrodes formation, a lateral cross section of the detector (like in figure 3.1 (b)) is depicted in figures 3.2 and 3.3, under the processes flow of interest. After polysilicon deposition (b) a Boron implantation process (c) is used to define its

resistivity. Then a first photolithography process (d) is used to transfer the patterns to

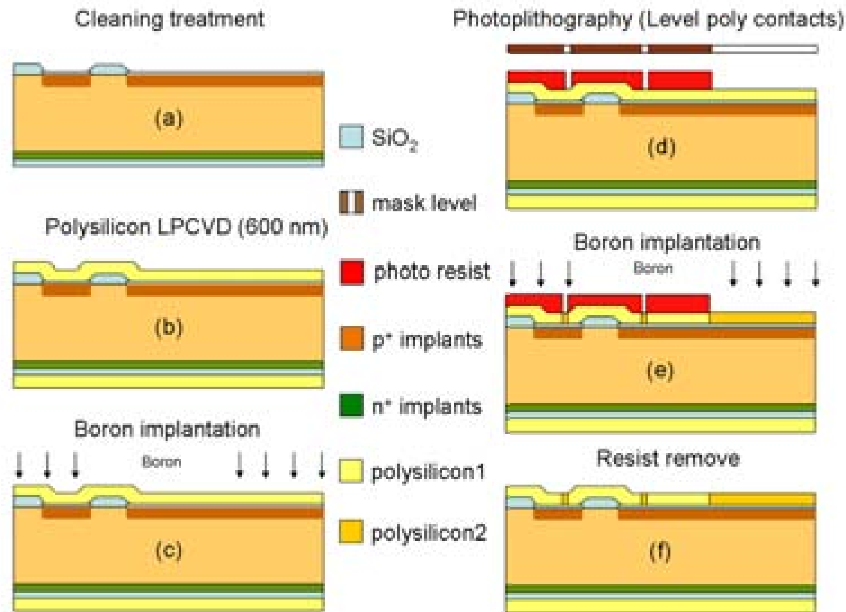

Figure 3.2: *First steps for the polysilicon electrodes (and bias resistors) definition. The schematics refers to a detail of a lateral cross section of the detector as in figure 3.1 (b). Drawing not in scale.*

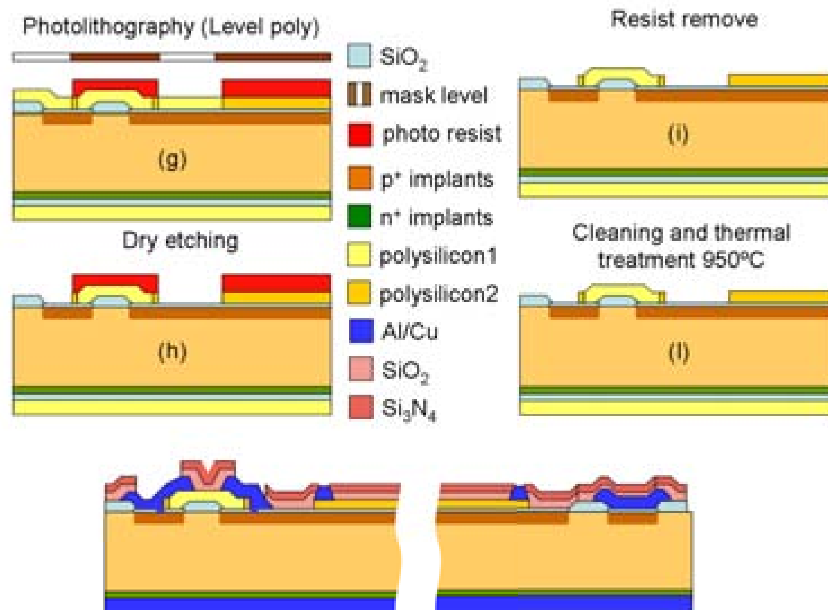

Figure 3.3: *Final steps for the polysilicon electrodes (and bias resistors) definition and final result of the processing.*

the photoresist for a selective ion (Boron) implantation (e) at both ends of the resistors, in order to further reduce the resistivity of polysilicon in the connections between the resistors edges and the metal contacts and, at the same time, to select the R/□ of the electrodes. As the final dopant concentration is controlled by the doses and energy of the ions as well as by the duration of the process, the two different R/□ values have been obtained changing these parameters from wafer to wafer. A second photolithography process (g) then defines the resistors and the electrodes shape. A final cleaning and thermal treatment at 950°C (l) is necessary for the dopants diffusion, crystals size enlargement and the preparation of the wafer for the next processes involving contact formation and passivation of the device. The final result can be seen in the bottom of figure 3.3. In particular it is possible to appreciate the metallization of the bias ring (with the pad for the wire bonding to the bias circuit), the DC pad of the strip (via opened through the oxide layer) useful for the electrical characterization of the sensor and the metal pads at the two ends of the polysilicon electrode for the connection with the readout electronics.

3.2.2 Modelling and simulation of the detector

A SPICE-like model of each prototype and the readout electronics have been developed in order to clarify the possible effect of the non-optimal shaping time on the linearity of equation 3.1, studying the response of the detector to a simulated current pulse injected at different points along the strip length.

Starting from the work presented in reference [69] the model of our detector has been built with standard components from the AnalogLib library of Virtuoso Spectre by Cadence [70]. A portion of the detector including five consecutive strips is modelled by a periodic structure composed of 80 cells, each one corresponding to a transverse section (250 μm long) of the strips. The unit cell is a complex chain of capacitances and resistors representing the main electrical characteristics of the device as the substrate resistance and capacitance (R_{sub} and C_{sub}), the interstrip resistance and capacitance (R_{int} and C_{int}), the p$^+$implant resistance (R_{impl}), the coupling capacitance (C_{AC}) and the resistance of the resistive upper electrode (R_{el}). Figure 3.4 shows the schematic of the unit cell. The values of the circuital elements have been determined from the ones measured during the electrical characterization of the detectors in full depletion

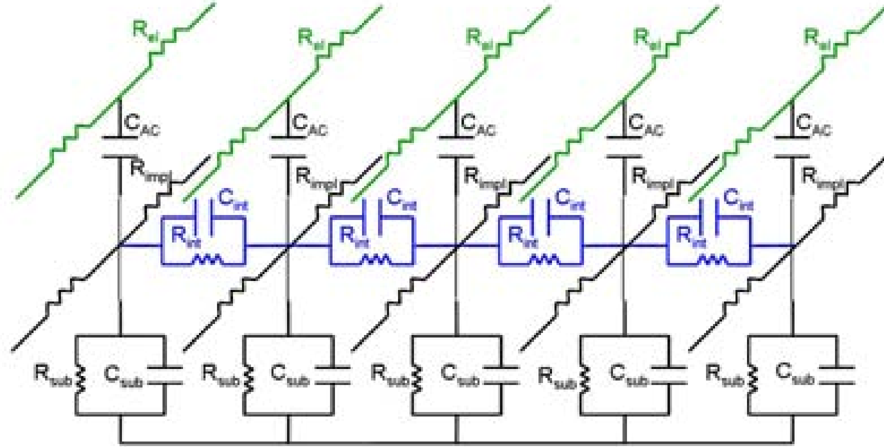

Figure 3.4: *Schematic of one of the 80 cells used to model the detector. Each one represents a portion (250 μm long) of five consecutive strips including the main electrical parameters like the coupling capacitance (C_{AC}), the substrate resistance and capacitance (R_{sub} and C_{sub}), the p^+ implant resistance (R_{impl}) and the resistance of the resistive electrode (R_{el}). In the simulation a current pulse has been induced at different nodes along the central strip implant.*

(V_{bias}=40V) and the test structures. These values are listed in table 3.1.

The detectors have been electrically characterized in the IMB-CNM laboratories with the use of the same instrumentation presented in section 2.5. The results are consistent with the ones of the standard microstrip detectors. The measured values are listed in table 3.2.

For this study, no dedicated analog signal processing electronics was built, but fast readout electronics designed for high energy experiments has been used. Therefore the front-end filtering of the signal was not optimized according to Radeka s conclusions. As it will be explained in more detail in the following section, we have used the ALIBAVA DAQ system [67] developed within the framework of the CERN RD50 collaboration. The analog front-end of the ALIBAVA system is based on the Beetle chip [68] used for the microstrip sensor readout of the silicon tracking subsystem of the LHCb experiment at LHC; consequently, the analog front-end shaper peaking time is set at 25 ns.

The model of the read-out electronics connected to the ends of each strip consists of a generic charge sensitive preamplifier followed by a CR-RC filter, whose peaking

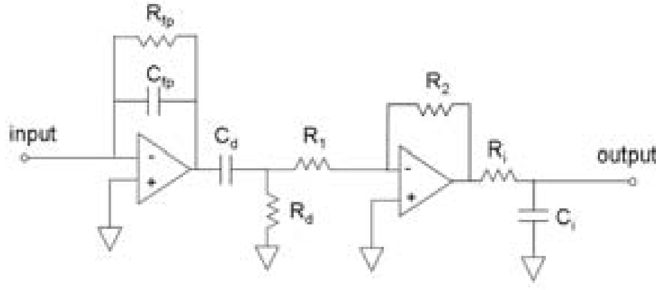

Figure 3.5: *Schematics of the front-end electronics modelled for the simulation.*

Table 3.1: *Values of the model parameters used for the simulation*

Detector		Readout electronics	
R_{el}	350 Ω or 1525 Ω	R_{fp}	300 MΩ
R_{impl}	718 Ω	C_{fp}	1pF
C_{AC}	4.7 pF	$C_d = C_i$	25pF
C_{sub}	8.6 fF	$R_d = R_i$	1 $k\Omega$
R_{sub}	20000 $G\Omega$	R_1	1 $k\Omega$
R_{int}	15 $G\Omega$	R_2	1 $k\Omega$
C_{int}	11.5 fF	R_t	1 $M\Omega$

time matches that of the Beetle chip. The front-end schematics is shown in figure 3.5 and the parameter values are listed in table 3.1.

The shape of the injected current is shown in figure 3.6. It is characterized by a rise time of 2 ns and total integrated charge around 4 fC. The rise time of the diode laser used for this study is 2 ns (measured with a high bandwidth photodiode), similar to the simulated one. The signal generator was connected to different points along the implant of the central strip with a step of 2 mm and the shapes of the current pulses, propagated to the entrance of the opposite charge-sensitive preamplifiers, have been recorded as well as the output response of the shapers. The current pulse read at the entrance of the preamplifier connected to the first cell of the strip (corresponding to the position 0 mm) is shown in figure 3.7 for each injection point and for both prototypes. As expected, the simulation confirms that the further the pulse travels the more its

Table 3.2: *Measured values of the polycrystalline silicon electrode resistance (R_{el}), depletion voltage (V_{dep}), breakdown voltage (V_{bd}), bias resistance (R_{bias}), interstrip resistance (R_{int}), interstrip capacitance (C_{int}) and coupling capacitance (C_{AC}).*

electrode resistance	V_{dep} [V]	V_{bd} [V]	R_{bias} [MΩ]	R_{int}	C_{int} [pF/cm]	C_{AC} [pF/cm]
2.8 Ω/μm	20	>300	4	>GΩ	0.46	189
12.2 Ω/μm	20	>400	2.41	>GΩ	0.46	189

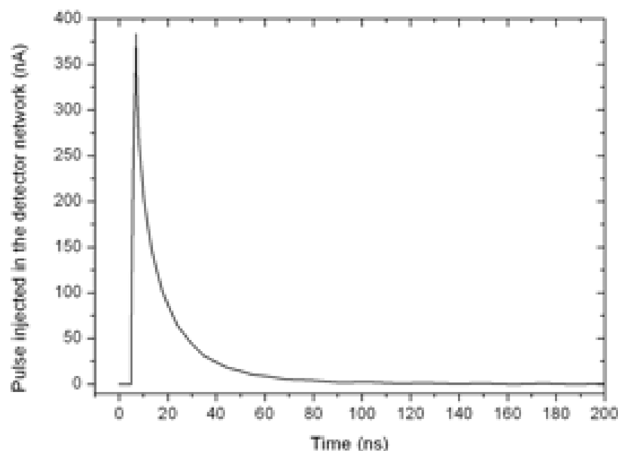

Figure 3.6: *Simulated input signal.*

amplitude decreases and its rise time increases: stronger effects can be observed for higher values of the electrode resistance.

The dependence of the response linearity on the electrode resistance is clearly seen in figure 3.8. According to equation 3.1, being A_1 and A_2 the amplitudes of the signal read at the output of the front-end electronics connected to the first and the last cells of the central strip respectively, the derived fractional position (A_2 $(A_1 + A_2)$) versus the injection point (y L) of current signal is shown in figure 3.8(a). The data related to the more resistive prototype reveal a clear separation (larger residuals spread in figure 3.8(b)) from the ideal values (green line in figure 3.8(a)) due to the ballistic deficit whose effect increases with the distance covered by the signal from the point of generation. It is worth to note also that in the case of the low resistivity prototype,

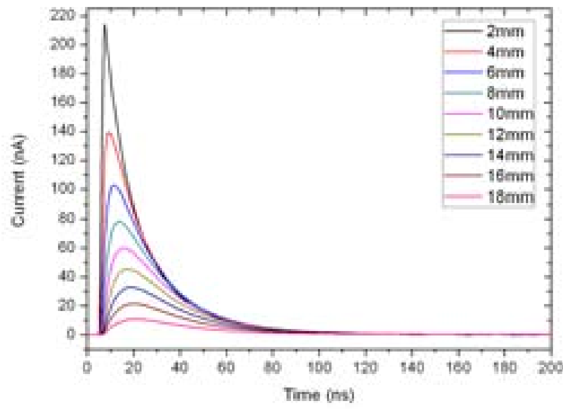

(a)

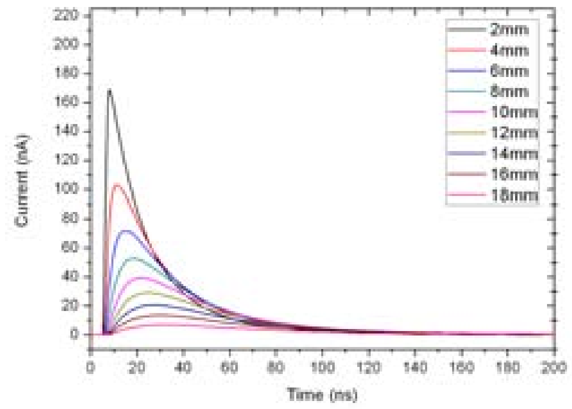

(b)

Figure 3.7: *Attenuation of the signal read at the entrance of the amplifier connected to the strip end in the corresponding position 0 mm. The results are shown for different positions of the pulse generator along the strip for R l=2.8 Ω μm (a) and R l=12.2 Ω μm (b).*

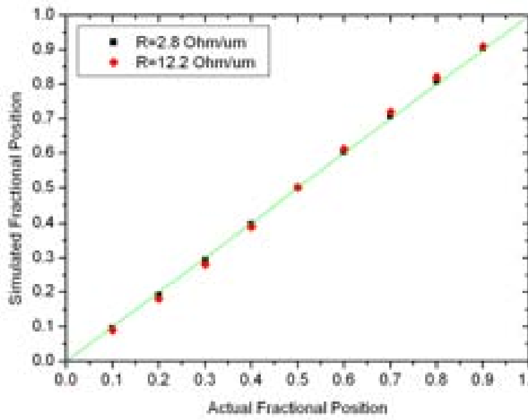

(a)

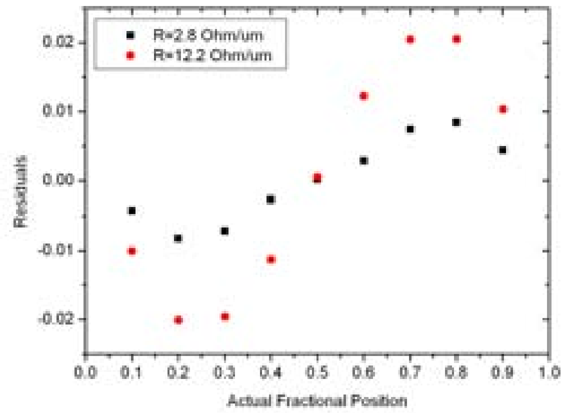

(b)

Figure 3.8: *(a) Simulated fractional position against the actual one for both values of the electrode linear resistance: R l=2.8 Ω μm and R l=12.2 Ω μm. The values have been compared to the linear prediction (green line). (b) The residual plot shows that for a peaking time of the analog front-end electronics equal to 25 ns, the linearity of the response of the detector suffers higher degradation for higher values of the electrode resistance.*

even for the more attenuated pulse, the rise time is around 10 ns, still only a 40% of the Beetle peaking time. Therefore the effect of the ballistic deficit in this sensor is

highly suppressed.

3.3 Laser characterization

3.3.1 Experimental setup

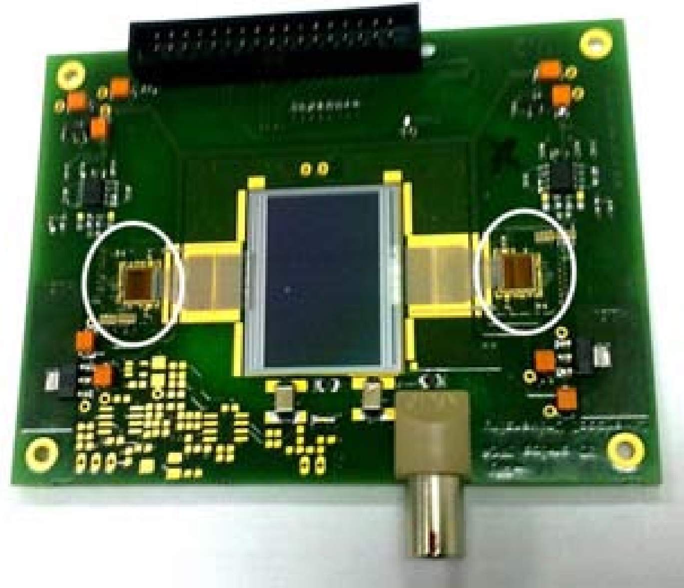

Figure 3.9: *Picture of one of the detectors mounted in the PCB sensor carrier. The two Beetle chips are indicated by the white circles. Each one is connected to one side of 128 consecutive strips of the detector in order to provide double-sided readout.*

Each sensor was mounted in a dedicated PCB sensor carrier and read out using an ALIBAVA DAQ system (see figure 3.9). The ALIBAVA is a DAQ system for the readout of microstrip sensors based on the Beetle analog readout ASIC. The Beetle integrates 128 pipelined channels with low-noise charge-sensitive preamplifiers and shapers with a peaking time of 25 ns. Each detector board has two Beetle chips, each one bonded to one side of 128 strips of the sensor like in figure 3.9.

The characterization test-stand allows for the precise injection of laser pulses along the microstrip direction (see figure 3.10). We used a pulsed distributed-feedback diode laser driven in a constant optical power mode and thermally stabilized. The laser output is coupled to a monomode optical fibre which feeds an inline fibre optic splitter: the first splitter output fibre is connected to a large bandwidth (2 Ghz) reference

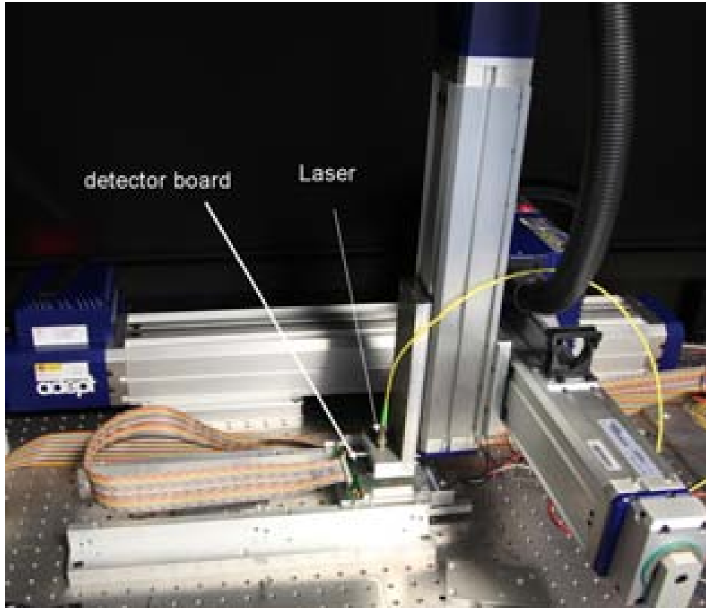

Figure 3.10: *Experimental setup. The micro focusing optical head mounted on the 3D axes stage is placed a few millimetres upon the detector board.*

photodiode whose output signal is recorded in a digital scope to monitor the laser pulse trace; the second splitter output fibre feeds a microfocusing optical head illuminating the sensor. The microfocusing optical head was moved by a 3D axes stage with a displacement accuracy better than 10 μm for all the axes. The laser is focused in such a way that the beam waist is at the sensor front plane; the beam intensity profile at the beam waist is a Gaussian with a sigma of 5 μm. The laser wavelength is centred at 1060 nm and the laser rise time, as measured by the reference photodiode, is 2 ns.

Comparing the signal amplitudes obtained with the laser pulses and the signal amplitudes obtained using a ^{90}Sr beta source, we estimated that the charge ionized by the laser pulse used during the sensor characterization is roughly equivalent to six times the most probable charge ionized by a minimum ionizing particle (MIP). The pulse optical power was adjusted using inline optical fibre attenuators and by tweaking the working parameters of the laser driver.

3.3.2 Longitudinal scan results

For each detector, a longitudinal scan was performed moving the focused beam spot along the midline of a polysilicon electrode -contrary to aluminium, polycrystalline

silicon is transparent to IR light. The pulse shape at the output of the front-end electronics shaper stage has been reconstructed scanning the whole electrode length (20 mm) with a scanning step of 2 mm.

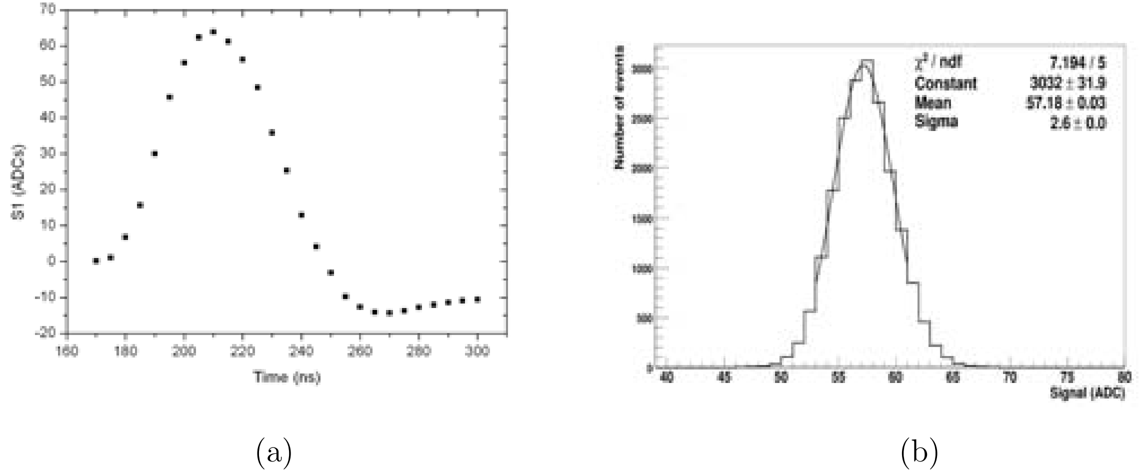

(a) (b)

Figure 3.11: *(a) Reconstruction of the pulse shape of the signal S_1 when the laser is 6 mm far from the contact pad along the scanned strip. The electrode linear resistance is $R\ l$=2.8 $\Omega\ \mu m$. For each time delay 20000 events have been recorded and the mean value of the signal has been extrapolated by fitting a Gaussian function to the data. As an example of this procedure the particular case of time delay = 200 ns is shown on the right (b).*

The ALIBAVA DAQ system does not allow to record the whole shape of the analog signal. On the other hand it allows to reconstruct it thanks to a particular feature that permits to change the value of the delay between the trigger time (synchronous with the laser pulse) and the acquisition time (specifying the instant at which the shaper output is sampled) [67]. Setting different delays in steps of 5 ns from 170 to 300 ns (see figure 3.11 (a)), we recorded 20000 events for each time delay and we found the amplitude of their distributions by fitting a Gaussian function (figure 3.11 (b)) obtaining a strong suppression of the statistical error. The amplitudes of the reconstructed pulses have been accurately extrapolated by fitting a Gaussian function to the peak region. These values have been used for the calculation of the fractional position defined by equation 3.1. The analysis of the data recorded, the histograms of the signals read by each channel of the two Beetles, have been created modifying the source code of the ROOT [71] macros provided by ALIBAVA [72].

Figure 3.12 shows, for both sensors, the measured fractional position of the laser

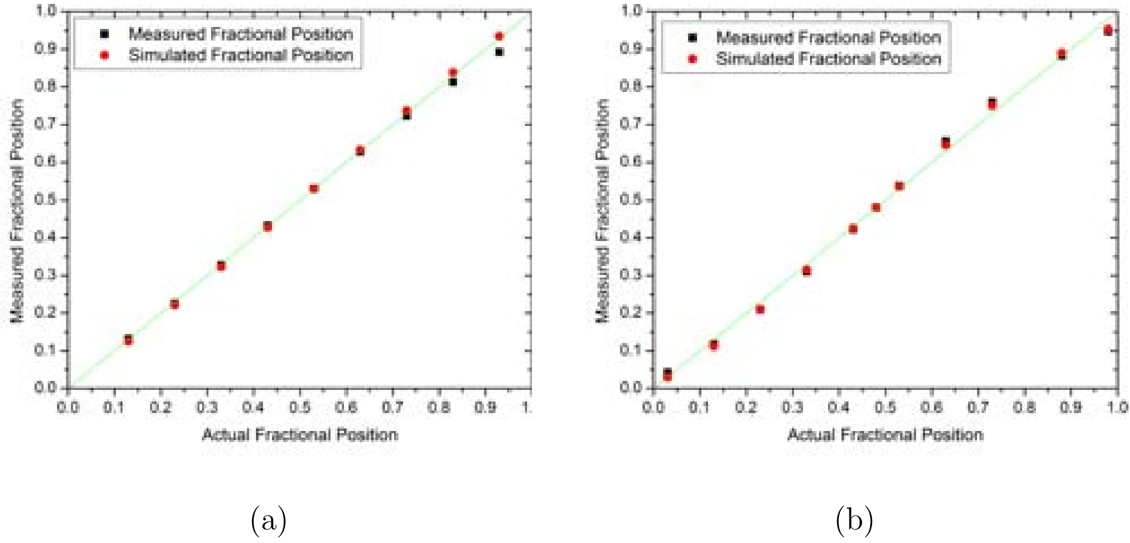

(a) (b)

Figure 3.12: *Experimental results compared with the simulation and the ideal case (green line) for both values of the electrode resistance: (a) R l = 2.8 Ω μm and (b) R l = 12.2 Ω μm.*

spot against the position given by the displacement of the micrometric stage. The comparison with the ideal linear behaviour given by equation 3.1 is shown as well as the comparison with the simulation data. We observe the degradation of the linearity of the detector response due to the systematic error introduced by the non-constant ballistic deficit: the higher the value of the electrode resistivity, the deeper the discrepancy between the data and the expected values. At this stage, before any noise considerations (it has been considerably averaged out in the experimental analysis), the simulation data and the experimental data show a similar systematic behaviour. The good agreement between these results confirms that the electrical simulation reproduces properly the systematic errors due to a non-optimal shaping time and as a consequence, this study validates it as an important design tool for sensor optimization. Actually, in order to meet the different requirements on the strip geometries and on the shaping time of the readout electronics, it is possible to tune the electrode resistivity without changing the diode structure of the sensor.

The residuals of the low resistive electrode sensor (see figure 3.13) increase for larger values of the fractional position: this effect was caused by an experimental error, that generated a slight progressive misalignment between the stage scanning direction and the electrode.

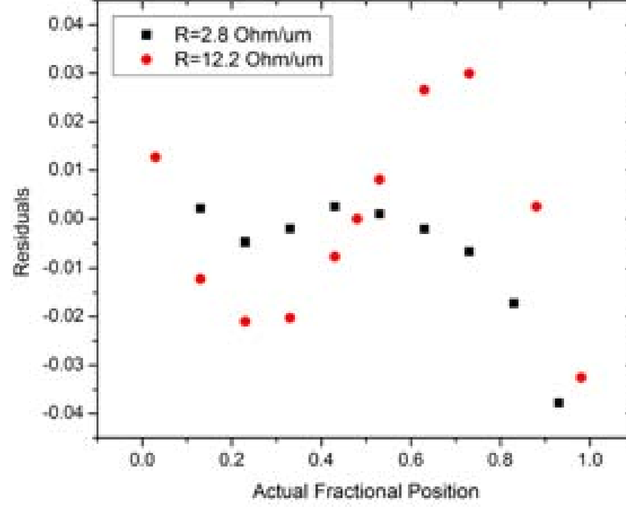

Figure 3.13: *Residuals of the experimental results.*

3.3.3 Spatial resolution and noise considerations

Considering the average noise fluctuation registered by the ALIBAVA system for each sensor, it is possible to estimate the fractional position error for 6 MIPs signals, using equation:

$$\sigma = \frac{A_1 A_2}{(A_1 + A_2)^2} \sqrt{\left(\frac{\sigma_{A_1}}{A_1}\right)^2 + \left(\frac{\sigma_{A_2}}{A_2}\right)^2 - 2\rho\left(\frac{\sigma_{A_1}}{A_1}\frac{\sigma_{A_2}}{A_2}\right)} \tag{3.2}$$

where σ_{A_1} and σ_{A_2} are the noise fluctuations of A_1 and A_2, and the correlation parameter ρ have been calculated as follows:

$$\rho = \frac{< A_1 A_2 >}{(\sigma_{A_1'} \sigma_{A_2'})} \tag{3.3}$$

Here A_1 and A_2 represent the noise excursions with respect to the mean value of the corresponding amplitude and $\sigma_{A_1'}$ and $\sigma_{A_2'}$ are the sigma parameters obtained from the Gaussian fit of the amplitude distributions.

As reported in section 1.3.2, in a silicon detector read out with a charge sensitive amplifier followed by a shaping state, the signal read is affected by different sources of noise. In the majority of the cases, the most important contribution is due to the input circuit component of the preamplifier followed by the statistical fluctuations of

the leakage current (shot noise). In this type of detectors, the thermal noise due to the resistive electrode has also to be considered: it can be represented by a current source in parallel with the input, with average intensity proportional to 1/R and a frequency independent spectrum [65], [73]. Any other noise source is negligible in this context.

Each source contributes to the value of σ and ρ in a different way. Remember that ρ can assume values in the range (-1;1), where $\rho = -1$ represents full anti-correlation, $\rho = 1$ full correlation and $\rho = 0$ represents uncorrelation.

The amplifier noise is associated to the input transistor of the amplifier, therefore, considering both channels of an electrode, it is uncorrelated and one should expect of similar amplitudes, when using similar electronics at both ends; under this assumptions this noise parameters are:

$$\sigma_{A1} \quad \sigma_{A2}; \rho = 0 \tag{3.4}$$

Making explicit the σ dependence on the fractional position of the laser impinging point $x = A_2 \ \ (A_1 + A_2)$ in equation 3.1, one obtain:

$$\sigma_x^2 = \frac{1}{(A_1 + A_2)^2}[(L - x)^2\sigma_2^2 - 2x(L - x)\rho\sigma_1\sigma_2 + x^2\sigma_1^2] \tag{3.5}$$

And in combination with equations 3.4:

$$(\sigma_x^{Amp})^2 = \frac{1}{(A_1 + A_2)^2}[(L - x)^2\sigma_{A2}^2 + x^2\sigma_{A1}^2] \tag{3.6}$$

Thus, the contribution of each amplifier to the position resolution is higher when the distance to the impinging point is higher. Total contribution should follow the geometrical symmetry with respect to the centre of the strip.

The statistical fluctuations of the leakage current is fully correlated if we assume that both ends should sense the same increase or decrease of the leakage current; besides the current excursions at both ends should be the same by symmetry. Under these two assumptions we get the following noise parameters:

$$\frac{\sigma_{A1}}{\sigma_{A2}} = 1; \rho = 1 \tag{3.7}$$

Applying these parameter to equation 3.5 we get:

$$(\sigma_x^{Shot})^2 = \frac{1}{(A_1 + A_2)^2}[(L - x)\sigma_{A2} - x\sigma_{A1}]^2 = \frac{\sigma_A^2}{(A_1 + A_2)^2}(L - 2x)^2 \tag{3.8}$$

Thus the shot noise introduces a quadratic dependence with the position of the laser, being zero at the centre of the electrode and maximal at the edges.

The thermal noise excursions at both ends of the electrode, due in particular to the electrode resistivity, have the same magnitude but opposite sign, that is:

$$\Delta A_1 = -\Delta A_2; \sigma_{A1} = \sigma_{A2} \equiv \sigma_A; \rho = -1 \tag{3.9}$$

Therefore accordingly to equation 3.5 the thermal noise effect on the fractional position resolution σ_x is independent of the position and it is dominated by the SNR as it is given by the following expression:

$$(\sigma_x^{Therm})^2 = \frac{1}{(A_1 + A_2)^2}[(L-x)\sigma_A + x\sigma_A]^2 = \frac{L^2\sigma_A^2}{(A_1 + A_2)^2} \tag{3.10}$$

Even though we can not consider it as a source of noise intrinsic to the detector, it is worth to discuss here the effect on the fractional position resolution of the laser intensity fluctuations among the 20000 pulses recorded at a given scanning position when carrying out the laser-based characterization of the sensor prototypes. This contribution, as the case of leakage current fluctuations, is fully correlated and its noise parameters are given by:

$$\sigma_{A1}^{Laser} = \beta A1; \sigma_{A2}^{Laser} = \beta A2; \rho = 1 \tag{3.11}$$

where β is a positive constant which characterize the laser stability. Applying these parameters to equation 3.5 we get:

$$(\sigma_x^{Laser})^2 = \frac{\beta^2}{(A_1 + A_2)^2}[(L-x)A_2 - xA_1]^2 = \beta^2[(L-x)x - x(L-x)]^2 = 0 \tag{3.12}$$

As a result, we conclude that the laser intensity fluctuation does not have any contribution to the position measurement error, but it influences the value of the correlation parameter.

After these considerations, we expect that the contribution to the position measurement error in our prototype sensors arises from the amplifier σ_{Amp} (quadratic dependence), the leakage current (symmetric and quadratic) and the electrode resistance (constant). We have measured the noise in absence of laser or other signal (defined as the width of the pedestal) obtaining a value of 1.83 ADU and 1.80 ADU respectively for the noise of A_1 and A_2 readout channels, raw data are shown in Figure 3.14. The correlation plot between A_1 and A_2 noise excursion is shown in Figure 3.15, the lack of correlation implies that the uncorrelated noise component (amplifier noise) dominates.

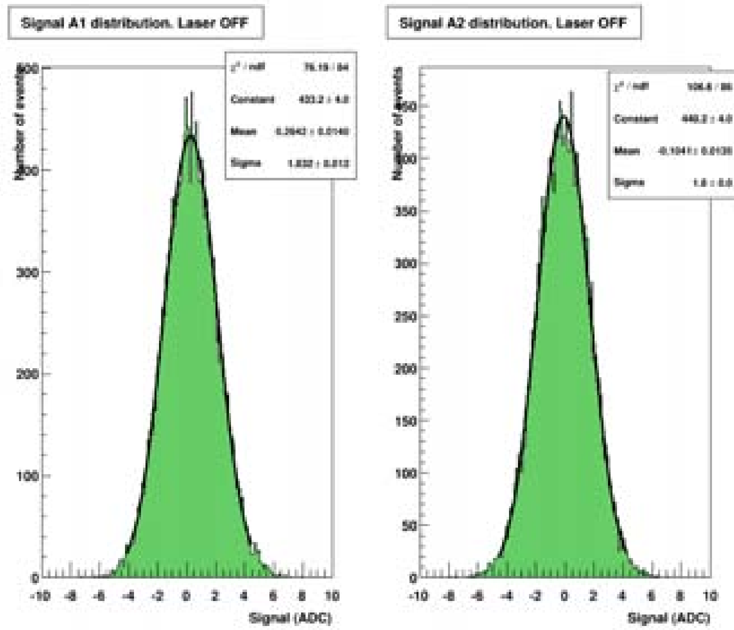

Figure 3.14: *Raw distribution of pedestals*

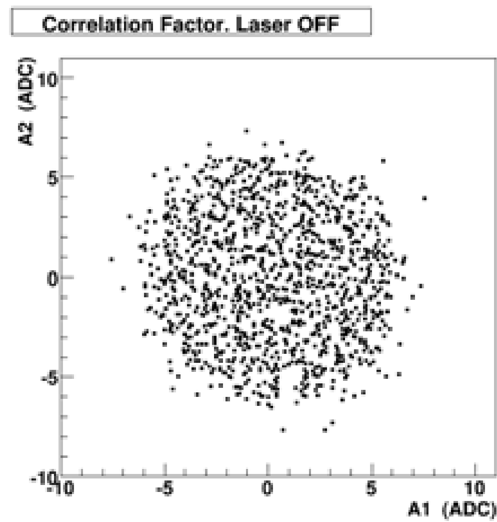

Figure 3.15: *Simultaneous Noise excursion between the opposite ends of the same electrode in absence of laser pulse. Correlation parameter ρ is 0.03.*

When the correlation parameter is calculated with the laser switched on its value increases as expected and the main values for the two prototypes are ρ = 0.19 and ρ = 0.34 respectively.

Using these values, the sigma (σ) has been computed for each of the scan points. Figure 3.16 shows the error dependence on the position for both sensors. The σ value strongly depends on the Signal to Noise ratio, that depends on the total charge created by the ionizing event as well as on its position along the strip. Therefore, the mean values of the spatial resolution obtained are 1.1% and 1.2% of total strip length for the prototype with electrode resistance $R\ \ l = 2.8\ \Omega\ \ \mu$m and $R\ \ l = 12.2\ \Omega\ \ \mu$m respectively.

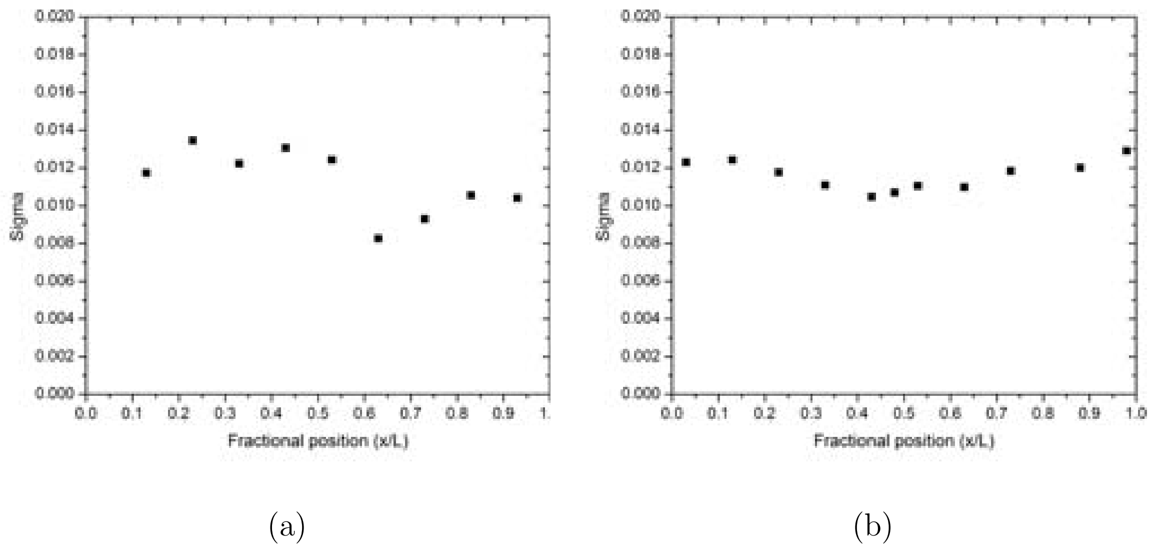

Figure 3.16: *Calculated fractional position error for prototype with electrode resistance (a) $R\ \ l$ = 2.8 $\Omega\ \ \mu m$ and (b) $R\ \ l$ = 12.2 $\Omega\ \ \mu m$.*

Considering that both detectors are characterized by the same total capacitance, but by different values of the electrode resistance, they should have the same voltage component of the total noise, but a higher current component for lower electrode resistances (see section 1.3.2). A simulation of the thermal noise of both detectors studied here has been carried out using the simulation model presented in section 3.2.2. Figure 3.17 shows the results. Integrating over the frequencies range, the noise associated to the more resistive electrode results to be a 40% lower than the value obtained for the less resistive electrode. On the other hand, figure 3.7 shows clearly how an higher resistance cause a stronger attenuation of the signal: the signal read from the more

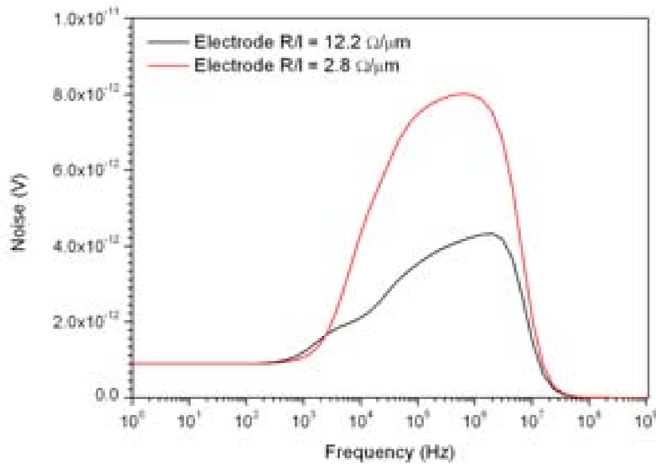

Figure 3.17: *Simulated noise spectrum of both the detectors.*

resistive electrode in the best case undergoes an additional 45% or higher attenuation with respect to the other. For this reason the resultant signal to noise ratio due to the thermal noise is higher when the resistance of the electrode is lower. Then, the study carried out on the correlation parameter shows how the amplifier source of noise (voltage component) fully dominates on the others sources (short shaping time, see equation 1.37), including the thermal noise source (current component) associated to the resistive electrode. This explains the similarity between the spatial resolution of two detectors that differ from each other in the electrode resistance by a factor ≈4, but have the same resultant capacitance. Therefore, reducing the total noise signal, i.e. improving the spatial resolution of the sensor for a fixed ionization event, is possible mainly reducing the total shunt capacitance at the amplifier input (or reducing the internal noise of the amplifier). The main component of this capacitance is the interstrip capacitance of the detector, that depends on the strip-width/pitch ratio (see section 1.3.2 and 2.5). Changing these parameters calls for attention to their influence on the full depletion of the device as well as on the spatial resolution in the transverse coordinate.

From another point of view, the signal to noise ratio will be optimal when the shaper time constant will be proportional to the detector time constant and hence to the rise time of the pulse that travel along the electrode (see section 3.1). In this way, ballistic deficit effect can also be avoided.

Therefore, the best result can be achieved by choosing the electrode resistance keeping the detector time constant small (in order to maintain the shaper time constant reasonable) and making the total capacitance of the detector as small as possible, without affecting the others characteristics of the device.

3.4 A possible alternative configuration of the electrode

In order to use only one chip to read out the detector another prototype has been designed and fabricated with a different configuration of the electrodes. The sensor consists of 34 p^+ strips 20 μm wide, 1.4 cm long and with a pitch of 160 μm on a (285±15) μm thick n-type substrate. The resistive material used is still highly doped polysilicon with linear resistance R l=20 Ω μm.

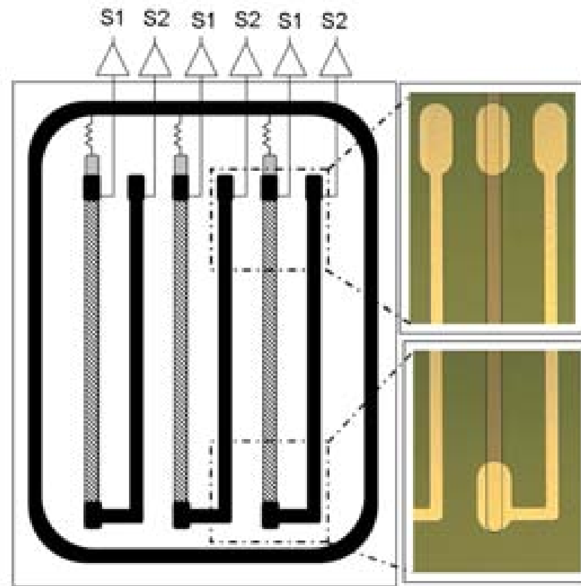

Figure 3.18: *Schematic top view of the first prototype (not in scale)(left). The black colour refers to aluminium structures while the striped elements represents the resistive electrodes on the strips. The strip implants pitch is 160μm while the readout pitch is 80 μm due to the aluminium tracks. The two photographs on the right side show the actual prototype layout at the electrode ends.*

As shown in figure 3.18, aluminium routing has been added during the metal sputtering step of the fabrication process. The result is the location of all the contact pads

in the same region of the detector surface, that allows their connection to the channels of only one readout chip.

The results of the electrical characterization of the prototype are still consistent with the ones obtained by standard detectors: the measured values are listed in table 3.3.

Table 3.3: *Measured values of the polycrystalline silicon electrode resistance (R_{el}), depletion voltage (V_{dep}), breakdown voltage (V_{bd}), bias resistance (R_{bias}), interstrip resistance (R_{int}), interstrip capacitance (C_{int}) and coupling capacitance (C_{AC}).*

strip width	V_{dep}	V_{bd}	R_{bias}	R_{int}	C_{int}	C_{AC}	R
μm	[V]	[V]	[MΩ]	[pF/cm]	[pF/cm]	[Ω μm]	
20	40	>400	1.31	>GΩ	0,6	173	20

As done for the other prototypes, the performances of this alternative detector have been simulated with Spectre. The same model of the front-end electronics as well as the same current pulse has been used. The detector model was composed of 56 cells identical to the one represented in figure 3.4 with the values of the parameters listed in table 3.4.

Table 3.4: *List of the values of the model parameters.*

R_{el}	R_{impl}	C_{AC}	C_{sub}	R_{sub}	R_{int}	C_{int}
2500 Ω	800 Ω	3.43 pF	16.6 fF	20000 GΩ	15 GΩ	24 fF

The aluminium routing system has not been included in the model in order to study their effects on the detector performance comparing the simulation with the experimental results. The simulated fractional position A_2 $(A_1 + A_2)$ of the pulse generator is shown in figure 3.19 as a function of the actual fractional position (y/L).

The well known effect of the ballistic deficit on the detector response linearity is pointed up by comparing the simulated data with the prediction of equation 3.1 (green line).

The detector has been wire bonded to one Beetle chip of the daughter board of the Alibava DAQ system and a longitudinal scan of one strip has been performed

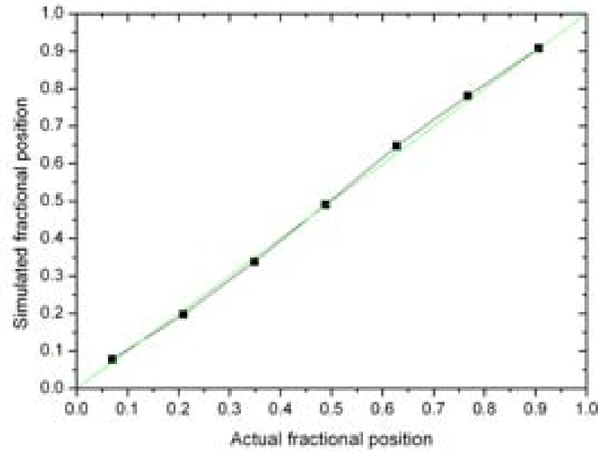

Figure 3.19: *Simulated fractional position as a function of the nominal one. The green line represents the linearity predicted by equation 2.1.*

using the same experimental setup and pulses shape reconstruction method described in section 3.3. We scanned the whole electrode length (14 mm) with a scanning step of 2 mm, reconstructing, for each position, the pulse shape at the output of the front-end electronics shapers stage in order to calculate the fractional position of the laser beam.

In figure 3.20 the experimental data are displayed together with the simulation. Even if the effects of the ballistic deficit are well represented, it is possible to notice a discrepancy between the two sets of data due to the contribution of induced signals to the aluminium tracks. The origin of this signal component is a parasitic capacitance between the metal routing and the strip, this decreases getting close to the connection between the aluminium line and the polysilicon electrode.

These results highlight the importance of improving isolation between strips when a metal routing system is integrated.

3.5 Summary and discussion

In this chapter a novel 2D position-sensitive semiconductor detector concept has been presented. It is based on the resistive charge-division readout method and prototypes were fabricated using the standard technology of AC coupled microstrip detectors. The implementation of resistive coupling electrodes allows to extract the information

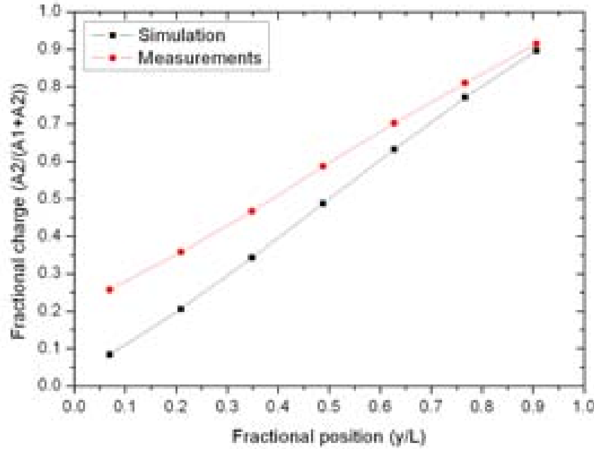

Figure 3.20: *Measured fractional position compared with the simulated one. The signal induced on the metal guides contributes to signal S_2 generating a shift of the results from the simulation expectation.*

on the longitudinal coordinate of an ionizing event using the resistive charge-division method.

Two proof-of-concept prototypes have been produced with strips 20 mm long and with different linear resistances of the electrodes: $R\ l = 2\ 8\ \Omega\ \mu$m and $R\ l = 12.2\ \Omega\ \mu$m. A first investigation of their performance has been carried out using a Near Infra-Red laser and readout electronics based on the Beetle ASIC. Results show that the mean spatial resolution for a 6 MIPs signal is 225 μm and 232 μm for the two prototypes respectively. The possibility of using only one read-out chip for each detector has been also investigated, integrating metal routing in order to locate all the connection pads in the same region on the surface of the detector. The study carried out highlights the importance of a good insulation between the strips in order to reduce the effects of parasitic capacitances.

An electrical simulation of the sensor equivalent circuit -including the amplifying and filtering stages- has been developed and benchmarked against the experimental data. The simulation allowed to highlight the effects of the propagation of the signal pulse along the dispersive electrodes: the amplitude attenuation and the increase of the peaking time that cause a systematic non constant ballistic deficit when non optimized front-end electronics is used to read the signal. The good agreement with the experi-

mental results in reconstructing the fractional position of the signal generation point validates the electrical simulation as an adequate tool for future sensor optimization.

This initial study demonstrates the feasibility of the resistive charge division method in a fully fledged microstrip sensor with resistive electrodes. Specific studies on detection of minimum ionizing particles are in progress to assess its soundness as tracking technology for the future particle physics experiments: the analysis of the data recorded with a pion test beam at the CERN SPS beam line H6 is being carried out; nevertheless, in its current conception, this implementation appears as a suitable technology for highly ionizing particles as it is the case of neutron monitors based on conversion layers or other nuclear imaging technologies ranging from Compton cameras to heavy-ion detection.

In view of future prototypes fabrication it is worth to pay attention to the optimization of the spatial resolution. As seen in section 3.3.3 it strongly depends on the signal to noise ratio, that will be optimal when the shaper time constant is proportional to the detector time constant. Considering the detector design, the detector time constant should be kept small and the interstrip capacitance as small as possible, without affecting the others characteristics of the device.

Using the simulation model described in section 3.2.2, relative values of the detector and shaper time constants can be adjusted in order to eliminate the sistematic effect of the ballistic deficit. Then, depending on the experiment and the electronics used, it is possible to replace the model of the ideal readout electronics with the one of the real chip and definitely tune the parameters of interest to optimize the signal to noise ratio.

Chapter 4

Stripixel detectors

In the previous chapters two single-sided detectors characterized by microstrip electrodes have been introduced and studied. The attention has been mainly focused on the possibility of obtaining specific capabilities, e.g. IR light transparency or 2D position-sensing, by properly changing some parameters of their simple design and standard technology.

Since 2003, other electrode geometries and technologies are being studied at the Brookhaven National Laboratory of New York [74] in order to obtain a device that could provide 2D position-sensitivity with a moderate number of readout electronic channels and single-sided detector fabrication process. The concept is based on pixel electrodes arranged in a projective X-U read-out configuration that allow to use a minimum number of readout channels (2N) to process the information read from N^2 pixels. Many designs and prototypes of so called *stripixel* detectors have been developed over the years [75],[76], [77].

The first generation consisted of planar p^+-in-n pixel detectors, in which the n^+ electrode was uniformly implanted from one side of the substrate, while the p^+ electrodes, on the other side, were divided into X- and Y-cells, and two metal layers were used to readout the pixels by means of two sets of crossed strips on the detector surface. An attempt to move and segment the n^+ electrodes to the same side of the p^+ failed due to difficulties in generating the electric field inside the substrate. Then, the interest in radiation-hardness and true single-sided processing has led to a deeper investigation in 3D technology and new electrodes arrangements, both types on one side of the bulk. New technologies have been proposed based on mixed planar/3D processes

(single-column) and full 3D (double-column) process.

3D detector technology, based on a deep reactive ion etching process, is at the moment available in only three investigation centres around the world, among which, the IMB-CNM of Barcelona. For this reason a collaboration between the BNL and the IMB-CNM started in 2006 in order to carry out the full process of the new prototypes.

In this chapter, after a brief overview of the stripixel concept and the different designs proposed over the years, the last prototypes, designed and totally fabricated in the IMB-CNM clean room facilities, will be presented.

The new device is a dual-column 3D detector in which the p^+ and n^+ columns are both processed on one side of the wafer and arranged in quincunx pattern (with the p^+ columns as the central elements). A net of perpendicular strips is defined on the surface by means of two different metal layers to allow a projective X-Y read out. 3D and 2D simulations have been performed in order to optimize the design of the devices, then they have been fabricated. The processes flow, including a total of 10 photolithography steps, has been the most challenging ever carried out at the IMB-CNM for silicon detectors fabrication. After it, many samples and test structures included in the wafer have been electrically characterized. The active area limitations have been investigated with the use of Transient Current Technique measurements, performed with different lasers of different wavelengths in the BNL instrumentation division laboratory. Finally, two-dimensional position sensitivity has been tested using a collimated laser set up and the ALIBAVA readout system in the IFCA clean room facility in Santander. The development of the device supported by the simulation study will be presented in the next sections as well as the experimental results.

This work has been carried out within the CERN RD50 collaboration, which has the purpose of developing new high radiation hard detectors for future high luminosity colliders (see section 1.4.1).

4.1 Stripixel detector concept: state of the art

In 2004 Z. Li presented the *stripixel* detector concept and the simulation, design and fabrication of the first prototypes fully carried out at the BNL [75]. The idea was combining the advantages of a double-sided *strip* detector with the ones of a

pixel detector, obtaining a single-sided device, 2D position-sensitive, with a minimum number of readout electronic channels.

The proposed devices were planar p^+-on-n pixel detectors with the n^+ electrode extended over one side of the substrate and the p^+ pixels (DC or AC coupled with the electronics) on the other side, divided into X- and Y-pixels (Alternated Stripixel Detector, ASD) or each and every one into X- and Y-cells (Interlaeved Stripixel Detector, ISD). In the fabrication, double-metal technology was used to organize the pixel readout into two sets of crossed strips (X and Y-strips) on the detector surface. The insulator separating the two Al layers was polymide with a thickness of about 1-2 μm. In the same paper, the possibility of creating a stereo angle α between the X- and Y-strip (and/or adding a third set of readout channels) is considered to partially resolve the multi-hit ambiguity problem (see section 1.2.1). For instance, a schematic of the electrode configuration chosen for the Phenix upgrade at RICH (BNL) [78], [79] is shown in figure 4.1.

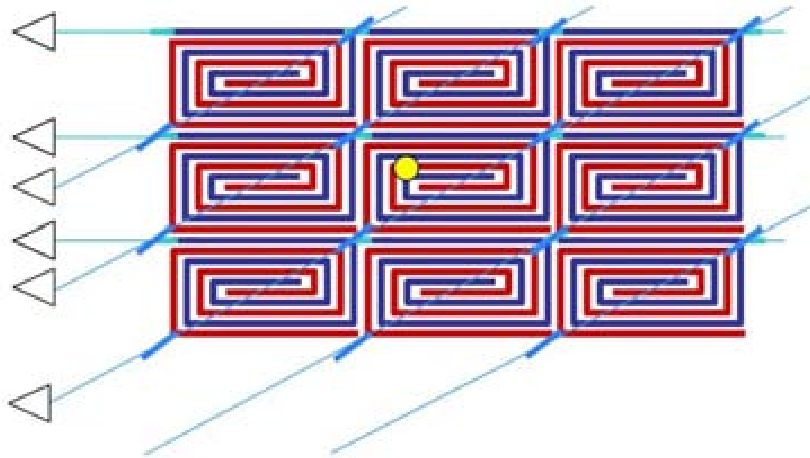

Figure 4.1: *Schematic of the interleaved electrode configuration chosen for applications in the Phenix upgrade at the BNL.*

It consists of interleaved rectangular spirals forming the pixels (DC ISD) organized in a X-U projective readout, characterized by a stereo angle of 4.6°. In this way, the charge cloud (yellow circle) created by the ionization, after spreading by diffusion can cover both X- and Y- cell anywhere in a pixel or between neighbouring pixels. The effective pixel size, considering the stereo angle effects, is 80×1000 μm^2, that provides

a spatial resolution of 33.6 μm for X-stripixel (35.2 μm for U-stripixel) and a signal to noise ratio of 10.4.

Then, in 2005 a collaboration with the IMB-CNM started with the purpose of integrating in the stripixel concept a partial (single column) or a full (dual column) 3D processing of the electrodes. The idea was to address this new investigation to these applications that would demand high radiation hardness of the instrumentation.

As introduced in chapter 1.2.3, 3D detectors have the capability to withstand high radiation fluences. Thanks to the very short distance between electrodes, their depletion voltage is substantially reduced with respect to planar detectors, and it should be possible to fully deplete them after high radiation doses as well as reducing charge collection degradation. These characteristics make 3D detectors suitable for applications in experiments in future accelerators, characterized by a severe radiation environment such as the case of LHC upgrade (HL-LHC).

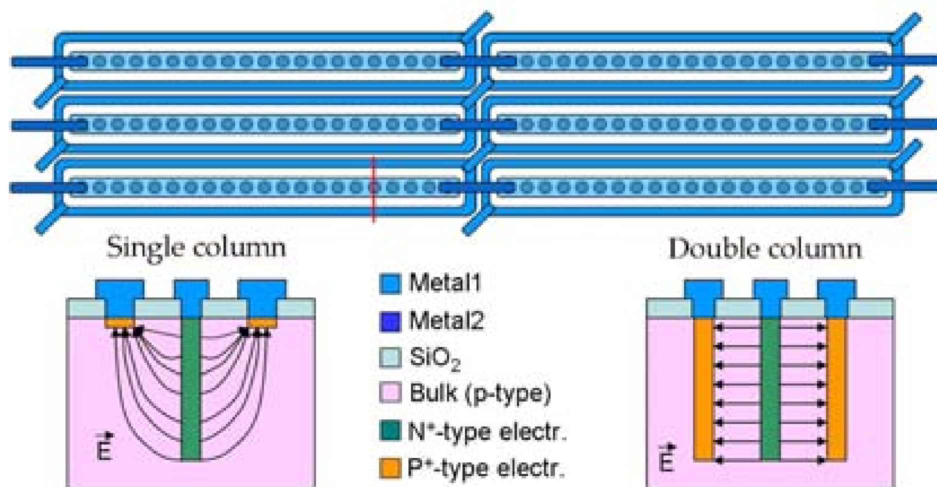

Figure 4.2: *Schematics of the stripixel electrode arrangement in the single column and dual-column device. The top figure showsa detail of the detector layout, while the bottom figures show a section of one cell (red line) is represented for the single column and the dual column case on the left and on the right respectively.*

The new 3D detectors were designed to have true single-sided process and both p^+ and n^+ electrodes on one side of the detector. The design of two different devices has been developed: one with dual-column (p^+ and n^+) electrodes and another with single-column and planar electrodes (p^+ or n^+). A comparison between one half of a single cell

of both the devices is shown in figure 4.2, under the schematics of the pixels layout. A mask set was completed and used for a prototype run of single-column stripixel detectors with x-pitch of 1000 μm and y-pitch of 80 μm. The n^+ columns, 240 μm deep, have been etched by IMB-CNM of Barcelona on a batch of 300 μm thick FZ p-type Si wafers, then BNL finished the remaining planar processing involving phosphorus implantations to connect the n^+ columns of each pixel, p^+ electrodes implantation and two-metal layers deposition and isolation. Electrical simulation demonstrated that detectors would be characterized by lower electric field regions expecially under the p^+ implants.

4.2 New prototype generation: a single side double strip detector

In 2009 the development of dual-column 3D stripixel detector started. The generic layout of the new device consists of p^+ and n^+ columns, both etched from one side of the bulk and connected by means of two layers of metal strips crossed on the surface. The main purpose of this project was to test the capability of the double-metal readout and the complexity of the dual-column technology applied to the same surface. A simple schematic of the device is shown in figure 4.3.

4.2.1 Optimization of the design: device simulation

The final layout of the detector has been decided after a preliminary study of its behaviour by means of computer simulations. The interest was focused on the electric field (electrostatic potential) distribution inside the silicon bulk, for different values of V_{bias} and for different doping types (n or p) and electrodes (guard ring) configurations. The aim was improving the guard ring isolation capability and reducing the effects of the defects introduced by the saw cut at the edges of the device (see section 1.2.4),in order to properly define the active area of the sensor. For this purpose Synopsys TCAD Sentaurus [80], a finite-element semiconductor simulation package, has been used.

In section 1.1 the basic differential equations of semiconductor physics were introduced. By solving these equations with appropriate boundary conditions, the behaviour

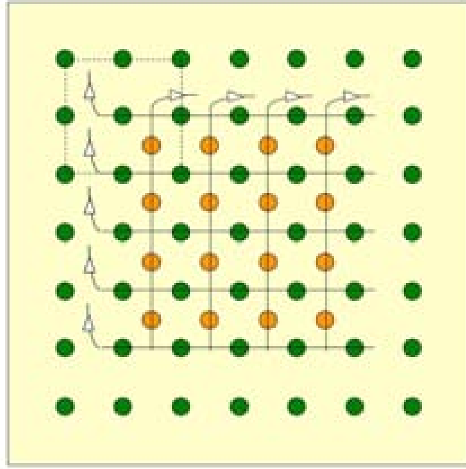

Figure 4.3: *Generic schematic of the new full 3D stripixel detector. A matrix of n^+- and p^+-type columns is etched in the detector bulk in a quincunx pattern with the p+ columns as the central elements. The active area is surrounded by a guard ring made up of columns of the same type of the external columns of the active area. Shaded square represent the portion of the device modelled for the 3D simulation(section 4.2.1). Drawing not to scale.*

of a semiconductor device can, in principle, be found analytically. However, in practice this can only be done for relatively simple devices and conditions. For more complex devices, such as the detectors presented in this chapter, a solution is to represent the device structure by a mesh of discrete nodes, and to apply the semiconductor equations to each point in an approximate form. These can then be solved to an acceptable level of accuracy by iteration methods [81]. With Sentaurus Structure Editor and Mesh the 2D or 3D device structure, i.e. the materials composition, the geometry and position of the electrodes and the electrical contacts can be defined as well as the various doping profiles within the silicon.Then, Sentaurus Device program can be used to simulate electrically the behaviour of the device. During the simulation, each node will be characterised by its own electrostatic potential and the electron and hole quasi-Fermi potentials , which are proportional to the natural logs of the electron and hole concentrations. In this representation, the volume between the nodes is split up into a series of elements. The values of the three variables are defined throughout each element by taking the values at the surrounding nodes and applying a linear interpolation process [83], i.e. it is assumed that, between nodes, the electrostatic potential and quasi-Fermi potentials vary linearly. So, if the value of some variable changes rapidly

across a region containing few nodes, the accuracy of the simulation will be reduced. However, as the number of nodes increases (there is a limit for 2D and 3D models), the resulting system of equations gets larger and the solving process becomes slower and more difficult. To avoid these problems it is possible to use a high mesh density only in the regions where the doping concentration changes rapidly or the electric field is high. For the same reason, considering the large size of semiconductor detectors with respect to common micro- or nano-electronic devices (to which Synopsys TCAD is mainly dedicated), it is advisable to model as carefully as possible only a portion of the detector. Actually, in general, a detector will have a repetitive structure, with many pixels or strips, and in a steady state it will have a repetitive field pattern, carrier densities etc. At the contacts, the boundary conditions generally consist in a fixed electrostatic potential, and neutrality of charge. At the boundaries of the device mesh, the default conditions are that the electric field and current densities normal to the boundary are zero. These are referred to as reflecting or Neumann boundary conditions and are also applied to the external surface of dielectric layers such as SiO_2. In a real detector in a steady-state, these conditions will naturally occur along planes of symmetry inside the device as well as along the external surfaces when the chip is clean . This means that basic steady-state simulations can be done using just the simplest repeating unit of the detector. However, in order to investigate the electric field distribution in the bulk of the detector close to its edges, the simulations presented in this section involve a larger region of the detector and 2D simulations have been performed of wider sections. In figure 4.4 the two main structures considered in the 3D simulations are shown. In both cases a corner (see figure 4.3) of the active area and of the guard ring of the sensor is considered. The guard ring of the sensor has a squared shape made up of just one line of columns of the same type of the external columns in the active area, in order to fix to zero the electric field outside the active area. The distance between columns of the same type is 80μm, so the simulation mesh has a volume of 160μm by 160μm by 300μm with more than 300000 nodes. The column type of the guard ring is the same as the bulk and as the external columns of the active area (see figure 4.3). The specific details of the simulated structures are as follows:

- The substrate is 300 μm thick, with constant 5×10^{11} cm^{-3} phosphorus (a) or 1×10^{12} cm^{-3} boron (b) doping.

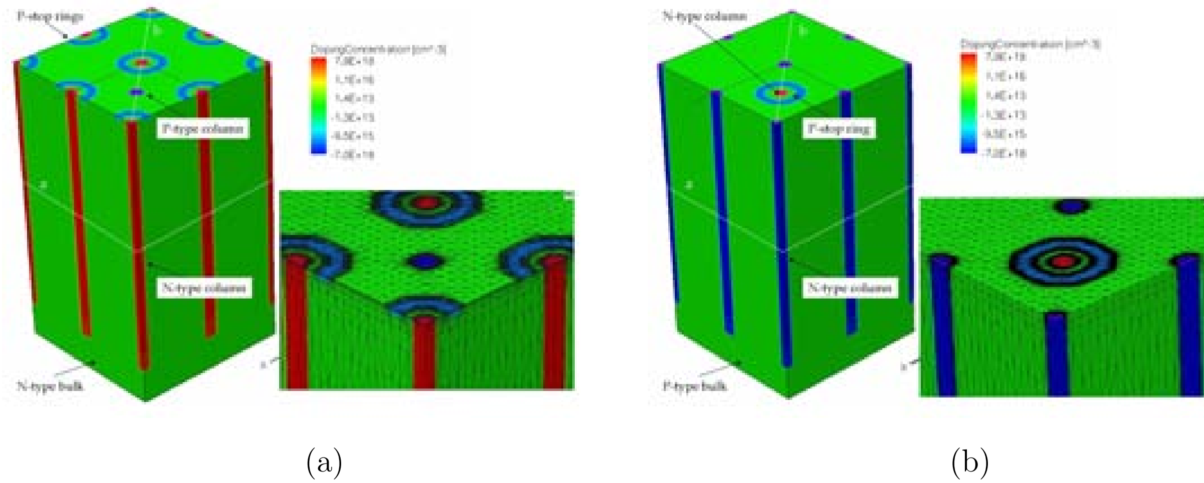

(a) (b)

Figure 4.4: *Main structures simulated: n-type bulk (a) p-type bulk (b). Each n-type column is surrounded by a p-stop ring. The active zone is limited by the dashed lines in the complete structure and a detail of the mesh is shown.*

- The columns are cylindrical and 5 μm in radius. To simplify the structure, the columns are totally filled with doped silicon, whereas polysilicon is used in real devices and they are not totally filled (see section 4.3). The n- and p-type columns have $1{\times}10^{19}$ cm^{-3} phosphorus and boron doping respectively. The doping profile at the edge of each columns is an error function, which increases the radius of the junction around the columns to about 7 μm.

- The n^+ columns are isolated using a p-stop ring around each one on the top surface. The boron doping has a Gaussian profile with peak concentration of $1{\times}10^{17}$ cm^{-3}.

- The front and back side of the device are both covered by a 1 μm thick oxide layer.

Doping concentrations and profiles have been chosen to be as close as possible to the real detector.

A detail of the mesh strategy is also shown for both structures. The mesh spacing is higher around the columns, where the doping concentration varies rapidly with position, and at the oxide/silicon interface, where the trapped charge affect the device behaviour. Between the columns, the electrostatic potential, hence the electric field,

varies rapidly with the horizontal coordinate, but not along the z-direction. As a consequence, the vertical mesh spacing is wider.

After creating the mesh, the Sentaurus Device program has been used inside the Workbench framework to run the simulations. The physics models needed in the simulation can be specify in the text file that control the program, as well as the conditions that one want to simulate. Starting from the basic semiconductor physics equations, Synopsys accepts many different and more complicated models in order to correctly handle with the full device as well as with specific regions or conditions inside its volume. In the simulations presented in this section, the mobility of the carriers was taken into account using doping-concentration-dependent and high-field-saturation-dependent physical models. This means that the electron and hole velocities cannot increase without limit as the electric field gets stronger, but will instead reach a saturation velocity. Then, the carrier generation and recombination rates are based on a Shockley-Read-Hall model and depend on the electron and hole concentrations and the doping density.

In order to account for the state charge induced at the interface between the silicon substrate and the oxide layer discussed in sections 1.2.4 2.4.1, a fixed positive charge of $2{\times}10^{10}$ cm^{-2} has been introduced. Specific information on all the models and conditions available in Sentaurus Device can be found in the dedicated user s guide [82].

Using all the proper models for our structures a quasi-stationary simulation was run, where the bias applied to the detector was steadily increased from 0V to 15V in consecutive steps, to find how the depletion region and electric field pattern develop. At each step, the time-dependent terms in the semiconductor equations are zero and an initial guess at the correct solution is found by extrapolation from the previous solutions; then a global approximate Newton method is used to solve the equations system to an acceptable level of accuracy.

In both structures, the depletion region start from the p^+-type columns and grows cylindrically outwards. The distance between a p-type and a n-type column is 56.6 μm. So, the lateral depletion, i.e. the depletion of the zone between columns of opposite doping, occurs at low voltage, around 4V for both types of bulk. Figure 4.5 shows the electric field strength and voltage distribution in an horizontal cross section (white section (a) in figure 4.5) of both structures in correspondence of the half of the columns

for V_{bias} = 12V. Comparing the results, in both cases, areas of low electric field are

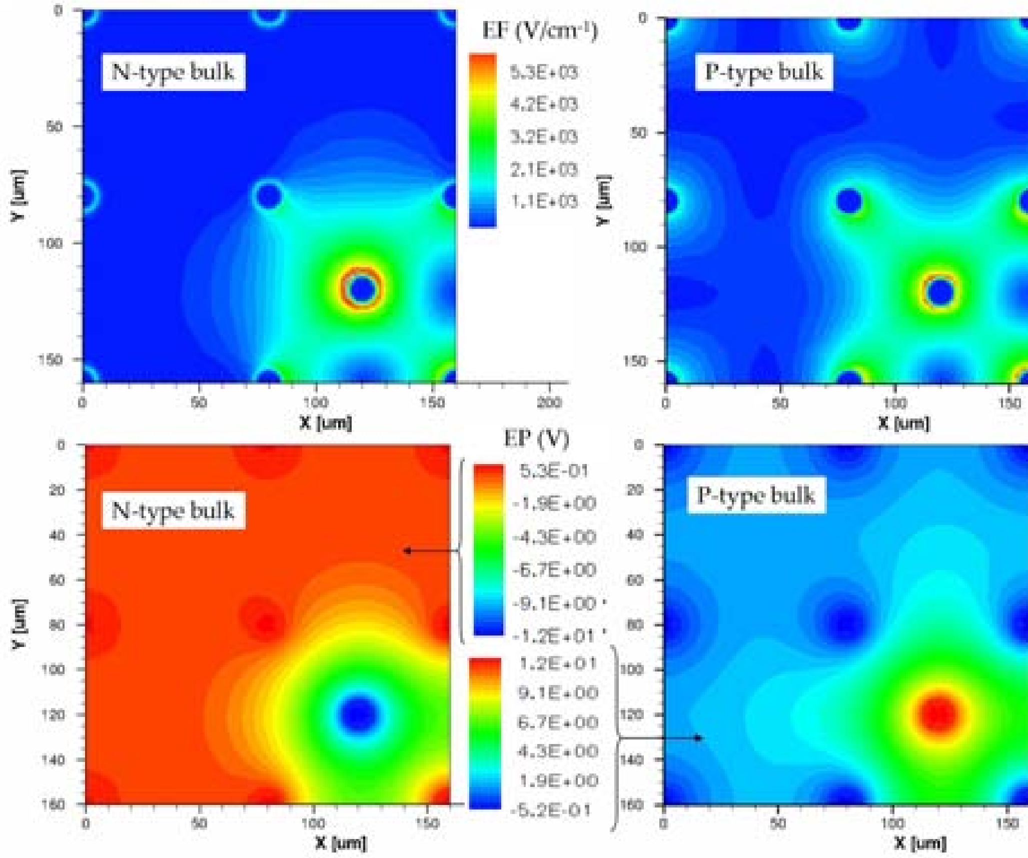

Figure 4.5: *Electric field (top figures) and electrostatic potential (bottom figures) distribution in a horizontal cross section of the simulated structure with n-type (left) and p-type (right) bulk.*

created between columns of the same type, as expected, but in general the field distribution outside the active area appears more homogeneous in the structure with n-type bulk and guard ring columns. The depletion region at the same time expands into the bulk volume under the columns. Nevertheless, it never reach the last few microns of the bulk, due to the accumulation of electrons attracted by the positively charged traps in the oxide/silicon interface. The electric field distribution shown in figure 4.6 refers to a vertical cross section along the white line (b) in figure 4.4. In this case, low strength areas appear beneath the n-type columns and even more clear results the better isolation capability of the n-type guard ring on an n-type bulk.

In order to consider the effects of the defects introduced by the saw cut at the edges of the device, 2D simulations have been performed extending the vertical cross section

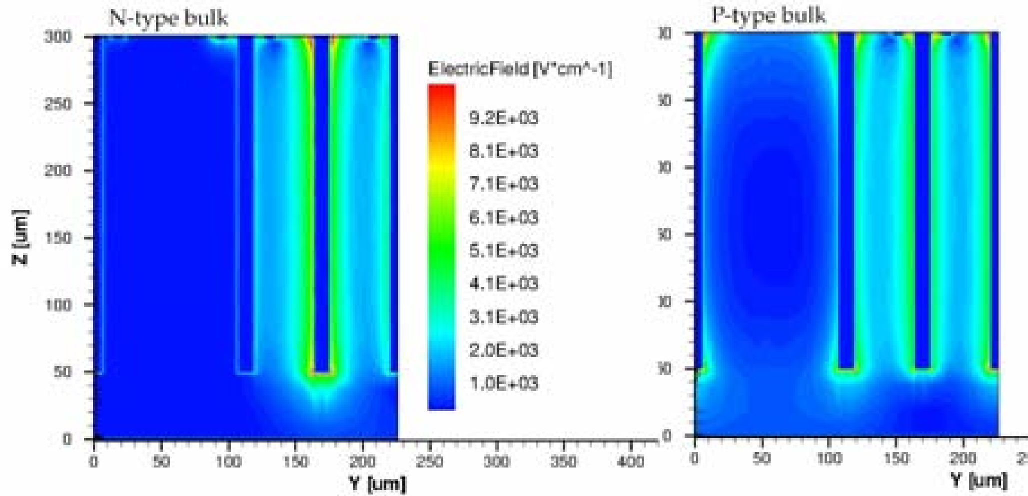

Figure 4.6: *Electric field distribution in a vertical cross section of the simulated structure with n-type (left) and p-type (right) bulk.*

of both models to the edge, 100 μm ($\times\sqrt{2}$ in the cross section) far from the guard ring, and to two more columns inside the active region. The defects along the edge have been simulated using the model presented in reference [84]. It consists in filling consecutive regions (in our case 4 regions 4.5 μm wide) with different concentration of neutral carrier traps (both electrons and holes) with an exponential energy distribution close to the conductive band. Concentration of each trap type decreases from the bare edge inwards. Figure 4.7 shows the results of the simulations concerning the electric field distribution for V_{bias}=12V. Again, the n-type bulk and guard ring result to be more effective in defining and isolating the active area of the detector. Following the hints of these results the n-type bulk configuration has been chosen for the prototypes production.

4.2.2 Layout of the detectors

A mask set has been designed for the production of baby sensors and test structures.

Each device has a surface of 1×1 cm^2 area in which the columns electrodes are arranged in a diamond pattern. The n^+ columns are surrounded each one by a p-stop ring in order to avoid any short circuit through the charges in the silicon/oxide interface between electrodes of different strips (see section 1.2.4). Then, two sets of perpendicular

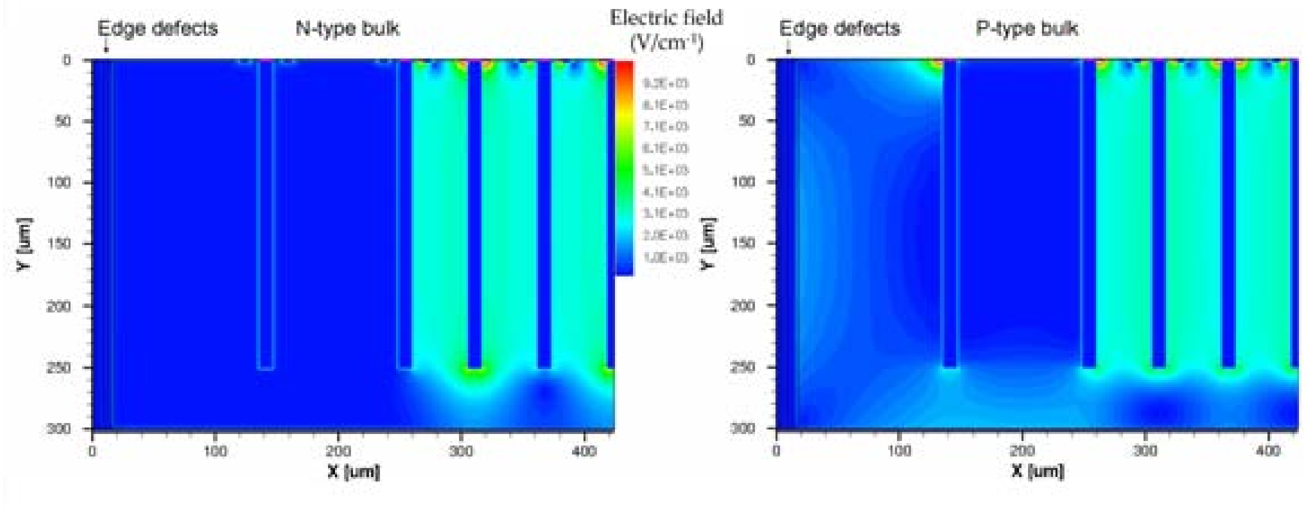

Figure 4.7: *2D simulation Electric field distribution in a vertical cross section of the simulated structure with n-type (left) and p-type (right) bulk.*

metal strips, 127 X-strips (p-type columns) and 128 Y-strips (n-type columns) with a X-pitch = Y-pitch of 80 μm, 10 μm wide and separated by a dielectric layer are defined on the surface directly contacting with the electrodes (Schottky contacts) to allow a projective X-Y read out (see figure 4.3). The active area is surrounded by a guard ring made up of n^+ columns with the same pitch and distance as the others connected by the Y-strips. Other detector models have been considered in the mask design in order to extract information by comparing the results of their characterization. Some devices with X- and Y-pitch of 160 μm have been added as well as some else with pitch of 80 μm but with polysilicon connections between p^+ columns instead of metal[1]. Detectors with 80 μm or 160 μm pitch and readout pads inside the guard ring perimeter have been included in order to investigate the possibility of obtaining detectors with a reduced dead area around the active area.

The mask is then completed by different 1D position-sensitive or diode test structures obtained by shorting the n-type and/or the p-type pads in order to simplify the connection with the electronics chains for different characterization measurements. All

[1]The design of these detectors has been developed at the same time of the design of the detectors presented in the previous chapter. The interest in polysilicon as contact material has been extended to these devices too.

Table 4.1: *Set of optimized thickness leading to maximum %T on 50 μm pitch microstrip detectors.*

Structure	n-type channels	p-type channels	X-(Y-) pitch	strips net	comments
1 (ABCD)	128	127	80	double metal	2D
2 (ABCD)	128	127	80	polySi-metal	2D
3 (ABCD)	64	63	160	double metal	2D
4 (CD)	1	127	80	double metal	1D
5 (CD)	128	1	80	double metal	1D
6 (AB)	1	127	80	double metal	1D parallel
7 (AB)	128	1	80	double metal	1D parallel
8	1	1	80	double metal	diode
9	1	1	80	double metal	diode
10 (ABCD)	128	127	80	double metal	2D, edgeless
11 (ABCD)	64	63	160	double metal	2D, edgeless

the devices are described in table 4.1 and some picture of the real samples are shown in figure 4.8 as well as their arrangement in the wafer area.

4.3 Fabrication process

Six 4 wafers with crystal orientation <100>, a thickness of 300μm and resistivity in the range 5-7 kΩ·cm have been processed together with 2 SOI wafers 20 μm thick, resistivity >1 kΩ·cm and crystal orientation <100>. Ten different mask levels (11 for the SOI wafers), each one associated to a photolithography step, have been used in a processes run including 100 steps, the most complex and large processes flow ever carried out at the IMB-CNM for detectors production. The full mask is summarized in table 4.2.

The processes flow, after the conventional procedure for wafer cleaning, start with the p-stop ring implantation, followed by the n-type columns etching, filling and doping. The p-type columns are successively etched, filled and doped and the lasts step are dedicated to the double-metal connection, passivation and contact pad opening. As

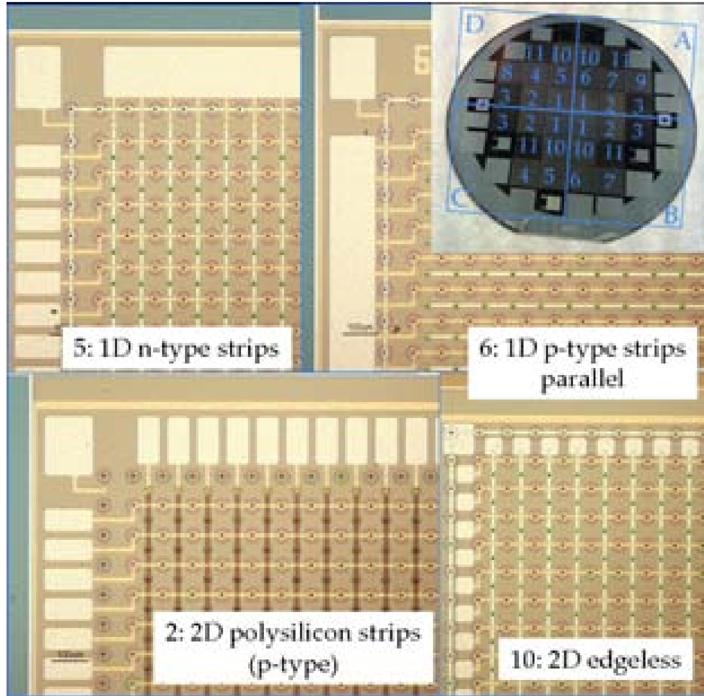

Figure 4.8: *Picture of some structures and their arrangement in the wafer area.*

explain in section 1.2.3 IMB-CNM normally produces double-sided 3D detector, in which the two sets of columns are fabricated from opposite sides of the silicon substrate and do not pass through the full substrate thickness. In the new 3D stripixel detector fabrication special attention has to be paid to protect the wafer surface during the etching of the two sets of columns from the same side and double-metal technology is necessary to create the crossed-strips net for the X-Y projective readout. In this section both technological challenges will be discussed along with the approaches used to face them.

4.3.1 Dual-column electrodes

The electrodes fabrication starts with etching deep holes in the substrate using Inductively Coupled Plasma (ICP) etching. SF_6 is injected in an ICP chamber. When an RF current flows into the inductive coils outside the chamber, it generates a changing magnetic field, which in turn generates a changing electric field through inductive coupling. The inductive coupled electric field accelerates electrons and causes ionization collisions creating high-density plasma at low pressure. Fluorine ions and radicals can

Table 4.2: *Mask levels for the stripixel fabrication run carried out at the IMB-CNM clean room facilities.*

Level	Pattern	Comments
P-DIFF	p-stop	p-stop rings definition around n-type columns
N-HOLES	n^+ columns	n^+ columns etching
POLY	polysilicon	definition of the n^+ columns on the surface
P-HOLES	p^+ columns	p^+ columns etching
POLY2	polysilicon	definition of the p^+ columns on the surface
WINDOW	metal window	removing SiO_2 on the guard ring columns
		and p-type columns to contact with the metal layer
METAL	metal (first layer)	first metal layer pattern definition
VIA	metal2 window	opening connection between two metal layers
		and removing SiO_2 on the p-type columns
METAL2	metal (second layer)	second metal layer pattern definition
PASSIV	metal contacts	opening windows on the metal connection pads
BACK WINDOW	SOI wafer	etching the support substrate up to SOI wafers

then be accelerated onto the wafer surface, where they react quickly with silicon and etch it; the etch product is SiF_4. One of the most important advantages of ICP system is that the ion bombardment flux and ion bombardment energy can be independently controlled by the source power and bias RF power, respectively. Then, low pressure of the system translates into longer ions main free path and less ion collision scattering, that enhances etch profile control. Nevertheless, going on etching the columns through the mask pattern (levels N-HOLES and P-HOLES in table 4.2), unreacted fluorine will accumulate and etch away the sides of the holes. To avoid this, periodically during the process the SF_6 is pumped out of the chamber and C_4F_8 is injected and ionized to create a polymer chain of CF_2 which is deposited on the substrate. This polymer protects the sides of the holes from chemical etching during the next etching step. The sequence of steps go on up to the desired depth of the column; endpoint of the process is determined by time, which has been previously calibrated. Ideally, the holes

should be very narrow, so that the total volume (inactive volume) occupied by the columns in the sensor is small. In practice, there are limits on how deep a hole of a given diameter can be etched, i.e. on how narrow a hole of a given depth can be. For example, with current etching machines 10μm-diameter holes cannot be etched much deeper than 250μm. So, this is the depth of the columns sets in our process. For what concern SOI wafers, they are characterized by a thin bulk (20 μm in this case) bonded on an insulator layer, so in this case, the columns are etched through all the bulk, up to the SiO_2 surface. The mask used during the deep etching is obtained depositing a metal layer over a SiO_2 or TEOS film. Before polysilicon deposition, the metal layer is etched. As explained in section 2.4.5, polysilicon is deposited by means of a LPCVD process. In this case 0.5 μm have been deposited to fill the n-type columns following the standard 3D technology developed at the IMB-CNM [17]: the columns were not completely filled. The columns have been finally doped through the polysilicon by diffusion from a solid source of B_2H_6 or a gas sourse of $POCl_3$ for p-type or n-type doping respectively and a thin layer of SiO_2 was used to passivate the polysilicon surface. Figure 4.9(a), shows SEM images of a set of columns produced at IMB-CNM with this method [17]. In figure 4.9 (b), a detail of a p-type column of a stripixel detector processed on a SOI wafer is shown. The wafer was treated with a tetramethylammonium hydroxide (TMAH) solution to etch the support substrate in the back side through the pattern defined by the last level of the mask (back window). Due to infiltrations through the passivation layer polysilicon and metal coating have been etched too, along with silicon substrate around the column. Silicon etch rate is higher along the $<111>$ crystal direction, causing the diamond etch profile shown in the figure. Silicon nitride has a negligible etch rate in TMAH and the etch rate for silicon dioxide is three order of magnitude lower than for silicon. So, just the dielectric coats survive to the etch process: passivation layers (SiO_2 and Si_3N_4), SiO_2 grown on the substrate to isolate columns to each others and the thin layer of SiO_2 used to passivate the polysilicon surface inside the columns. Shaded arrows point at the vacancies left by the materials etched.

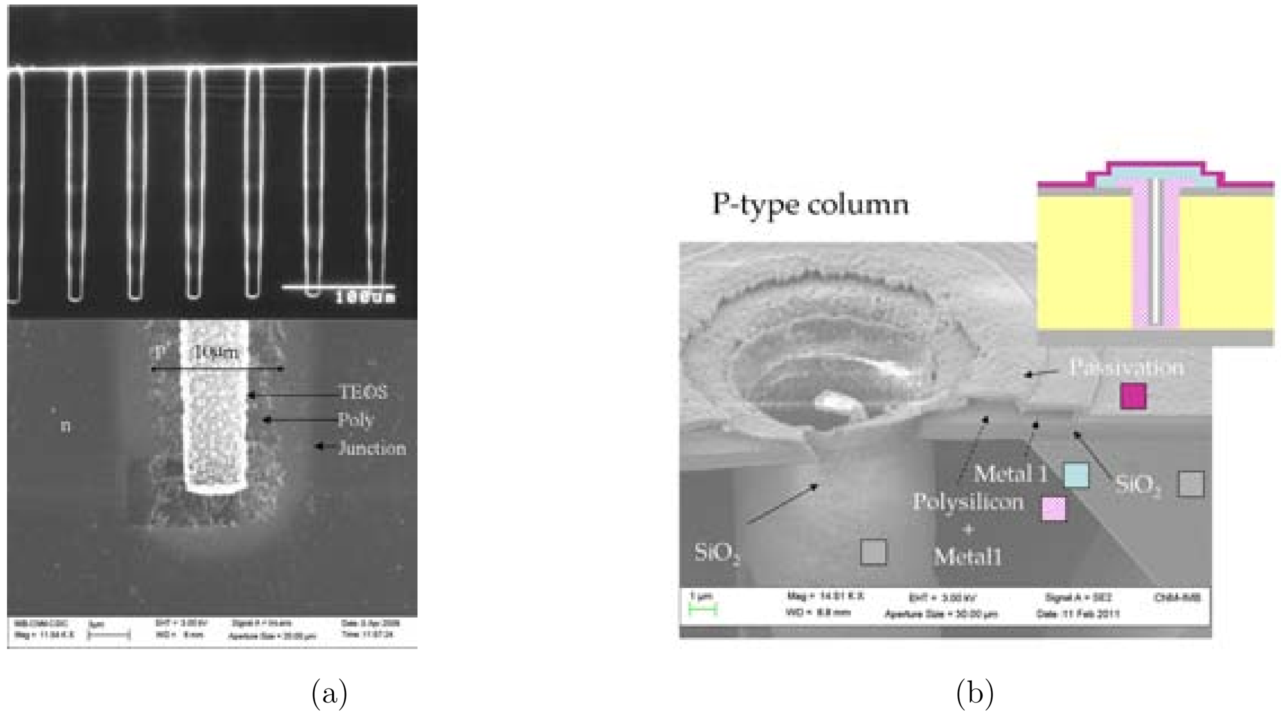

(a) (b)

Figure 4.9: *(a) SEM image of etched holes in a silicon substrate (top figure) and SEM image showing details of a filled and doped p-column. The brigther zone around the polysilicon reperesents the region where dopant atoms diffused thill the junction. Images refer to structures fabricated in 2008 by Pellegrini [17]. (b) SEM image of a detail of a p-type column of a stripixel detector after TMAH etch.*

4.3.2 Double metal deposition

Double-metal technology has been used in order to provide X-Y projective readout. The same Al/Cu alloy introduced in section 2.4.2 has been used in this case too. It has been sputtered on the chips surface and etched by plasma to define the strip profiles in different steps. The aluminium etcher uses Cl_2 as the main etchant, and BCl_3 for the sidewall passivation in order to obtain an anisotropic etch profile. In the plasma, chlorine dissociates and generates Cl free radicals, which can react to Aluminium and form volatile by-products $AlCl_3$.

Between the two metal layers, 500 nm of SiO_2 has been deposited in order to electrically isolate the X-strips from the Y-strips. Considering the strips are 10 μm wide, the resultant capacitance between two crossed strips is about $6{\times}10^{-3}$ pF, that should be sufficiently small to ensure a good isolation. A superposition of the two metal layers have been realized in selected regions in order to provide external metal pads

to the columns connected by the first metal layer for the connection to the readout electronics and biasing. The first metal layer actually has the function to connect both the p-type columns (the last ones processed) in parallel strips and the n-type columns of the guard ring in a squared arrangement. The second layer is then dedicated to the connection of the n-type columns and the pads definition for the electric contacts. Figure 4.10 shows a detail of the surface of a stripixel detector: the elements generated with the two metal layers are visible.

The sequence of processes involved in the metal strips formation is summarized in figures 4.11 and 4.12, where it is shown a vertical cross section of the device in the region defined by the red shaded line in figure 4.10.

The first metal layer has the function of connecting both the p-type columns (the last ones processed) in parallel strips and the n-type columns of the guard ring in a squared arrangement. The guard ring columns were protected during the p-type columns definition by a thermal dioxide layer plus the metal mask. After etching the

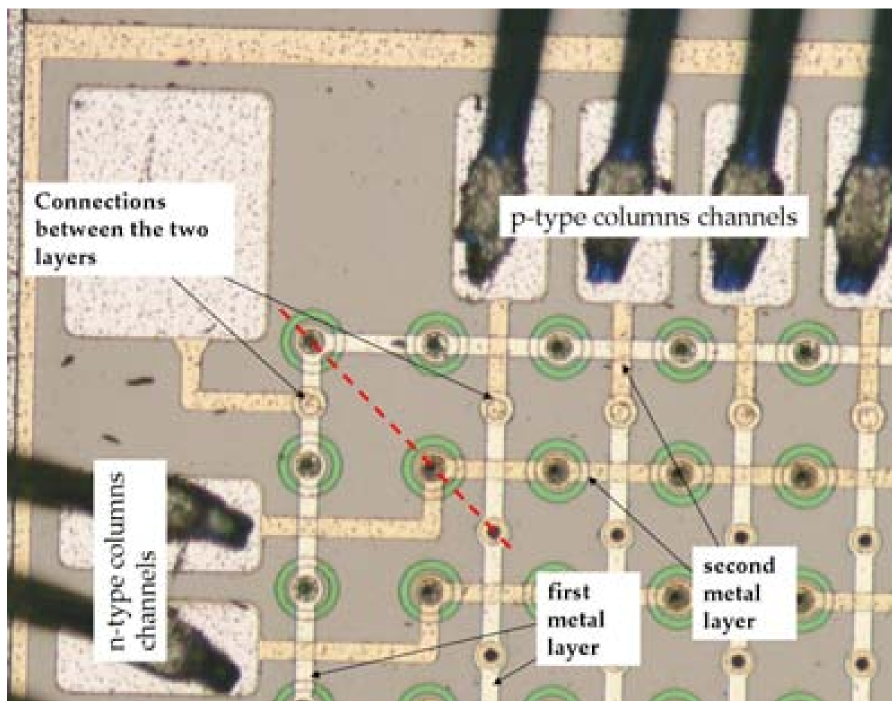

Figure 4.10: *Detail of the front surface of a stripixel detector. A corner of the active area surrounded by the guard ring is considered. In addition to the metal strips for the X-Y projective readout and the guard ring, the pads for the connections with the electronics are shown, along with the bonded wire. The red shaded line define the position of the vertical cross section object of figures 4.11 and 4.12.*

aluminium layer, SiO_2 underneath has been opened by a wet etch process through the WINDOW mask patterns (figure 4.11(b) and (c)) as well as the native oxide has been removed from the p-type columns surface. Then, the aluminium alloy with copper has

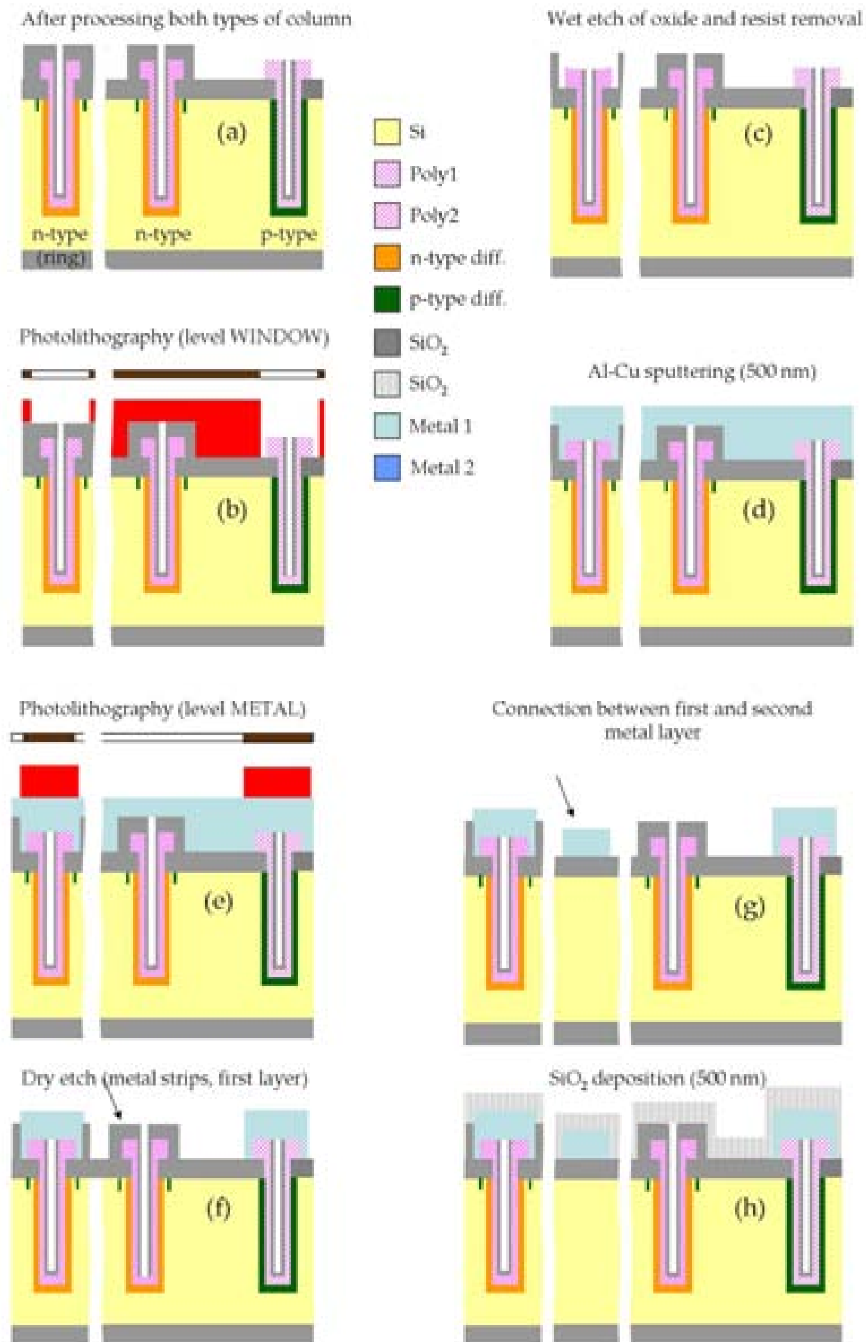

Figure 4.11: *First steps of the metallization processes. Drawing not to scale.*

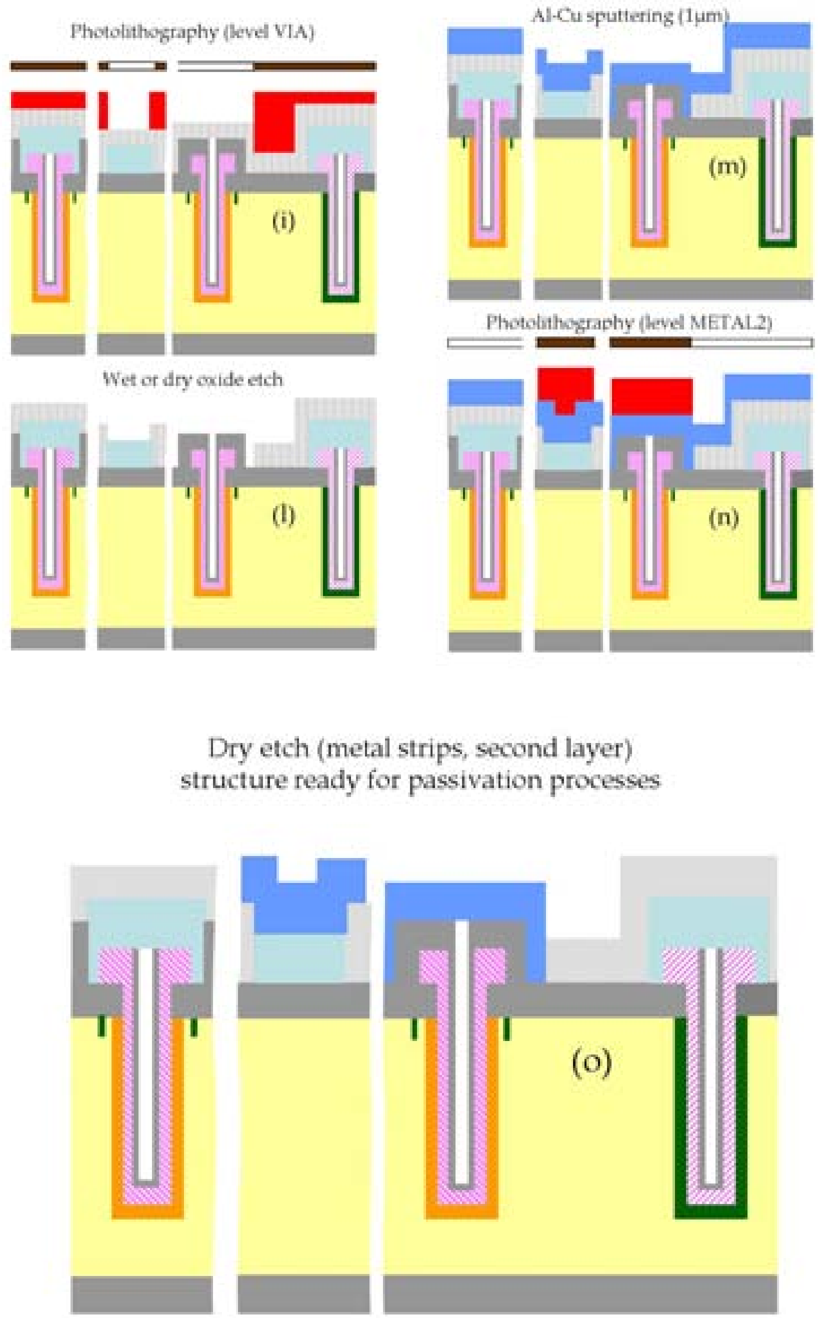

Figure 4.12: *Final steps of the metallization processes. Drawing not to scale.*

been deposited to form a layer 500 nm thick (figure 4.11(d)). Then, a photolithography (figure 4.11(e), mask level METAL) and a dry etch (figure 4.11(f)) processes have been used to define the strips and guard ring shape. From figure 4.11(g) the cross section

considered includes one of the regions where the two metal layers are superposed.

The metal lines defined by the first metal layer have been covered by a SiO_2 layer 500 nm thick (figure 4.11(h)) on which a photolithography (figure 4.12(i)) and a wet (or dry) etch (figure 4.12(l)) processes have been carried out to open vias in correspondence to the n-type columns and the strips regions dedicated to the two metal layer superposition. Then the second metal layer is deposited (figure 4.12(m)). Finally other photolithography (figure 4.12(n)) and dry etch (figure 4.12(o)) processes are used to define the n-type columns strips and the pads for the contacts with the electronics. Along all the fabrication run, the back surface of the detectors is passivated by a SiO_2 layer 800 nm thick, thermally grown in the first steps before p-stop definition. As well as for the other detectors fabricated and studied along this thesis work, the front side of the stripixel detectors has been passivated with a standard layer of silicon nitride deposited on a silicon dioxide layer. A detail of the final device can be seen in figure 4.10, where the two sets of readout strips are connected to the electronics channels by wires bonded to the contact pads, where the passivation layers have been removed. The finished wafer is presented in figure 4.13.

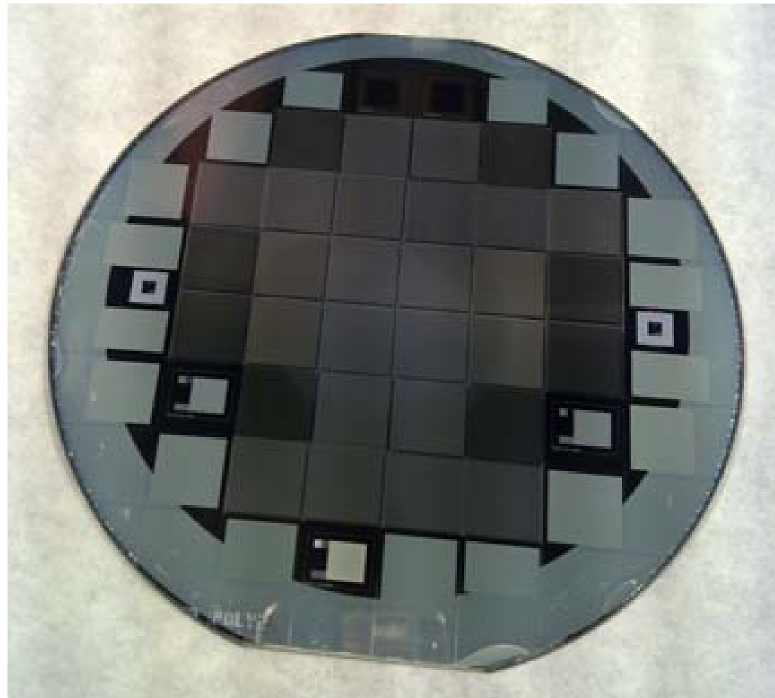

Figure 4.13: *Finished wafer of stripixel detectors.*

4.3.3 Fabrication process monitoring

In such an elaborate processes flow there are many delicate steps, that can determine the good quality of the whole run: photolithography is one of the most important. It transfers the design layout from the mask to the photoresist and then to the wafer, by either etch or implantation through the pattern defined on the photoresist. A precise alignment between different levels of the mask is important in order to guarantee high quality of the device. Nevertheless, especially for what concern the etching process, defects on the protection mask can cause serious failure, creating undesirable patterns on the photo resist and as a consequence undesirable effects on the wafer surface.

The experience had with this processes run, highlights the damaging effects of defects on the aluminium mask deposited before a deep etch process. As explained in section 4.3.1, two consecutive deep etch processes have been carried out in order to separately create the n-type and p-type electrodes. During the deep etch used to open the p-type columns the hard mask used to protect the rest of the device broke in many places, in correspondence of some aluminium defects. It occurred especially on the n-type columns surface causing the overetching of some of them down to the back surface of the wafer (SEM image on the left of figure 4.14) and causing regions of indiscriminate etching (microscope pictures on the right of figure 4.14). As a consequence the next steps of the fabrication process, i.e. deposition and doping (Boron) of the polysilicon, involved all the affected regions. These puntual (one column) or clustered defects affect the working status of the devices, especially for what concern the test structures, in which many strips of columns are shorted together (see next section).

The same defects on the aluminium mask have been observed in a later fabrication run of 3D detectors: a careful monitoring of the wafers surface and a precise cleaning of the identified defects allowed to avoid the above effects.

Similar defects on the passivation layer of a SOI wafer (wafer 8) caused infiltrations of TMAH into the columns and into the bulk during a deep etch process with destructive effects as reported in section 4.3.1.

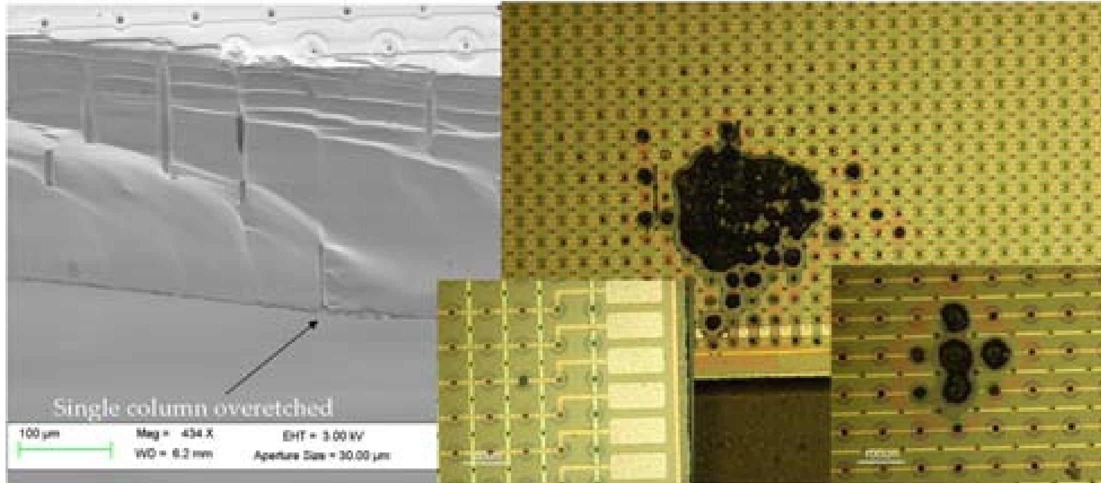

Figure 4.14: *Consequence of some defect on the aluminium protective mask during the deep etch of the p-type columns. The SEM image on the left shows a n-type column overetched down to the back side of the wafer, while the microscope pictures on the right show the defect effects on the surface of different devices.*

4.4 Electrical characterization

The detectors have been electrically characterized in the IMB-CNM laboratories with the use of the same instrumentation presented in section 2.5. Unlike planar strip detectors, stripixel detectors do not have any bias ring connection, so each strip have to be biased (grounded) and read separately. Many test structures have been included in the mask design with the purpose of shorting one set of strip (p- or n-type) or both separately in order to better investigate the electrical behaviour of the sensors. Unfortunately, most of these devices have been affected by the problems explained in section 4.3.3 and resulted useless for the electrical characterization. Just a few samples have a breakdown voltage higher than the depletion voltage and have been mainly used to study the capacitance between different set of electrodes. Figure 4.15 (a) displays the C-V characteristic of some samples. Apart from the diodes, in which all the n-type electrodes are shorted together as well as all the p-type electrodes, in the other structures the capacitance between all the n-type strips and just one p-type strip was measured. All the samples have 80 μm pitch. Considering the values for $V_{bias} = 12$ V, the samples with columns 20 μm deep (SOI wafer) and parallel strips has a capacitance 4 times lower than the same structure with columns 250 μm deep (wafer 300 μm thick

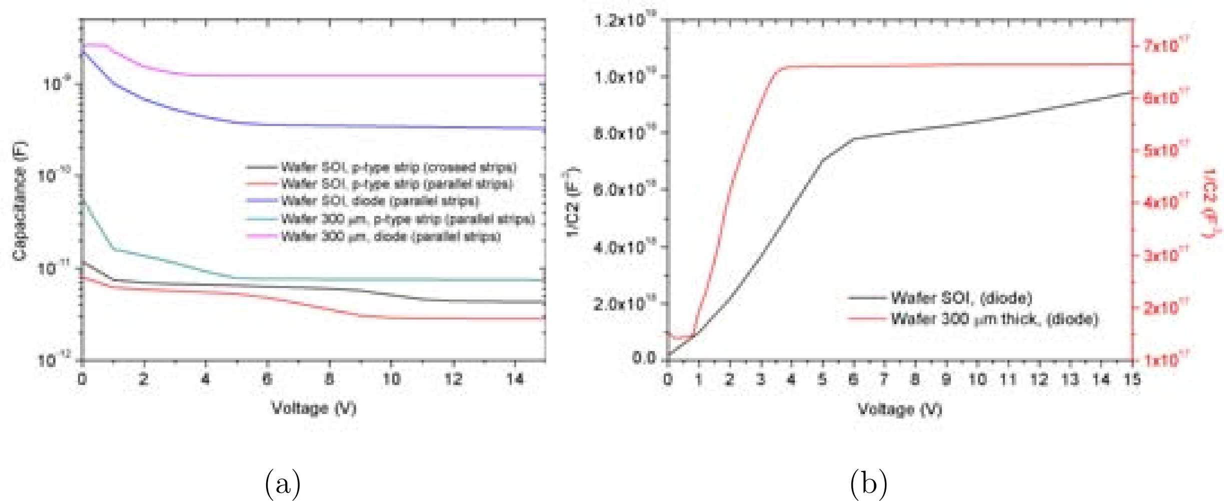

(a) (b)

Figure 4.15: *(a) C-V characteristic of different structures. See text for details. (b) 1/C^2 dependence to the bias voltage for two diodes, one from each type of wafer. The wafers have different resistivity.*

and parallel strips), but only 2 times lower than the structures from the same wafer and crossed strips. The values are in the range between 2 and 8 pF. The values of the interstrip capacitance, i.e. the capacitance between one p-type strip and both its first neighbour strips have been measured on the same samples. The result obtained for the detectors from the wafer SOI is independent of the parallel or crossed configuration of the strips and takes a value of about 0.15 pF for $V_{bias} = 12$ V. The interstrip capacitance of the sample with the columns 250 μm deep, is 0.8 pF at the same voltage value.

The diode from the wafer SOI has a bulk capacitance of about 0.3 nF, while the diode from the wafer 300 μm thick of 1.2 nF. Figure 4.15 (b) shows the classic 1/C^2 dependence to the bias voltage for both diodes. It can be noticed that the depletion voltage of the detector from the wafer 300 μm thick and resistivity in the range 5-7 kΩ·cm is $3V < V_{depl} < 4V$ as expected from the simulation results, while the depletion voltage of the diode from the SOI wafer 20 μm thick and resistivity >1 kΩ·cm, is $5V < V_{depl} < 6V$. In both cases the distance between electrodes with different doping is $d = \text{pitch} \times \sqrt{2} \approx 56.6$ μm.

The results of the I-V characteristic measurements are shown in figures 4.16 (a) for detectors 300 μm thick and (b) for detectors 20 μm thick. A current of about 10 nA has been recorded from the detectors with columns 250 μm deep, when just one p-type strip

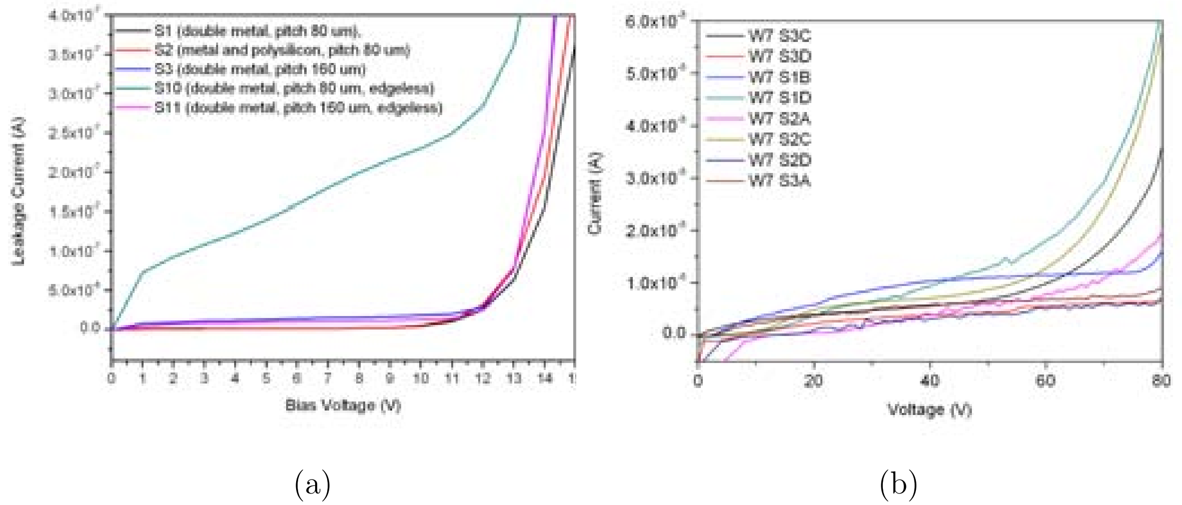

(a) (b)

Figure 4.16: *(a) I-V characteristic of every detectors type included in the wafer. Measurements refer to the particular condition in which just one p-type strip has been biased and one n-type strip has been grounded and read. (b) I-V characteristic of some detectors from a SOI wafer.*

was biased and one perpendicular n-type strip was grounded and read. Measurements on test structures with all the n-type strips shorted together give a value 10 times higher.

In the detectors from SOI wafer, columns are only 20 μm deep and they are processed through all the substrate thickness up to the SiO_2 layer. This forbids to isolate the n-type columns from each other at this silicon/oxide interface. So, all the detectors processed on this wafer are strip detectors 1D position sensitive. In this case, the leakage current is less than 10 nA. More relevant is the fact that for these detectors the breakdown voltage is noticeably higher than for the 300 μm thick detectors. This wafer, actually, has been damaged in a minor portion during the deep etch of p-type columns.

Two samples among all have been chosen for a deeper investigation of the stripixel detectors characteristics and their capability as 2D position sensitive detectors. The studies carried out are presented in the next sections.

4.5 TCT measurements

As introduced in section 4.2.1, processing the two types of column on one side of the bulk 300 μm thick, lead to a non-uniform distribution of the electric field strength in the bottom of the wafer, characterized by lower values in the regions under the n-type columns. Then, for $V_{bias} \leq 15$V, the last 5 μm close to the silicon/SiO_2 interface do not deplete. In order to investigate the effect of the Space Charge Region (SCR) extension and of the electric field distribution on the charge collection of the device, a sample with parallel strips (pitch = 80 μm) and all the n-type columns shorted together (sensor type, TS6) has been electrically characterized using a laser Transient Current Technique (TCT) with different lasers of different wavelengths. In this section the results of this investigation are presented and discussed.

4.5.1 TCT set-up and experimental technique

TCT is based on the analysis of the current pulse shapes which arise from the drift process of non-equilibrium carriers in the electric field region inside the detector bulk. A schematics of the laser TCT set-up at Brookhaven National Laboratory (BNL) is shown in figure 4.17 (a). The sample can be placed on a copper support and can be

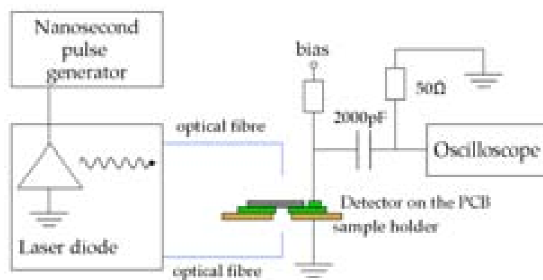

(a) (b)

Figure 4.17: *(a) Schematic of the TCT set-up at Brookhaven National Laboratory (BNL). (b) Detector mounted on the detector board.*

AC coupled with an high frequency oscilloscope TDS-445 (Textronix) by a thin coaxial cable. Non equilibrium carriers can be generated by lasers of different wavelengths:

the light beam, driven by an optical fibre, can impinge directly on the front or on the back surface passing across an hole through the copper support. Details of the set-up can be find in references [85], [86], [87].

With this set-up it is possible to analyse detector waveforms of current pulses with amplitudes of the order of the mV. It is prepared for pad detectors characterization, grounded from the back side and biased and readout from the front side. For this reason a special detector board has been designed, on which all the p-type strips are connected together to one contact pad and the n-type to another. Then, one of the pad can be connected to a metal contact on the back side of the board. In this way all the electrodes of the same type can be grounded or biased and readout together. A picture of the detector mounted on the board is shown in figure 4.17 (b).

Three different lasers of different wavelengths have been used to generate non equilibrium carriers inside the detector bulk. The diameter of the beam spot on the detector was 1 mm. The laser was pumped by nanosecond current pulses from a pulse generator through a current amplifier. The different penetration depth of each laser permitted to study the carrier generation and collection along all the bulk thickness as well as selectively close to the front and back surface of the detector. Characteristics of the three lasers and their operation specifications are listed in table 4.3.

Table 4.3: *Laser characteristics and their operation specifications.*

Wavelength (λ) (nm)	Intensity (V)	Width (ns)	Period (μs)	Penetartion depth (20°) (μm)
1060	10	10	20	whole thickness
830	10	10	20	15
660	10	10	20	5

The depletion voltage of the detector extrapolated by its C-V characteristic was 3.5 V and the I-V characteristic, for the pad configuration of the electrodes (1×1 cm^2 area), showed an increasing leakage current, higher than 20 μA after the depletion voltage. For this reason measurements have been restricted to a V_{bias} range of 15 V, starting from 0V and an high intensity (10V) and large width (10 ns) of the laser pulse were set. Measurements have been performed at room temperature.

4.5.2 Measurements results

The current pulse shapes generated by the three lasers, impinging on the front side of the detector, have been recorded from both the n- and p-type pads, at many stages of a voltage ramp from 0 V to ±15 V. The shape of the signal arise from the simultaneous drifting of electrons and holes in the electric field between the columns, following different paths depending on where they are generated. Due to the wide spot of the laser beam (≈20 times the distance between columns) the carriers are created homogeneously all around a big number of columns and they start moving towards the electrodes with different velocities depending on the electric field strength. Then, the large width of the laser pulse cause superposition of the motion of carriers generated during a large time lapse. However, being the electron mobility about 3 times the mobility of the hole, the rise time of the current pulse read can be considered dominated by the electrons drift, while the tail by the holes drift. The integral of the current pulse over the time represent the total charge collected by the electrodes.

The shapes of the signals read from the n-type electrode (left) and from the p-type electrodes (right) are shown in figure 4.18 for all the laser wavelengths. The pulse amplitude depends on the absorption coefficient of light in silicon, that depends on the wavelength of the laser: the higher the wavelength, the lower the absorption coefficient, i.e. the lower the pulse intensity. It also depends on the temperature at which the measurements were carried out. All the measurements were done at room temperature, without any stabilizer system, during two different days, so the lower amplitude of the signals readout from the p-type electrodes, can be due to a different temperature of the laboratory. In all the cases the amplitude of the current pulse increases rapidly with the bias voltage up to 3 V and then slowly after 4 V, while the rise time decreases. The device simulation reveals that the lateral depletion occurs for a bias voltage close to 4 V. The SCR extends below the columns while voltage increases, almost reaching the silicon/silicon dioxide interface: only the last 5 μm do not deplete in the V_{bias} range considered. Then, close to the silicon/silicon dioxide surface, regions of low electric field extend in proximity of the p-stop rings. Figure 4.19 shows the values of the pulses amplitude, normalised to the value taken at 12V as a function of the bias voltage applied for both the reading configurations and for each laser wavelength. The general trend seams to be independent of the laser wavelength,

i.e. of the penetration depth inside the bulk; we can deduce that the lateral depletion of the sensor predominates over any other trend in the region beneath the columns.

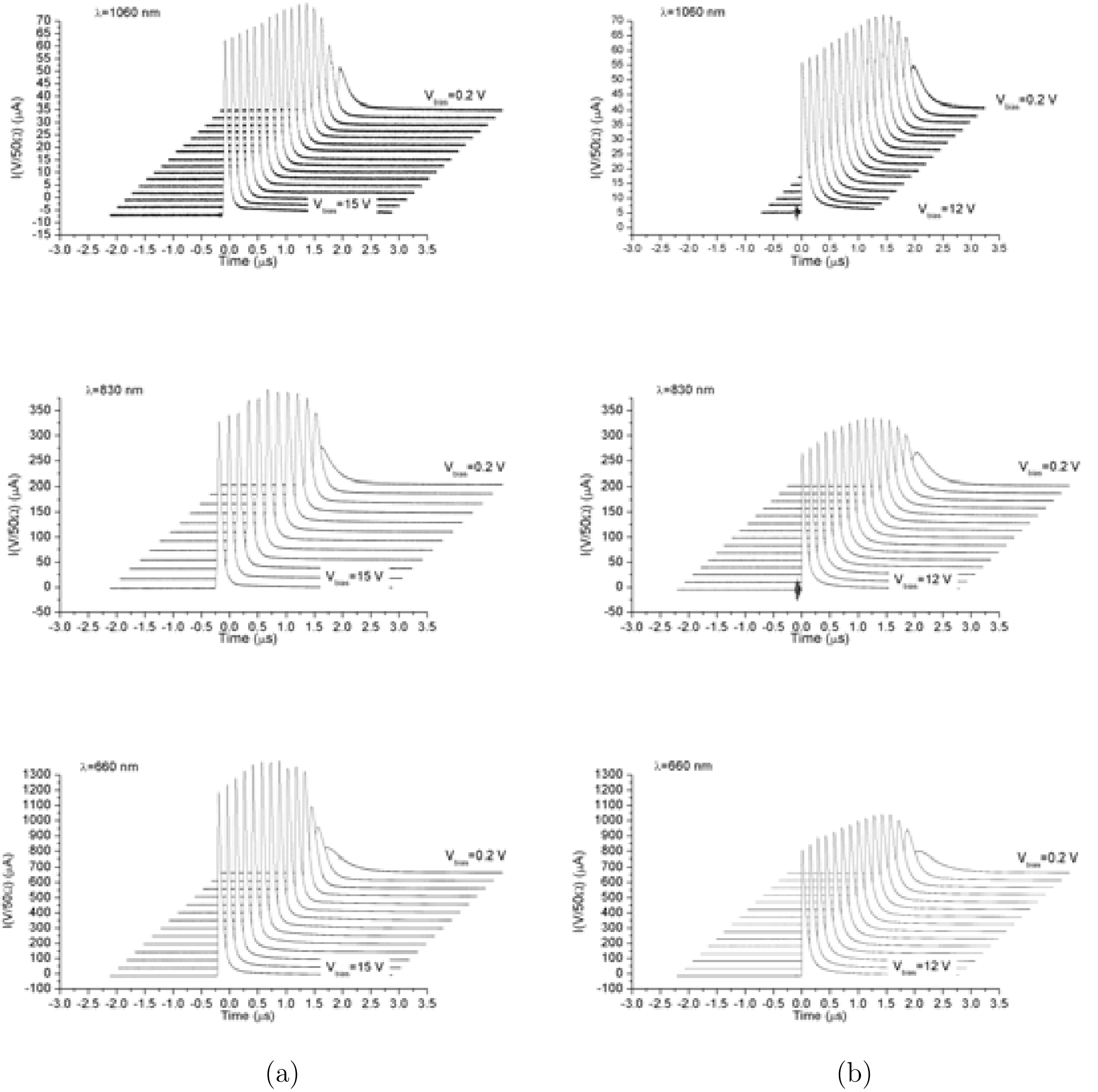

Figure 4.18: *(a) Shape of the signals read from the n-type (a) and the p-type (b) electrode for different values of the* V_{bias} *and for all the laser wavelengths.*

In the same plots, the normalized values of the current integrated over the time, i.e. the total charge collected, are shown. Laser fluctuations avoid a clear analysis based

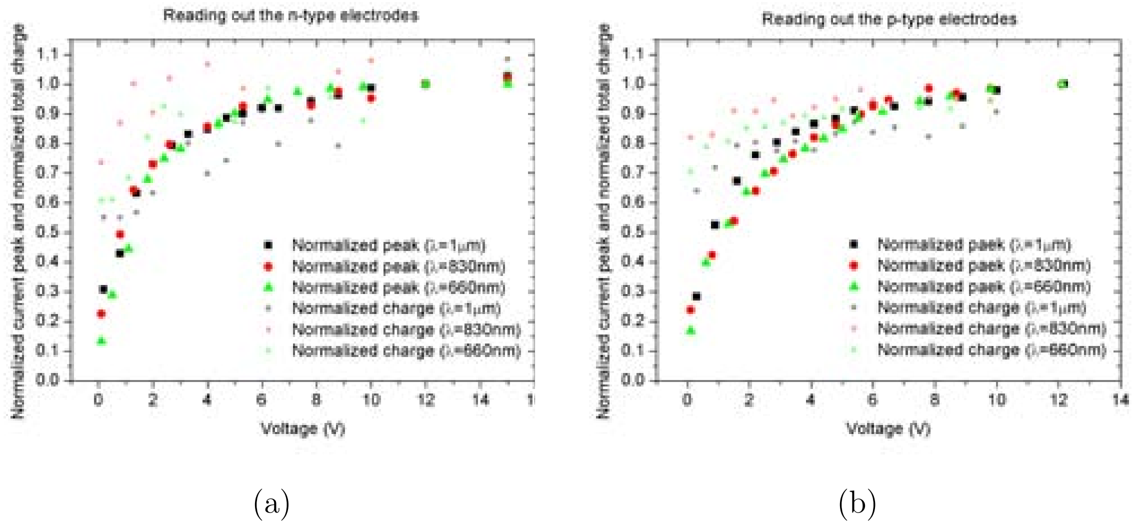

(a) (b)

Figure 4.19: *Value of the pulses amplitude, normalised to the value at 12V, as a function of the bias voltage applied for both the reading configurations ((a)n-type electrodes and (b) p-type electrodes) and for each laser wavelength. The smaller empty marks related to the normalized value of the pulse integral (total charge)*

on this parameter, but in general, the total collected charge increase with voltage. In figure 4.20 the Full Width at Half Maximum of the pulses, related to the average drift

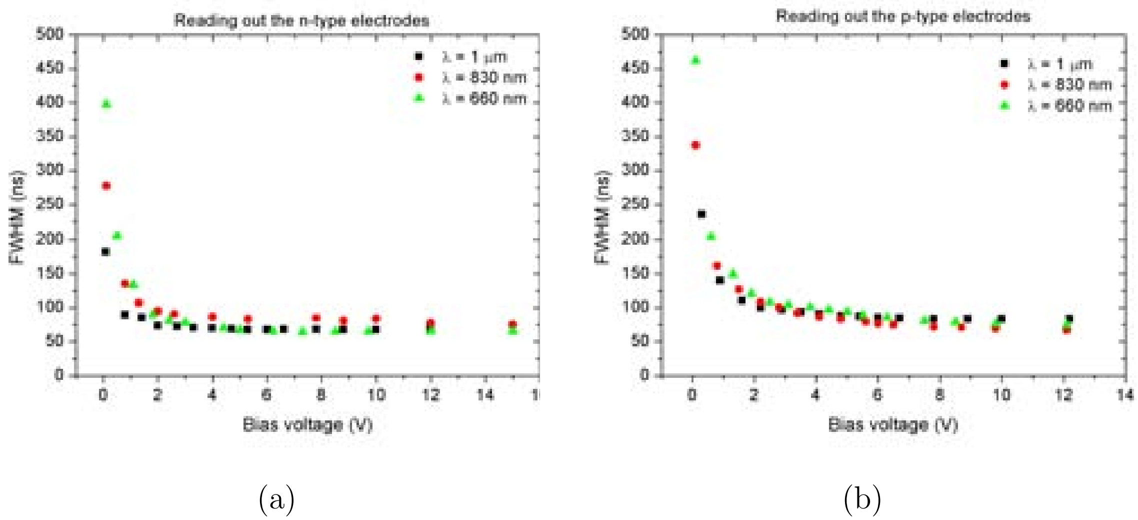

(a) (b)

Figure 4.20: *Value of the pulses FWHM, normalised to the value at 12V, as a function of the bias voltage applied for both the reading configurations ((a) n-type electrodes and (b) p-type electrodes) and for each laser wavelength.*

time of all the carriers, are shown for both reading configurations. Again, the curves show a trend independent of the laser wavelength.

In order to investigate the region under the columns, the same measurements have been repeated driving the light of the laser through an optical fibre to the back surface of the detector. Using both the laser with λ=660 nm and λ=830 nm, no signal could be read, neither for the highest value of the bias voltage (15 V). From table 4.3 we know the two wavelength correspond to a penetration length of 5 and 15 μm respectively. Simulations with Sentaurus TCAD showed that the last 5 microns of the bulk do not deplete when a voltage lower than or equal to 15 V is applied. Going deeper into the bulk up to 15 μm, the region result to be characterised by a low electric field strength expecially under the n-type columns (see figure4.21 (a)). This can affects carriers transport to the electrodes introducing a delay not recorded by the oscilloscope.

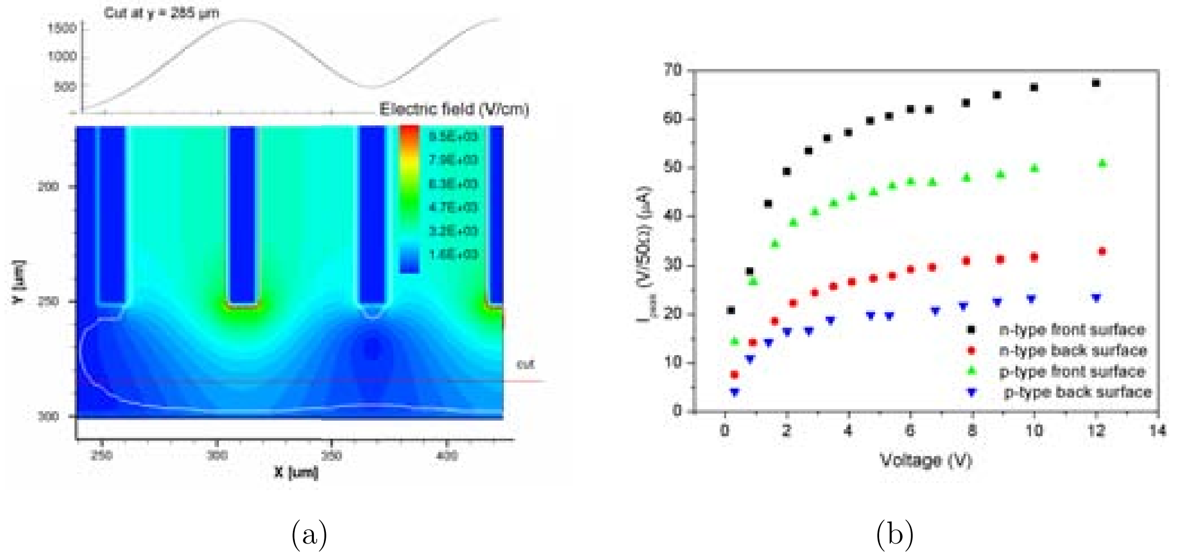

Figure 4.21: *(a) Detail of the simulated (2D) electric field distribution in the bulk zone below the columns of the active area, when a bias of 12V is applied. The white outline define the SCR. The plot on the top display the electric field strength along the cut defined by the red line, 15 μm inside the bulk from the silicon/silicon dioxide interface. (b) Pulse amplitude for both reading configurations as a function of the bias voltage. The values obtained when the laser with λ=1 μm enter from the back surface are compared with the values obtained when the laser enter from the front surface.*

Using the laser of λ=1060 nm, a current pulse can be obtained for both the reading configurations. The pulses amplitude results in both cases attenuated with respect to the pulses read when the laser penetrates from the front surface. Considering the value

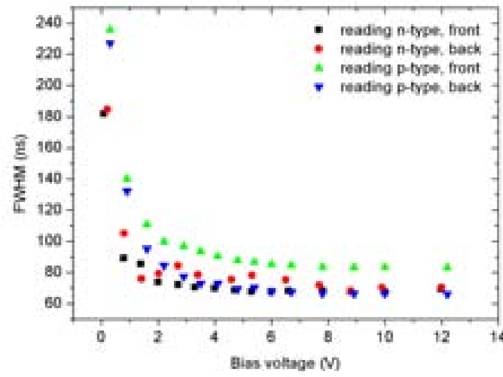

Figure 4.22: *Pulse FWHM for both reading configurations as a function of the bias voltage. The values obtained when the laser with λ=1 μm enter from the back surface are compared with the values obtained when the laser enter from the front surface.*

at V_{bias} = 12V, the attenuation can be quantify as by 51% and 54% for the signal read from the n- and the p-type electrodes respectively. This effect has different reasons. Let us start considering the Beer s law: $I = I_0 e^{-\alpha x}$, that expresses the dependency of the beam intensity, travelling through a material, on the initial intensity value (I_0), the absorption coefficient (α) and the distance covered (x). The use of the short wavelength lasers reveals that no readable signal is produced in the first 15 μm from the detector back surface. Suppose that the active area of the detector extends along the rest of the bulk thickness. So, when the laser penetrates into the silicon from the front surface it reaches the inactive area after crossing 285 μm. That means it will lose just a little portion of its energy in the inactive zone. On the other hand, when the laser enter into the silicon from the back surface, at first it crosses the inactive area, reaching the active one more attenuated. A simple calculation considering α = 20 cm^{-1} [88], gives that the attenuation of the laser, hence of the energy absorbed in the active area, is 3 % when the laser enters from the back surface[2]. More decisive is the effect due to the different optical fibres into which the laser light propagates before to impinge on the detector surfaces: the longer fibre that drives the light to the back surface attenuates

[2]In the text, we consider the active area of the detector extends to all the bulk thickness apart the last 15 μm beneath the coplumns. On the contary, if we suppose that the inactive area extends from the back surface to the base of the columns, a total thickness of 50 μm, the attenuation of the laser intensity, when crossing the whole bulk from the back surface, will be close to 10%.

approximately the laser light by a 50%.

Measurements results are shown in figure 4.21 (b). Comparing the FWHM of the pulses, as expected, it results practically independent of the surface from which the laser enters.

4.6 2D position sensitivity and spatial resolution

In order to study the 2D position sensitivity of the new stripixel detector, a simple (5 points) scan of a pixel has been performed using the same laser setup presented in section 3.3 and the ALIBAVA DAQ system. Again, a special detector board has been designed to adapt the detector geometry to the readout electronics. In this case, the 127 p-type strips have been DC coupled to 127 channels of one Beetle chip, while two sets of 10 consecutive n-type strips have been AC coupled to the same number of channels of the other Beetle chip through a capacitor of 2 pF, and biased (10 V) through a resistor with R = 1MΩ. The other n-type strips have been all bounded[3] to a common bias pad and connected to the same bias circuit through a proper resistor.

The sample bounded to the board was a 2D detector 300 μm thick, with pitch of 80 μm, crossed strips and doped polysilicon instead of the first metal layer (see section 4.2.2). A picture of the detector mounted on the board is shown in figure 4.23.

4.6.1 Laser characterization

At first, the laser beam has been positioned to impinge on the detector surface, approximately in the centre of the pixel defined by two consecutive n-type strips, among the ones biased and coupled with the readout channels, and two consecutive p-type strips. Then, it has been moved in other four positions within the pixel.

Due to the nature of the detector, the ALIBAVA DAQ system read out two signals for each position of the laser: a negative signal from the first Beetle chip (n-type strips) and a positive signal from the second Beetle chip (p-type strips). In a detector characterised by a double-metal connection of the strips, the two signals are supposed

[3]the wire bonding procedure has been carried out by the High Energy Physics group of the University of Liverpool.

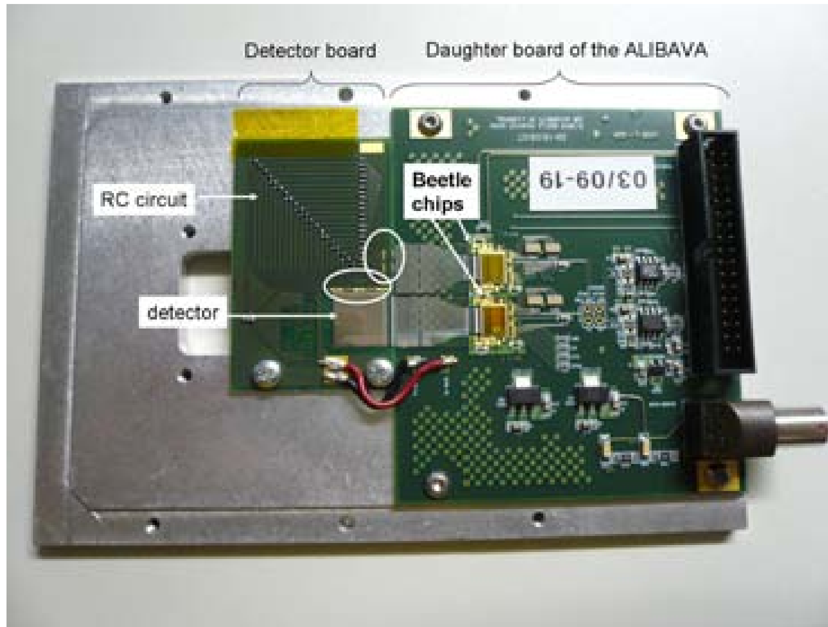

Figure 4.23: *Detector mounted on the dedicated detector board for the laser characterisation with the ALIBAVA DAQ system. The white circles highlight the connection of the two sets of 10 strips each one to the RC circuits and then to the Beetle chip.*

to arrive to the readout channels at the same time. Nevertheless, being this detector characterised by the p-type strips made of a resistive material, i.e. doped polysilicon (see chapter 3), a time delay is expected to be observed for the signal read from these strips. The limited range of the scan positions along the p-strips direction (40 μm) is not enough to introduce an additional delay between signals created in different positions. Measurements revealed that the signal read from the p-type strips had always the same delay (30 ns) with respect to the signal read from the n-type strips. For this reason the procedure used to identify the signal peak described in section 3.3.2 is not necessary in this case, and just two measurements are enough for each position of the laser, each one for the value of the time delay in correspondence of a signal peak. The plot created by the Laser Synchronisation procedure of the ALIBAVA DAQ system is shown in figure 4.24: the average signal read is displayed as a function of the laser delay and the two peaks can be recognized.

For each measurement, 20000 events have been considered, recording the peak of both pulses. An example of the measurement result is shown in figure 4.25 for the first laser position P0.

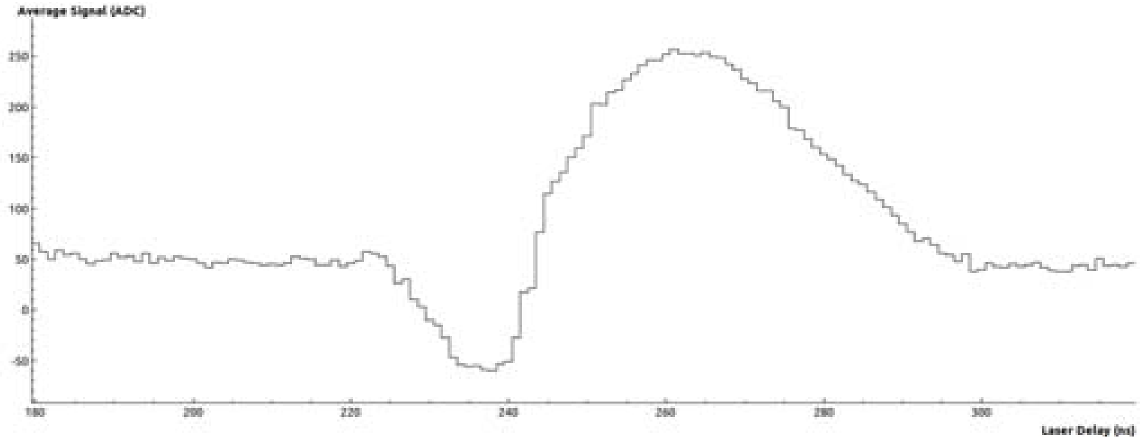

Figure 4.24: *Plot created by the Laser Synchronization procedure of the ALIBAVA DAQ system: the average signal read is displayed as a function of the laser delay. It is possible to recognize the negative signal read from the n-type strips centred around* $\tau = 235$ *ns and the positive signal read from the p-type strips, shifted in time (*$\tau = 265$ *ns) because of the resistive polysilicon strips.*

The signal read from the n-type strips is shown on the left (a) as a function of the channel number (chip 1). The same plot has been generated for the p-type strips (chip 2) (b). The n-type strips are bounded only to even channels of the first Beetle, while the p-type strips are bounded sequentially to all the channels of the second Beetle. From the plots it is clear that the laser beam impinges on a pixel within the detector surface, well defined by channels 64, 66 (n-type strips) and 185, 186 (p-type strips). The pixel area is 80×80 μm^2 but a better spatial resolution can be achieved thanks to the projective readout connections. Due to the 3D electrodes geometry, capacitive coupling between neighbour strips outside the pixel is practically negligible. Nevertheless, the charge generated by the laser beam through the detector is shared by the two couples of strips that defined the pixel, in a different portion depending on the position of the laser beam within the pixel area. Comparing the amplitudes of the signals read from channels 64 and 66, or from channels 185 and 186, the beam position can be reconstructed with a precision of pitch/$\sqrt{12} = 23$ μm in both the directions. In order to test this capability of the sensor, four measurements have been performed moving the laser beam 20 μm away from the central position in both directions parallel to the p-type strips (P1 and P2) and to the n-type strips (P3 and P4), drawing a cross centred in the first position P0 (see figure 4.26 (a)).

Results of the measurements are plotted in figure 4.26 (b) with the error bars and the

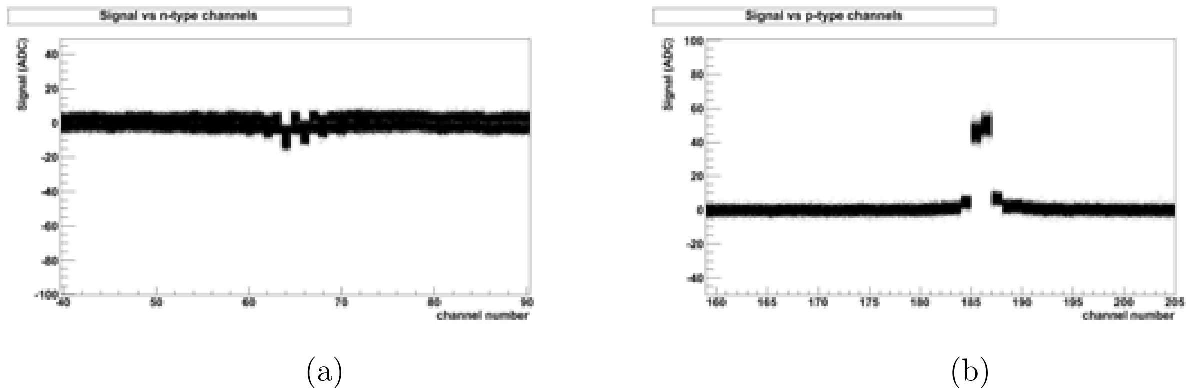

(a) (b)

Figure 4.25: *Measurement results: (a) Signal read from the n-type strips (zoom around the channels of interest. (b) Signal read from the p-type strips (zoom around the channels of interest).*

nominal position of the laser beam. The only result that does not include the expected value into its error bars is related to the measurement of position P2. Observing the schematics in figure 4.26 (a) and remembering what presented in chapter 2, the issue can be due to the orography of the detector surface in the zone of the p-stop ring, that can have cause a stronger refraction of the laser light changing its trajectory.

Finally, signals from the n-type strips results to be lower than the signals read from the p-type strips (figure 4.25). Due to the necessity of decoupling the high voltage supply from the readout chip, the n-type strips are AC coupled with the Beetle channels through a 2 pF capacitor. From the electrical characterization, we know that the capacitance of one strip to the bulk is of the same order, that can explain a loss of signal at the entrance of the readout electronics.

4.7 Summary and discussion

The study presented in this chapter represents the first experience in producing and characterizing dual-column 3D stripixel detectors. The stripixel concept was formulated and present by Z.Li almost 10 years ago, when he started investigating the possibility of obtaining a 2D position-sensitive device by a single-sided fabrication process (pixel detector), that could be coupled and readout with a moderate number of electronic channels (double-strips detector). At first, the idea was integrated in planar detectors by means of double-metal layer technology, then the interest in radiation-

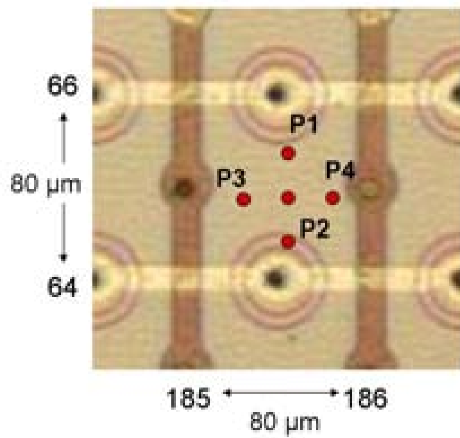

(a)

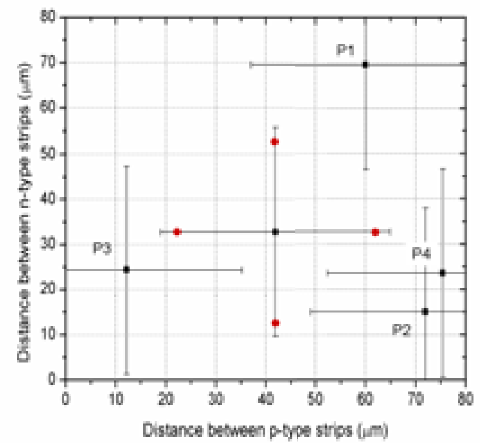

(b)

Figure 4.26: *Laser beam position within the pixel area 80×80 μm^2. (a) Schematics of the five position on a detector picture. (b) Sperimental reconstruction of the positions. The red circles indicated the nominal position of the laser, the black squares, the measured ones with the error bars.*

hardness and true single-sided processing moved the attention on 3D technology for the fabrication process of the electrodes.

The new device presented here is a dual-column 3D detector in which the p+ and n+ columns are both processed on one side of the wafer and arranged in a diamond pattern. Then, a net of perpendicular strips is defined on the surface by means of two different metal layers to allow a projective X-Y read out.

The final layout of the detector has been decided after a preliminary study of its behaviour by computer simulations. 2D and 3D models of a portion of the device has been developed using Synopsys TCAD Sentaurus, considering n-type or p-type bulk doping and different columns configurations. The results demonstrated that choosing an n-type doping for the bulk and the guard ring columns improves the guard ring isolation capability.

Then, the mask for the first prototypes fabrication has been designed including baby sensors with different geometries and many 1D position sensitive test structures. Following the hints of the simulation results, the devices were processed on a batch of 6 FZ n-type wafers 300 μm thick and 2 SOI wafers 20 μm thick. P-stop rings have been used to isolate the n-type columns to each other at the upper silicon/silicon dioxide

interface. Two metal layers have been used to contacts the electrodes and allow a projective X-Y read out on the detector surface.

The finished samples have been electrically characterized in the IMB-CNM laboratory finding that the depletion voltage is lower than 4 V and the leakage current measured between two strips of opposite doping assumes high values around 10 nA in detectors 300 μm thick.

A test structure with all the n-type strips shorted together as well as all the p-type strips, has been characterized using a laser Transient Current Technique with lasers of different wavelengths and penetration depths, in a range of voltages between 0V and 15V. The whole thickness of the bulk and the regions close to the silicon /oxide interfaces have been investigated confirming that the lateral depletion voltage is less than 4 V. Signals have been read from both n- and p-type strips. No signal is produced when the laser cross only the last 15 μm under the columns.

2D sensitivity has been tested by scanning the surface of a pixel with a laser and reading separately the strips crossing the interesting area. The ALIBAVA DAQ system was used to read out the sensor. Measurements have shown that the laser beam induces a signal only in two pairs of strips, the two p-type and two n-type strips that define the pixel area, almost without charge sharing outside the pixel. The position of the laser inside the pixel can be reconstructed with a resolution of pitch/$\sqrt{12} = 23$ μm in both the directions.

As mentioned in section 1.2.1, crossed readout strips with a 90° angle lead to multi-hit ambiguity at high hit density. This design has been chosen here in order to simplify the structures, focusing the attention on the double-columns and double-metal layer technologies. The investigation carried out demonstrates the feasibility of both technologies, however revealing the difficulties one has to face dealing with such complicated processes.

Nevertheless, small-angle stereo can be used in this structures as well as a different arrangement of the electrodes, like those proposed by Z.Li [77], can be designed in order to further improve the detector capabilities.

Chapter 5

Conclusions

The work presented in this thesis deals with the development of innovative technologies of silicon radiation detectors for future tracker systems. Three types of device have been studied and designed with the help of different tools for computer simulations (Spectre by Cadence and Sentaurus TCAD). They have been manufactured in the clean room facilities of IMB-CNM in Barcelona and characterized with proper experimental set-ups in order to test both the detectors capabilities and the quality and suitability of the technology used for their fabrication process.

In chapter 2 the upgrade of dedicated sensors for the laser alignment of future tracker systems has been presented. The layer composition of silicon trackers allows track reconstruction with a precision that depends both on the precision of the sensible elements involved and on the stability of the whole system. Considering the technological state of the art, stability can only be reached with a precise monitoring of reciprocal positions between sensible elements in different layers. A laser alignment system provides a solution without additional costs or mass to the system. Following the successful experiences of the AMS and CMS experiments, the design and technology of single-sided silicon microstrip p^+-in-n detectors have been slightly modified and monitored in order to improve IR light transmittance through the detectors volume. An optical model of the detector has been developed by the IFCA group of experimental physics in Santander and the passage of infra-red light through the sensor has been simulated, finding the geometrical and technological parameters that could boost light transmittance. The design and fabrication process of prototype baby sensors have been carried out at IMB-CNM of Barcelona respecting the hints of the simulation

study and the baseline pitch width of 50 μm fixed by the SiLC collaboration. The metal strip electrodes have been narrowed in order to meet the optimal width/pitch ratio ($\leq$ 10%) that enhance light transmittance without interfering with the diode structures (p^+ implants) of the sensors. A circular window has been opened in the back metal contact, to allow the laser beam passing through, towards the next sensor to be aligned. The fabriction process has been monitored in order to measure the thikness of the dielectric layers grown or deposited on the silicon surfaces and to perform optical measurements with the aim of further improving the simulation model of the detector and the predicted transmittance of laser light. The last passivation layer of silicon nitride deposited on both sides of the detector resulted to play a key rule as an Anti-Reflecting Coating.

The main goals reached by this project are:

- A maximum transmittance of 50% for metal-strip-width/pitch ratio of 6% and a peak value of 80% in unpatterned structures. Results are stable even after irradiation with 1 MeV neutrons at a fluence of 1×10^{15} n/cm^2.

- Uniformity of the optical characteristics, i.e. the technological parameters, within 6 wafers, each one populated by 12 sensors, is better than 5%, that ensure the possibility of large scale production of the detectors.

- The upgrade of the detectors has been carried out slightly changing the design and the standard technology of common silicon microstrip detectors, obtaining a similar simple and cheap device.

- An optical model of a real microstrip detector and the simulation of the passage of an IR laser beam through its active volume have been developed, obtaining coherent predictions of the measured transmittance in the real prototypes. The model is then validated as a powerful tool for possible future detector upgrade.

In chapter 3 a new 2D position sensitive detector has been presented based on the standard technology of single-sided AC coupled, silicon microstrip detectors in which resistive coupling electrodes have been integrated. The metal electrodes on each strip have been replaced with highly doped polysilicon strips and each electrode has been double read out. With this configuration, the resistive charge division method can

be applied to obtain spatial information on the coordinate of an ionizing event along the strip length. Optimal results can be achieved when using a readout electronics with optimal shaping time and electrodes resistance much higher than the preamplifier impedance, as reported by Radeka in 1984. The orthogonal coordinate can be obtained by using the usual cluster-finding algorithms for microstrip detectors. On the other hand, when a current signal travels along a resistive electrode (a diffusive RC line), it undergoes both an amplitude attenuation and an increase of the rise time the further it travels and the higher the resistance of the electrode. Amplitude attenuation allows to use the resistive charge division method, increasing rise time has to be taken into account when coupling the detector with a front-end electronics characterized by a finite integration constant and a short shaping time. Two prototypes of p^+-in-n detectors with strips 20 mm long and different electrode linear resistance (R/l=2.8 Ω/μm and 12.2 Ω/μm) have been studied and fabricated. In order to study the performance of the novel detector when coupled with a fast readout electronics, electrical models of the two prototypes equivalent circuits have been developed. The propagation of a current signal with initial rise time = 2ns has been simulated with Spectre by Cadence when the pulse generator is connected to different points along an implant length. Both ends of the coupled resistive electrode were connected each one to a charge preamplifier and an CR-RC shaper with shaping time of 25 ns. A systematic non constant ballistic deficit has been observed affecting the linearity of the sensor response: the effect increases for higher resistive electrode. The sensors have been fabricated processing the electrodes during the processes steps, and using the mask level, dedicated to the bias resistances definition. The electrode resistivity on each wafer has been defined by doping the polysilicon with different Boron concentrations. The real prototypes have been finally characterized at the IFCA clean room facility in Santander, performing a longitudinal scan of a strip with a collimated near infra-red laser. The sensors were read out with the ALIBAVA DAQ system, based on the Beetle ASIC, the front end chip developed for the tracking system of LHCb at CERN and characterized by a peaking time of 25 ns. Each side of the strips was connected to a readout chip. The results of the characterization demonstrate that the resistive charge division method is suitable for silicon microstrip detectors with resistive electrodes, although high resistance lead to the same non constant ballistic deficit foreseen by the simulation study.

The most relevant results of this first investigation are:

- 2D position sensitive silicon detectors based on the resistive charge division method can be obtained by means of the standard single-sided fabrication process of AC coupled microstrip detectors, simply designing the proper patterns in the mask levels dedicated to the bias resistor definition.

- Decoupling the restive electrode from the strip implants, the resistance value of the electrode can be opportunely selected in accordance with the electronic shaping time, without affecting the diode structure of the strip. The simple simulation model developed in this thesis, and validated by the experimental results, can be used for future optimization of these parameters.

- Spatial resolution along the strip length strictly depends on the S/N, that suffers the effects of the amplitude attenuation as well as of the internal and external noise sources. In the case of the two prototypes studied here, the achieved spatial resolution for a 6MIPs signal have been 1.1% and 1.2% of the total strip length for the detector with less and more resistive electrodes respectively.

The possibility of driving the wire bonding pads to the same edge of the detector, allowing the use of just one readout chip, has been also investigated running in the detection of undesirable induced signals in the metal lines composing the driving system. Specific studies on detection of minimum ionizing particles (irradiation at neutron facilities, beam tests) are in progress to assess its soundness as tracking technology for the future particle physics experiments, for the particular case of the external layers of the tracking system in order to improve the tracks reconstruction of the common single-sided strip detectors. Nevertheless, in its current conception, this implementation appears as a suitable technology for highly ionizing particles as it is the case of neutron monitors based on conversion layers or other nuclear imaging technologies, ranging from Compton cameras to heavy-ion detection.

Finally, chapter 4 relates the new design, fabrication and first characterization of double columns stripixel detectors. The stripixel concept was proposed by Z.Li from the Brookhaven National Laboratory in 2004, when he firstly presented a novel 2D position sensitive silicon detector based on the planar pixel technology and the integration of two metal layers on the detector surface to achieve a projective X-U readout typical of

double-sided strip detectors. After an attempt of placing both the n^+ and p^+ planar electrodes in the same side of the sensor, failed due to the impossibility of depleting the area beneath the electrodes, 3D detector technology has been considered as a promising technology for stripixel detectors, upgrading the device to a radiation hard detector. The new device proposed in this thesis consists of double-column electrodes (both n^+ and p^+) arranged in a diamond configuration on one side of the n-type silicon bulk and connected by two sets of perpendicular strips, organized in two separated metal layers, that allow a X-Y projective readout of the sensor. The final design has been achieved after a computer simulation study of the internal electric field distribution as a function of the bulk and electrodes doping type, carried out with Sentaurus TCAD. A multiple trap distribution model has been used to simulate the defects caused by the saw cut at the edges of the device. The fabrication run dedicated to the prototypes of these detectors has been the most complicated ever carried out in the clean room facilities of the IMB-CNM in Barcelona for what concern radiation detectors processing. The main challenges have been: performing two consecutive column etching processes on the same surface of the wafer and using dual-metal technology over such a complicated structure. Despite of some difficulties during the processing flow, some detectors could be characterized at the end of their fabrication. Electrical characterization allowed to study the leakage current and the depletion voltage of the detectors. Transient Current Technique measurements were used to test the low electric field areas inside the detector bulk and the readout capability from both type of columns. Finally, the same laser set-up used to characterized the new detectors with resistive electrodes has been used to test the 2D position sensitivity of this detector too. This work represents the first fabrication experience and characterization of 3D stripixel detectors. The main results obtained can be summarized as follow:

- A novel 2D position sensitive 3D detector, based on a real single-sided process, has been developed with the use of double-column and dual-metal technologies. The detector is characterized by low depletion voltage (<4V) even if low electric field areas always can be observed in the bottom of the bulk, expecially beneath the n-type columns. The last few microns of the bulk never deplete.

- 2D position sensitivity has been demonstrated reconstructing a laser beam position within a pixel ($80\times80\ \mu m^2$) defined by two consecutive p^+-type strips

crossing two consecutive n^+-type strips, with a spatial resolution of 23 μm, due to the low charge sharing between neighbouring strips.

3D detectors are promising devices for application in the innermost layers of tracking systems and in the pixel vertex detectors at the future colliders facilities, due to their higher radiation hardness compared to planar detectors. Actually, both CMS and ATLAS are investigating the possibility of replacing the current vertex detectors with 3D pixel detectors. Although, short strip detectors have been proposed for the innermost layers of the tracking systems.

Conceptually, 3D stripixel detector can be an alternative for those layers where high radiation hardness is required, but channel occupancy does not put too strong constraints on the electrode design: for instance, the external layers of vertex detectors or the innermost layer of the tracking systems. In practice, apart of the difficulties and costs required by their fabrication process, introducing a proper arrangement of the electrodes and/or stereo-angle between p^+-type and n^+-type strips is mandatory to achieve good performance of the device.

Bibliography

[1] F. Gianotti, M. L. Mangano, T. Virdee, S. Abdullin, G. Azuelos, A. Ball, et al. *Physics potential and experimental challenges of the LHC luminosity upgrade* European Physical Journal C, 39(3), 293 333, 2005.

[2] The web page of ILC is: http://www.linearcollider.org/.

[3] L. Evans and B. Philip, *LHC machine* , Journal of Instrumentation, 3(08),S08001, 2008.

[4] B.Wittmer et al., *The Laser Alignment System for the CMS Silicon Microstrip Tracker* , Nucl. Instr. and Meth. A581 (2007)

[5] The ATLAS collaboration. The ATLAS experiment at the CERN Large Hadron Collider. Journal of Instrumentation, 3(08), S08003, 2008.

[6] M. Moll., *Development of radiation hard sensors for very high luminosity colliders - CERN-RD50 project* Nucl. Instr. and Meth. A 511(1-2), 97-105, 2003.

[7] T. Blass et al., The SiLC Collaboration, *SiLC: Silicon Tracking for the Linear Collider* , PRC R&D 03/02 proposal submitted to the PRC-DESY, April 10 2003, and addendum: PRC R&D 03/02 update 01 (03), and references therein. See also: http://www.desy.de/f/prc/html/documentation.htm

[8] Centro Nacional de Microelectrónica, Campus Universidad Autónoma de Barcelona. 08193 Bellaterra (Barcelona), Spain (http://www.imb-cnm.csic.es/).

[9] Instituto de Física de Cantabria Edificio Juan Jordá, Avenida de los Castros, s/n E-39005 Santander, Cantabria, Spain (http://www.ifca.unican.es/).

[10] G.Lutz *Semiconductor Radiation Detectors: Device Physics* , Springer, 1999.

[11] S.M.Sze *Semiconductor devices* , Ed. Wiley Interscience, 1985.

[12] H.Spieler *Semiconductor detector system* , Oxford Science Pubblications, 2005.

[13] S. Ramo, *Currents induced by electron motion* , Proc. IRE 27, 584585, 1939.

[14] W.R. Leo, *Techniques for nuclear and particles physics experiments* , Springer Verlag, 1994.

[15] R. Turchetta, *Spatial resolution of silicon microstrip detectors* , Nucl. Instr. and Meth. A 335 (1993) 44-58.

[16] S.I. Parker et al., *3D - A proposed new architecture for solid-state radiation detectors* , Nucl. Instr. and Meth. A 395 (1997) 328-343.

[17] G. Pellegrini, M.Lozano, M. Ullan, R. Bates, C. Fleta and D. Pennicard. *First double-sided 3D detectors fabricated at CNM-IMB.* , Nucl. Instr. and Meth. A 592(1-2), 38-43, 2008.

[18] V. A.Wright et al., *Three-dimensional Medipix - a new generation of X-ray detectors* , IEEE Trans. Nucl. Sci., 52(5), 1873-1876, 2005.

[19] J. Morse, C. J. Kenney, E. M. Westbrook, I. Naday, and S. I. Parker. *The spatial and energy response of a 3D architecture silicon detector measured with a synchrotron X-ray microbeam* , Nucl. Instr. and Meth. A, 524(1-3), 236-244, 2004.

[20] C. Piemonte. *Device simulations of isolation techniques for silicon microstrip detectors made on p-type substrates* IEEE Trans. Nucl. Sci., 53(3), 1694-1705, 2006.

[21] C.Fleta, *Tecnologa de detectores de partculas de silicio resistentes a la radiacin* , PhD Thesis, Barcelona 2006.

[22] L. Evensen, A. Hanneborg, B. S. Avset, and M. Nese, *Guard ring design for high-voltage operation of silicon detectors* , Nucl. Instr. and Meth. A 337(1) 4452, 1993.

[23] C.J. Kenney et al., *Active-edge planar radiation sensors* , Nucl. Instr. and Meth. A 565(1) (2006) 272-277.

[24] J. Kemmer, *Fabrication of low Noise Silicon Radiation Detectors by the Planar Process* , Nucl. Instr. and Meth. A 169 (1980) 499-502.

[25] C. Adolphsen et al., *The Mark II silicon strip vertex detector* , Nucl. Instr. and Meth. Phys. Res. A 313 (1992) 63-102.

[26] The web page of LEP is: http://public.web.cern.ch/public/en/research/lep-en.html;

[27] G. Batignani et al. *The ALEPH silicon vertex detector* , Nucl. Phys. B, Proc. Suppl. 23 (1991) 291-296.

[28] N. Bingefors et al., *The DELPHI microvertex detector* , Nucl. Instr. and Meth. A 328 (1993) 447

[29] P.P. Allport et al., *The OPAL silicon strip microvertex detector with two coordinate readout* Nucl . Instr. and Meth . A 324 (1993) 34.

[30] M. Acciarri et al., *The L3 silicon microvertex detector* , Nucl . Instr. and Meth. A 351 (1994) 300-312.

[31] A. Sill for the CDF collaboration, *CDF Run II Silicon Tracking Projects* , Nucl . Instr. and Meth. A447 20001.

[32] The web page of KEK is: http://legacy.kek.jp/intra-e/.

[33] Stanford Linear Accelerator Center, http://www.slac.stanford.edu/.

[34] Inner Tracker Technical Design Report. CERN/LHCC 2002-029 LHCb TDR 008 November 8, 2002, available at: http://lhcb.web.cern.ch/lhcb/TDR/front%20cover/LHCb-IT-TDR.pdf.

[35] The web site of the TOTEM collaboration is: http://totem.web.cern.ch/Totem/.

[36] *Alice Technical Design Report of the Inner Tracking System (ITS)* , CERN /LHCC 9912 ALICE TDR 4, 18 June 1999 available at: http://aliceinfo.cern.ch/ITS/sites/aliceinfo.cern.ch.ITS/files/documents/ITS-TDR.pdf.

[37] W. Wallraff, *TAS status* , AMS Tracker Meeting, CERN, February 9th 2005.

[38] F. Taccetti et al., *Pamela tracking system: status report* , Nucl. Instr. and Meth. A 485 (2002) 7883.

[39] The web page of GLAST is: http://www-glast.slac.stanford.edu/tracker-hardware/publications/c5-paper.pdf.

[40] The web page of CERN is: www.cern.ch.

[41] The RD50 Collaboration, RD50 Status Report 2008, CERN-LHCC-2010-012 and LHCC-SR-003.

[42] The RD50 Collaboration web page is: /http://rd50.web.cern.ch/rd50S.

[43] M. Fernández et al., *R&D on Microstrip IR Transparent Silicon Sensors* Eudet Memo 2007-32 available at: http://www.eudet.org/e26/e28/e182/e428/eudet-memo-2007-32.pdf.

[44] B. Dhoedt, D. Delbeke, *RODIS: Rigorous Optical Diffraction Software* , http://www.photonics.intec.ugent.be/research/facilities/design/rodis/.

[45] P. Bienstmann, L. Vanholme, *CAMFR: Cavity Modelling Framework* , http://camfr.sourceforge.net/.

[46] E.D. Palik, *Handbook of Optical Constants of Solids* , Academic Press. 1st edition (January 15, 1997).

[47] M.J. Keevers, M.A. Green, *Absorption edge of silicon from solar cell spectral response measurements* , Appl.Phys.Lett. 66 (2), 174-176, 9 January 1995

[48] S. E. Aw, H. S. Tan and C. K. Ong, *Optical absorption measurements of band-gap shrinkage in moderately and heavily doped silicon* J. Phys. Condens Matter 3 (1991) 8213-8223.

[49] M. Fernández et al., *Experimental validation of optical simulations for microstrip detectors* Eudet Memo 2008-37 available at: http://www.eudet.org/e26/e28/e615/e838/eudet-memo-2008-37.pdf

[50] M. Fernández et al., *New silicon microstrip detectors optimized for tracker alignment* Nucl. Instr. and Meth. A A624(2010)340343.

[51] T. Bergauer et al., *Results from a first production of enhanced silicon sensor Test Structures produced by ITE Warsaw* , Nucl . Instr. and Meth A 598 (2009) 86-88.

[52] The TOPSIL web page is: http://www.topsil.com/1.

[53] Carlos Martinez *Desarrollo de una tecnologa de detectores de radiacin de silicio de micropistas para aplicaciones de fsica de altas energas* , PhD Thesis, Barcelona 2003.

[54] H.Xiao *Introduction to Semiconductor Manifacturing Technology* , Prentise Hall (2001).

[55] D.Bassignana et al. *Silicon microstrip detectors for future tracker alignment systems* , Nucl. Instr. and Meth. A 628, 276-281.

[56] A. Chilingarov, *Recommendations towards a standardisation of the macroscopic parameter measurements* , Technical note 2003/03, RD50 (2003), available at: http://rd50.web.cern.ch/rd50/.

[57] Near Infrared Spectrometer, NIR 512L-1.7T1 USB, 523 element InGaAs, single stage TE cooled, Control Development, http://www.controldevelopment.com

[58] J. Stefan Institute, Jamova cesta 39, 1000 Ljubljana, Slovenia, http://www.ijs.si/.

[59] D.Bassignana et al., *First investigation of a novel 2D position-sensitive semiconductor detector concept* 2012 JINST 7 P02005.

[60] H. Foeth, R. Hammarstrom, C. Rubbia, *On the localization of the position of the particle along the wire of a multiwire proportional chamber* , Nucl. Instr. and Meth. 109 (1973) 521.

[61] P. Schubelin, et al., *Low mass cylindrical multiwire proportional chamber with unambiguous dual coordinate readout* , Nucl. Instr. and Meth. 131 (1975) 39.

[62] A. Feinberg, N. Horwitz, I. Linscott, G. Moneti, *A Frameless, Cylindrically Shaped, Multiwire Proportional Chamber Using Charge Division Readout* , Nucl. Instr. and Meth. A 141 (1977) 277.

[63] V. Radeka, P. Rehak, *Charge Dividing Mechanism on Resistive Electrode in Position-Sensitive Detectors* , IEEE Transactions on Nuclear Science NS-26 (1979) 225.

[64] R.B. Owen, M.L. Awcock, *One and Two Dimensional Position Sensing Semiconductor Detectors* , IEEE Transactions on Nuclear Science NS-15 (1958) 290.

[65] V. Radeka, *Signal, Noise and Resolution in Position-Sensitive Detectors*, IEEE Transactions on Nuclear Science NS-21 (1974) 51.

[66] J. K. Carman, et al., *Longitudinal resistive charge division in multi-channel silicon strip sensors* , Nucl. Instr. and Meth. A 646 (2011) 118.

[67] R.Marco-Hernandez and ALIBAVA collaboration, *A Portable Readout System for Microstrip Silicon Sensors (ALIBAVA)* , IEEE Transactions on Nuclear Science NS-56 (2009) 1642.

[68] Beetle - a readout chip for LHCb http://www.kip.uni-heidelberg.de/lhcb/.

[69] N. Bacchetta et al. , *SPICE analysis of signal propagation in Si microstrip detectors* , IEEE Transactions on Nuclear Science NS-42 (1995) 459.

[70] Virtuoso Spectre data sheet, Cadence. Available at http://www.cadence.com/products/custom ic/index.aspx.

[71] R. Brun et al., *ROOT An Object-Oriented Data Analisis Framework* . Available at http://root.cern.ch/drupal/.

[72] Alibava-gui documentation. Available at http://twiki.ific.uv.es/twiki/pub/Atlas/ALiBaVa/.

[73] J.C.Vermeulen *Noise in resistive charge-division position-sensing methods* . Nuclear Instruments and Methods in physics Research A 185 (1981) 591-593.

[74] http://www.bnl.gov/world/.

[75] Z.Li, *Novel silicon stripixel detector: concept, simulation, design, and fabriction* , Nuclear Instruments and Methods in Physics Research A 518 (2004) 738-753.

[76] Z.Li, *New 3d Si Detectors at BNL and CNM* , 2006 IEEE Nuclear Science Symposium Conference Record N34-5.

[77] Z.Li, *Development, simulation and processing of new 3D detectors* , Nuclear Instruments and Methods in Physics Research A 583 (2007) 139-148.

[78] R. Nouicer et al. *PHENIX Upgrade: Novel Stripixel Detector for Heavy Quark Detection and Proton Spin Structure Measurements at RHIC Energies* , Nuclear Instruments and Methods in physics Research B 261 (2007) 1067-1071.

[79] R. Nouicer at al. *Status and Performance of New Silicon Stripixel Detector for the PHENIX Experiment at RHIC: Beta Source, Cosmic-rays and Proton Beam at 120 GeV* , 2009 JINST 4 P04011.

[80] Synopsys TCAD Sentaurus, http://www.synopsys.com/tools/tcad/Pages/default.aspx.

[81] W. Fichtner, D. J. Rose, and R. E. Bank. *Semiconductor device simulation* , IEEE Trans. Electron Dev., 30(9), 1018-1030, 1983.

[82] *Sentaurus Device* Version X-2005.10, October 2005 or *Sentaurus Device User s Guide* Version E-2010.12, December 2010.

[83] M. N. O. Sadiku. *A simple introduction to finite-element analysis of electromagnetic problems* , IEEE Transactions on Education, 32(2), 85 93, 1989.

[84] E.P. Nochis et al., *Simulation of planaredgeless silicon detectors with a current terminating structure* , Nucl. Instrum. and Meth. A 583(1) (2007) 77-86.

[85] V. Eremin and Z. Li. *Determination of the Fermi Level Position for Neutron Irradiated High Resistivity Silicon Detectors and Materials Using the Transient Charge Technique (TChT)* , BNL 60072. pres. IEEE Nuclear and Space Radiation Effects Conf., Tucson, AZ. IEEE Trans. Nucl. Sci. NS-41, No. 6, p. 1907 (1994).

[86] V. Eremin, Z. Li, and Ijashenko. *Trapping Induced N_{eff} and Electrical Field Transformation at Different Temperatures in Neutron Irradiated High Resistivity*

Detectors , BNL 60154. pres. at Frontier Detectors for Frontier Physics, 6th Pisa Mtg. on Advanced Detectors, Elba, Italy, 22-28 May (1994). Nucl. Instrum. and Meth. A360 458 (1995).

[87] V. Eremin, N. Strokan, E. Verbitskaya, and Z. Li. *Development of Transient Current and Charge Techniques for the Measurement of Effective Impurity Concentration in the Space Charge Region of p-n Junction Detectors* , BNL 60156. Nucl. Instrum. and Meth. A372 (1996) 388-398.

[88] A. H. Johnston. *Charge Generation and Collection in p-n Junctions Excited with Pulsed Infrared Lasers* , IEEE Transactions on Nuclear Science, vol. 40, NO. 6, december 1993.

[89] Sproul AB, Green MA. *Improved value for the silicon intrinsic carrier concentration from 275 to 375 K* , Journal of Applied Physics [Internet]. 1991 70:846-854. Available from: http://link.aip.org/link/?JAP/70/846/1